이학박사 학위 논문

Long-term Variations of Physical Properties of Seawater in the East Sea (Japan Sea) Revealed by Heat Content and Water Mass Analysis

열용량과 수괴 분석을 통해 고찰한 동해 해수의 물리적 특성 장기 변동

2017 년 8 월

서울대학교 대학원

지구환경과학부

윤 승 태

Abstract

Long-term Variations of Physical Properties of Seawater in the East Sea (Japan Sea) Revealed by Heat Content and Water Mass Analysis

Seung-Tae Yoon
School of Earth and Environment Sciences
The Graduate School
Seoul National University

The global ocean has undergone dramatic warming since the 1950s. As a consequence, the ocean heat content which plays a major role in the variability of Earth's heat balance significantly increases most parts of the global ocean. Moreover, it has been reported that the global meridional overturning circulation (MOC), whose stability and sensitivity to the hydrological cycle and atmospheric forcing are keys to solving uncertainties regarding future ocean changes, would be continuously weakened associated with the global warming.

Although the East Sea (ES) is a small marginal sea in the northwestern Pacific, it is often called as "a miniature ocean" because of a remarkable dynamic similarity with the global ocean. Addressing the response of this marginal sea to the global climate change would be helpful for better understanding present and future environmental changes in the global ocean. In this study, therefore, how the upper ocean heat content (OHC) and ES ventilation system

changed under the continued global warming is investigated.

Long-term variability of non-seasonal OHC in the upper 500 m in the ES exhibits a distinct east-west contrast during the recent 30 years. The contrasting OHC variations are revisited and investigated more in detail by analyzing two observational datasets, the gridded data from 1976 to 2007 and in situ data from 1976 to 2011 in the southwestern ES that covers the zone of western boundary current. The OHC variability shows in-phase and predominant decadal variation in both east and west regions before 1995, but uncorrelated and predominant interannual variations after 1995. Heaving effects due to major branches of warm currents in the ES, the East Korea Warm Current (EKWC) in the western part and other two branches in the eastern part, mainly contribute to the OHC variations. The heaving effect in the southwestern ES is shown to be associated with changes in winter wind stress curl field in the northern ES. Weakening of the subpolar gyre due to weakening of positive wind stress curl in the Japan Basin related with wintertime Western Pacific teleconnection pattern and Siberian High appears to enhance the northward penetration of the EKWC resulting in an increase of OHC in the southwestern ES. The heaving effect in the southeastern ES is significantly correlated with the Siberian High, but the causative mechanism is inconclusive. This study also demonstrates the importance of using highly-resolved datasets for areas affected by strong and narrow boundary currents in computing and understanding the OHC variability.

Also presented in this study are evidences suggesting vigorous changes in the ventilation system of the ES during the latest decade from structure and volume of deep (> 500 m) water masses — Central Water (CW), Deep Water (DW), and Bottom Water (BW). A

shift in the sea' s ventilation system from BW to CW under a warming climate was previously suggested from the deepening of CW-DW and DW-BW boundaries, providing a clue to future changes in global MOC. Here, a slowdown of the deepening since 2000s is newly found associated with re-initiation of the BW formation. A simple one-dimensional (1-D) advection-diffusion model supports a halt of CW formation and continual oxygen supply to DW since 2000s with more chances of the BW formation. A new projection, associated with open-ocean and slope convections in the northern ES, is also provided here allowing the three-layered deep-water structure without loss of BW, at least by 2040.

As a conclusion, the OHC variations and the ventilation system in the ES show significant change in the recent decade and it is suggested that the recent changes of physical properties of seawater in the ES are primarily affected by the atmospheric and oceanic advective or convective processes occurring within and outside the ES rather than an increase of the water temperature due to the global warming. In short, the OHC variations and deep ventilation system in the ES support a previous assertion on the 'East Sea as a miniature ocean'.

Keyword : Global Warming, Ocean Heat Content, Deep Water Mass, East Sea (Japan Sea), Upper Ocean Circulation, Deep Ventilation System

Student Number : 2011-20374

Table of Contents

Abstract ····· i
Table of Contents ····· iv
List of Tables ····· vii
List of Figures ····· ix

1. Introduction ····· 1

1.1. Global warming ····· 1
1.2. East Sea (Japan Sea) ····· 3
1.3. Previous works ····· 10
1.3.1. Ocean heat content change ····· 10
1.3.2. Deep ventilation change ····· 12
1.4. Main purposes ····· 14

2. Data and Methods ····· 16

2.1. Data ····· 16
2.2. Methods ····· 23
2.2.1. Heat content calculation and decomposition ····· 23
2.2.2. CTD data processing ····· 25
2.2.3. Finding deep structures ····· 34
2.2.4. 1-D advection-diffusion model ····· 34
2.2.5. Significant level of trend and correlation ····· 38

3. Results ····· 39

3.1. An east-west contrast of upper ocean heat content variation south of the subpolar front in the ES ····· 39
3.1.1. Characteristics of OHC variations in the ES ····· 39
3.1.1.1. Linear trend of HCA ····· 39
3.1.1.2. Interannual and decadal heat content variability ··· 47
3.1.2. Decomposition of HCA ····· 53
3.1.3. HCA and depth variation of 10 ℃ isotherm ····· 60
3.1.4. HCA and upper circulation ····· 64
3.1.5. Causative mechanisms for HCA variation ····· 73
3.1.5.1. Relationship between HCA and volume transport through the Korea Strait ·····73
3.1.5.2. Relationship between HCA and winter wind stress curl ····· 81
3.1.5.3. Influence of the Siberian High and Western Pacific teleconnection pattern ····· 86

3.2. Re-initiation of bottom water formation in the ES: Another clue to future changes in global ocean ····· 91
3.2.1. Observations on deep structural changes ····· 91
3.2.2. 1-D advection-diffusion model ····· 97
3.2.3. Significant role of convective DO supply for changing deep-water structures ····· 102
3.2.4. Winter surface atmospheric and oceanic conditions associated with ES ventilation system change ····· 105

4. Discussion ····· 114

4.1. Comparison between variations in the recent decade and those in the past ····· 114

4.2. Warming effect on physical properties of seawater changes in the ES ····· 115
4.3. Non-warming effect on physical properties of seawater changes in the ES ····· 116
4.4. Implications for the global ocean ····· 117
4.4.1. Importance of the heaving effect on ocean heat content variations ····· 117
4.4.2. A possibility on global MOC re-strengthening ····· 118

5. Conclusions and suggestions for the future study ····· 122

Bibliography ····· 128
Abstract (in Korean) ····· 142
Appendix ····· 145
Publications and Presentations ····· 154

List of Tables

Table 2.1. Information on CREAMS or EAST-I cruises between 1993 and 2016. *T, S*, and DO denote water temperature, salinity, and dissolved oxygen, respectively. 2 1

Table 2.2. SBE Data Processing sequences referred to Sea Bird-Electronics [2014] 2 8

Table 2.3. Equations for calibrated DO profiles estimated with Winkler bottle samples and full-depth DO profiles at four cruises together with number of the bottle samples and RMS difference between the bottle data and CTD DO profiles..... 3 2

Table 3.1. Linear trends of non-seasonal heat content variation in the upper 500 m in the global ocean and Pacific Ocean during 1955–2010 [from Figure 2 in Levitus et al., 2012], and those in the whole area of NA12 data (EJS), southeastern ES (EAST), southwestern ES (WEST), and the region covered by the KODC data (UB) during 1976–2007 together with the 90% confidence level of the trend. 4 6

Table 3.2. Percent variance of each decomposed part of total eight components of HCA to HCA, cross correlation coefficients between each decomposed part and HCA, and the linear trend of each decomposed part (Trend) in the four regions defined in the text with 90% confidence level of the trend. $\overline{T}H'_i$ denotes the i-th heaving component and $\overline{T}H'_i$ the i-th warming component. 5 7

Table 3.3. The largest correlation coefficients at zero lag (upper part) and lagged correlation coefficients (lower part) between de-trended $\overline{T}H'_1$ in the EAST or in the UB and de-trended climate indices and volume transport components through the Korea Strait. The cross correlation coefficients are calculated with lags up to 2 years with those significant at the 95% confidence level highlighted in bold. Other listed cross correlation coefficients are significant at 90% confidence level.

Left (right) number in parentheses denotes lags in months (degrees of freedom). DJF WP, DJF SH, VT, WVT, and EVT denote the winter (December–February) Western Pacific teleconnection pattern, winter Siberian High, total volume transport through the Korea Strait, and volume transports through the western channel and though the eastern channel, respectively. 7 7

Table 3.4. Cross correlation coefficients between winter SH and WP, between VT and WVT or EVT, and between WVT and EVT. Cross correlation coefficients significant at the 95% confidence level are highlighted in bold. Left (right) number in parentheses denotes lags (degrees of freedom). Parameters on the left column lead those on the right and vice versa. 7 8

Table 3.5. Compare the boundary values and fitting coefficients (*Z**, *J/w*) between 1996 and 2015 applied in the 1-D advection-diffusion model. 1 0 0

Table A1. Abbreviations used in the dissertation..... 1 4 5

Table A2. Percent variance of each decomposed part of total eight components of HCA to HCA, cross correlation coefficients between each decomposed part and HCA, and the linear trend of each decomposed part (Trend) in the EJS defined in the text with 90% confidence level of the trend. $\overline{TH}'_{i-}$ denotes the i-th heaving component and $\overline{TH}'_{i-}$ the i-th warming component. 1 4 8

Table A3. The long-term trends of deep structures reported in Kang et al. [2003b] and calculated in this study. The position of station C, W, and E is 41.3°N, 134°E, 41°N, 132.3°E, and 42°N, 136°E, respectively. The JB denotes trends of the averaged deep structures in the JB (north of 39°N, 131–139°E). A positive value means a deepening tendency of depth. The significant trend at 95% confidence level is highlighted in bold. Other listed trends are significant at 90% confidence level. 1 4 9

Table A4. Upper and Lower limit of CW and DW for applying the 1-D advection-diffusion model at each cruise' s Station C. 1 5 0

List of Figures

Figure 1.1. A cover page of synthesis report of the IPCC (Intergovernmental Panel on Climate Change) fifth assessment report [IPCC, 2014] 2

Figure 1.2. Reproduce the Figure 1 in Levitus et al. [2012]. A red (black) line indicates five-year running mean time series for the world ocean of heat content (10^{22} J) for the 0–2,000 m (700–2,000 m) layers. The vertical bar and grey-shaded area represent +/− two standard error about each time series..... 2

Figure 1.3. (a) Global sea surface temperature (SST) difference map between the 2000s and the 1980s with 0.1 ℃ color interval. A black box indicates the East Sea (Japan Sea). (b) The green diamonds denote stations of KODC (Korea Oceanographic Data Center) data and brown dots indicate stations where the hydrographic data were collected through the CREAMS (Circulation Research of the East Asian Marginal Seas) or EAST (East Asian Seas Time-series)-I cruises. A 500 m (3,000 m) isobaths is represented with grey (black) contours. Also shown are three basins of the East Sea deeper than 2,000 m, the Japan Basin (JB), the Ulleung Basin (UB), and the Yamato Basin (YB). The data collected in the central JB or the Station C (centered around 134°E, 41.3°N, blue squares) are mainly used here. Other stations in the eastern JB are also remarked with blue and green circle, respectively. VL, EKB, SY and TS denote Vladivostok, East Korea Bay, Soya Strait and the Tsugaru Strait..... 7

Figure 1.4. (a) Major surface currents of the East Sea with red denoting warm currents, blue cold currents, and grey subpolar gyre [Park et al., 2013]: East Korea Warm Current (EKWC), Offshore Branch (OB) and Nearshore Branch (NB) of the Tsushima Warm Current (TWC), North Korea Cold Current (NKCC), and the Liman Cold Current (LCC). A 2,000 m isobaths is denoted by grey contours. (b) Vertical profiles of

potential temperature (red), salinity (blue), and dissolved oxygen (green) observed at Station C in October, 2005. The pressure range is from 200 to 3,600 dbar. A blue (magenta) arrow indicates a deep salinity (dissolved oxygen) minimum depth. An upper limit of benthic homogeneous layer detected in potential temperature (dissolved oxygen) profile is denoted by a red (orange) arrow. The layer between 0.6 ℃ isotherm and a deep salinity minimum depth is defined as Central Water (CW). Bottom Water (BW) is located within a benthic homogeneous layer and Deep Water (DW) is existed between CW and BW. 9

Figure 2.1. (a) Potential temperature (θ) – salinity (S) diagram at Station C with potential density contours observed in April, 2014. Pre (Post) - cruise calibrated sensor' s data are represented by a blue (red) line. The data applied a pre- and post-cruise calibration is indicated by a black line. (b) RMS (Root Mean Square) difference among salinity (red dots) and temperature (blue squares) processed by four CellTM processes: Morison et al. [1994], Kim et al. [2000], Mensah et al. [2009], and Sea-Bird Electronics [2014]. Black solid line denotes an accuracy of temperature (T) and salinity (S). The x-axis for RMS difference is represented by a log-scale. Data of six cruises are used in this test: Oct., 2005; May, 2007; Jul., 2009; Oct., 2012; Apr., 2014; Apr., 2015. ..... 2 9

Figure 2.2. (a) Relation between CTD dissolved oxygen (DO) sensor data ($DO_{obs.}$) and Winker bottle samples (DO_{bottle}) observed at June, 1999 (red dots). A blue line indicates a linear regression line obtained by using two variables (predictor = $DO_{obs.}$, dependent variable = DO_{bottle}) (b) The same as Figure 2.2a, but for October, 2012. (c) The same as Figure 2.2a, but for April, 2014. (d) The same as Figure 2.2a, but for April, 2015 ..... 3 1

Figure 2.3. Final-calibrated DO profiles at Station C from 1996 to 2015..... ..... 3 3

Figure 2.4. (a) Potential temperature (θ) – salinity (S) diagram at Station C

with potential density contours observed in June, 1999. Solid dashed line marked between CW (DW) and DW (BW) indicates deep salinity minimum (upper limit of benthic homogeneous layer). Red dots in the CW (DW) represent the range of linearity in $\theta - S$ diagram. 1-D advection-diffusion model is applied in these ranges. (b) Results of potential temperature profiles by the 1-D advection-diffusion model. Potential temperature profile in each layer is denoted by a blue solid line and potential temperature profile fitted to Z^* (K/w) is represented by a red solid line. Range of Z^* is from 0.2 to 2.0 km. (c) The same as Figure 2.4b, but for DO profiles. DO profile in each layer is denoted by a blue solid line and DO profile fitted to J/w is represented by a red solid line. Range of J/w is from −70 to 70 μmol/kg/km. 3 7

Figure 3.1. (a) Spatial pattern of long term (1976–2007) trends of non-seasonal heat content in the upper 500 m based on NA12 data [Na et al., 2012]. The shaded areas have significant trends at the 90% confidence level. The positive (negative) trend is shown by red solid (blue dashed) lines with zero value denoted by a black solid line. The contour interval is 1×10^6 J/m^2/month. The black-box regions EAST, WEST, and EJS correspond to 135–140°E and 36–42°N, 130–133°E and 35–39°N, and 130–140°E and 35–42°N, respectively. KODC stations are also shown by dots. WC (EC) denotes the western (eastern) channel of the Korea Strait. (b) The same as Figure 3.1a, but for the AVHRR sea surface temperature during 1982–2007. The contour interval is 0.02 ℃/year. (c) The same as Figure 3.1a, but for the results in the region UB covered by KODC data. The contour interval is 2×10^6 J/m^2/month, the stations with a significant trend at 90 % confidence level are denoted by shaded squares. HCAs shown in Figure 3.3e are calculated in overlapped areas (black boxes) between the NA12 and KODC data. 4 3

Figure 3.2. (a) Linear trends of non-seasonal heat content during 1976–2007 as a function of depth in the EJS (black diamond) together with those in the global ocean (magenta arrow) and Pacific Ocean

(grey triangle) during 1955–2010 [from Figure 2 in Levitus et al., 2012]. (b) Percent variances accounted for by the linear trends as a function of depth in the EJS together with those for global and Pacific oceans [from Figure S3 in Levitus et al., 2012]. (c) The same as Figure 3.2a, but for the EAST (red), WEST (blue), and UB (green). (d) The same as Figure 3.2b, but for EAST (red), WEST (blue), and UB (green). 45

Figure 3.3. (a) Time series of HCA in the EJS during 1976–2007. The linear trend of HCA in the EJS is shown by a black dashed line. (b) Time series of HCA during 1976–2007 in the EAST (red) and WEST (blue) with their respective linear trends. Vertical green dashed lines indicate years for dividing the time series of HCA in the EAST and WEST into in- and out-phase periods. (c) De-trended time series of HCA in the EJS (dashed line), EAST (red line), and WEST (blue line). For HCA in the EAST, the two-year advanced time series is shown. (d) Time series of HCA in the UB based on KODC data from 1976 to 2011 (purple) with HCA in the WEST based on NA12 data (blue). The linear trend of HCA in the UB is shown by a dashed line. (e) Time series of HCA using original KODC data (grey shade), gridded KODC data (blue line), gridded and smoothed KODC data by the Gaussian filter (red line), and NA12 data in an overlapped area between KODC and NA12 datasets enclosed by black box in Figure 3.1c (black line) 50

Figure 3.4. Lead-lag correlations (a) between HCA in the WEST and EAST during 1976–1994 (WEST leading), (b) HCA in the WEST and EJS (WEST leading), and (c) HCA in the EAST and EJS (EJS leading). All time series are de-trended, and the maximum lead-lag correlations are indicated (star) with corresponding lags. The range of months indicates the same correlation values for those lags when the correlation is rounded off to 2 decimal digits. Red dashed lines represent the 95% confidence level. Degrees of freedoms, hence the 95% confidence levels are different depending on the lag. 52

Figure 3.5. (a) Time series of HCA (shading), $\overline{TH}'_1$ (red), $\overline{TH}'_3$ (blue), and $\sum_{i=2}^{4}\overline{TH}'_i$ (black dashed) in the EAST (b) Time series of HCA (shading), $\overline{TH}'_1$ (red), $\overline{TH}'_2$ (green), and $\sum_{i=2}^{4}\overline{TH}'_i$ (black dashed) in the UB 59

Figure 3.6. (a) Spatial pattern of long-term (1976–2007) averaged 10 ℃ isotherm depth in the EJS. Contour interval is 10 m. Black boxes indicate the WEST and EAST regions. (b)–(c) Horizontal distributions of 10 ℃ isotherm depth anomaly averaged over in-phase periods, 1981–1987 and 1990–1994. (d)–(e) Horizontal distributions of 10 ℃ isotherm depth anomaly averaged over the out-phase periods, 1976–1980 and 1995–2007. Contour interval is 2 m. The positive (negative) values are shown with black solid (blue dashed) lines and the zero value is denoted by red solid lines. 62

Figure 3.7. (a) The same as Figure 3.6a, but in the UB. (b)–(e) The same as Figure 3.6b–e, but in the UB. Contour interval is 5 m. 63

Figure 3.8. (a) Mean depth of the 10 ℃ isotherm during 1976–2007 for stations deeper than 500 m based on NA12 data. Black boxes indicate the WEST and EAST regions. The contour interval of black bold (thin) line is 40 (10) m. (b) The same as Figure 3.8a, but for the mean dynamic height (geopotential height anomaly at surface relative to 500 m divided by the acceleration of gravity in meters). The contour interval of black bold (thin) line is 0.1 (0.2) m. (c) The same as Figure 3.8a, but for the satellite-altimetry derived (AVISO) mean sea surface height (SSH). The contour interval of black bold (thin) line is 0.1 (0.2) m. 69

Figure 3.9. Spatial patterns of mean dynamic height (a, b, c) in the EJS based on NA12 data and (d, e, f) in the UB based on KODC data. (a), (d) in 1977, (b), (e) in 1984, and (c), (f) in 1991. Arrays of squares in (a) and (d) denote two sections where surface geostrophic currents are calculated using sea surface height data shown in Figure 3.10b and 3.10d. 70

Figure 3.10. (a) Relation between section-averaged monthly surface

geostrophic velocity relative to 500 m based on NA12 data and surface geostrophic velocity calculated from monthly mean AVISO SSH data along the section in the EAST shown in Figure 3.9a. Numbers on the bottom right denote correlation coefficients, which are both significant at the 95% confidence level. (b) Time series of $\overline{T}H'_1$ in the EAST (grey bar) and section-averaged northeastward geostrophic velocity (blue line) along the line shown in Figure 3.9a. The correlation coefficient is shown on the bottom right, which is significant at the 95% confidence level. (c) The same as Figure 3.10a, but for the relation between bimonthly surface geostrophic velocity calculated using KODC data and surface geostrophic velocity obtained using bimonthly-averaged SSH field along the section shown in Figure 3.9d. (d) The same as Figure 3.10b, but for the time series of $\overline{T}H'_1$ in the UB (grey bar) and northward geostrophic velocity (blue line) along the line shown in Figure 3.9d. 7 1

Figure 3.11. Spatial correlation map (a) between non-seasonal SST variation and $\overline{T}H'_1$ variation in the WEST (1982–2007), (b) between non-seasonal SST variation and $\overline{T}H'_1$ in the UB (1982–2011), and (c) between non-seasonal SST variation and $\overline{T}H'_1$ in the EAST (1982–2007). The non-seasonal SST is calculated by subtracting the monthly mean climatology. The shaded areas have a significant correlation coefficient at the 90% confidence level. Areas having a significant correlation coefficient at the 95% confidence level is also shown in (c) with yellow green color. 7 2

Figure 3.12. (a) Time series of annual mean volume transports through the Korea Strait (VT, black square), the western channel (WVT, blue circle), and the eastern channel (EVT, pink triangle). The left y-axis is for the VT and the right y-axis is for the WVT and EVT. (b) Time series of annual mean $\overline{T}H'_1$ in the UB (grey bar), in the EAST (red solid line), WVT (blue circle), and EVT (pink triangle). (c) Time series of wintertime Siberian High (SH) index (blue circle), and annual mean $\overline{T}H'_1$ in the UB (grey bar) and in the EAST (red line). The right

y-axis is for the SH index, with reversed values. (d) Time series of wintertime Western Pacific teleconnection pattern (WP) index (blue line), and annual mean $\overline{TH}'_1$ in the UB (grey bar) and in the EAST (red line). All time series in (b)–(d) are de-trended..... 7 9

Figure 3.13. (a) Spatial pattern of winter-mean wind stress curl (WSC) (December–February) during 1979–2011. Black contour line denotes the zero WSC. (b) Spatial correlation map between de-trended annual mean $\overline{TH}'_1$ in the UB and the de-trended winter-mean wind stress curl anomaly (WSCA) during 1979–2011. The WSCA is calculated by subtracting the monthly mean WSC. The shaded areas have a significant correlation coefficient at the 95% confidence level. (c) The same as Figure 3.13b, but for correlation between de-trended annual mean $\overline{TH}'_1$ in the EAST and the de-trended winter-mean WSCA during 1979–2007. (d) The same as Figure 3.13b, but for correlation between de-trended winter-mean WP and WSCA during 1979–2011. (e) The same as Figure 3.13b, but for correlation between de-trended winter-mean SH and WSCA during 1979–2011. ..... 8 4

Figure 3.14. (a) The mean sea surface height [m] during 1993–2011 with a color scale shown in the right. An interval of a black (bold) line is 0.01 m (0.1 m). (b) The same as Figure 3.14a, but for the periods when de-trended $\overline{TH}'_1$ in the UB is over $2 \times 10^8\ J/m^2$ (1998, 2001, 2002, and, 2004) (c) The same as Figure 3.14a, but for the periods when de-trended $\overline{TH}'_1$ in the UB is below $-2 \times 10^8\ J/m^2$ (1993, 1994, 1995, 1996, 1997, 2000, and 2005). 8 5

Figure 3.15. (a) Spatial pattern of mean wind vectors and wind speed (color) during 1979–2011. (b) The same as Figure 3.15a, but for the mean wind in 1986. Annual mean dynamic height relative to 500 m in 1986 is also shown with solid lines. (c) The same as Figure 3.15b, but for the mean wind and dynamic height in 1990. ..... 9 0

Figure 3.16. Time series of the boundaries between Central Water (CW) and Deep Water (DW) defined by 0.13–0.15 ℃ isotherms (open circles [Kang et al., 2003b] and purple triangles) or deep salinity

minimum (DSM, red circles), between DW and Bottom Water (BW) or upper limit of benthic homogeneous layer (UBHL, derived from potential temperature; magenta squares or dissolved oxygen; open squares [Kang et al., 2003b] and brown asterisks), and depth of dissolved oxygen minimum (DOM, grey diamond) for 67 years from 1950 to 2016. Isotherms of 0.6 ℃ used for upper boundary of CW are shown with crosses. Data collected in 1999 (June), 2000, and 2001 using different Conductivity-Temperature-Depth (CTD) instruments are shown with yellow circles and squares. The DSM observed in 2012 is denoted with blue circle. Three black dashed lines denote the upper boundary of the CW fixed at 200 m, and linear fits to the observed CW−DW and DW−BW boundaries (from top to bottom), previously reported using data from 1950 to 1996 [Kang et al., 2003b] (not shaded). Red solid lines are new fits to the up-to-dated boundaries whereas the dashed lines are old fits projected previously. Vertical bars indicate an uncertainty of the boundary depth. 9 4

Figure 3.17. Time series of Bottom Water (BW) dissolved oxygen (DO) observed from 1977 to 2015 in the Station C (blue squares), Station E (blue circles), and eastern JB (green circles) [Gamo, 2014] where are shown in Figure 1.3 as blue square, blue circle, and green circle, respectively. A green dashed line indicates a linear trend of declining BW DO in the eastern JB between 1970 and 2020, derived using data collected from 1977 to 1999. The blue dashed (solid) line shows for the same linear trend between 1996 and 2020 but with data collected at Station E (Station C) from 1996 to 2015. ..... 9 6

Figure 3.18. (a) Time series of Z^* at station C. Z^* values for the CW and DW are shown with magenta triangles and black circles, respectively. (b) Vertical profiles of potential temperature for four periods (1979, 1996, 2005, and 2015) marked with vertical dashed lines in Figure 3.18a and 3.18c. (c) Time series of J/w at station C. J/w values for CW and DW are shown with the magenta triangles and black circles, respectively, filled with red (positive) and blue (negative) colors. J/w

for CW and DW, independently estimated from the water boundary fits shown in Figure 3.19b (J/w_{MOD}), is shown with red and green vertical bars, respectively. (d) The same as Figure 3.18b, but for dissolved oxygen..... 101

Figure 3.19. (a) Relationship between East Sea area and corresponding depth digitized from Kim et al. [2002a]. (b) Time series of the volumes of CW, DW, and BW calculated from the linear relationship of Figure 3.19a. Markers are the same as Figure 3.16. 104

Figure 3.20. (a) The winter (DJF) mean net heat flux (NHF) during 1980–2016. The northwestern East Sea where the surface fluxes are averaged (see texts for details) is remarked with a black box. The NHF is positive when ocean loses heat. (b) The same as Figure 3.20a, but for the fresh water flux (FWF). The FWF is positive when evaporation is larger than precipitation. 110

Figure 3.21. Winter (DJF) fresh water flux anomaly (evaporation minus precipitation; positive when ocean loses freshwater) vs. net heat flux anomaly (positive when ocean loses heat) averaged in a black box region in Figure 3.20 during 1980–2016. The integrated anomalies of fresh water and heat fluxes for 10-year-segments starting from 1980 are shown with colored squares (1980s, 1990s, and after 2000s are marked with grey, blue, red, and orange colors). The red star denotes the case of 2000–2001 winter when the slope convection was observed with sufficiently high sea surface density (SSD)..... 111

Figure 3.22. Changes in sea surface salinity (SSS, blue circle) and sea surface temperature (SST, red triangle), both averaged over the area marked with the black box in Figure 3.20, regressed from the flux anomalies. The surface buoyancy flux anomaly out of (into) the area is represented by vertical orange (sky blue) bars with 5-year running mean (thick black line). The y-axes are for the changes of SSS (blue), SST (upside down, red), and surface buoyancy flux (black). And a black dashed line indicates values in winter, 2001..... 112

Figure 3.23. (a) Locations where the winter mixed layer depth deeper than

500 m was observed for the period 1995–2000 with a color scale shown in the right. (b) Time series sea ice concentration [%] (cases exceeding 15% only) averaged over the Tartarsky Strait region (marked with black dots in Figure 3.23a) from November to February between 1979 and 2015 (black line), and its linear trends from 1979 to 1995 (green line) and from 1995 to 2015 (blue line). VL denotes the Vladivostok, Russia. 1 1 3

Figure 3.24. Schematics of changes in the East Sea ventilation since the 1950s. Vertical water boundaries are shown for representing periods; (1950s, 1980s, 1990s, 2000s, and 2010s with significant changes in 1990s and 2000s) following the volumes of deep-water masses (CW; Central Water, DW; Deep Water, and BW; Bottom Water). Convective supplies of water volume (e.g., transport) and DO (e.g., flux) from the surface are marked with thick filled arrows where the formation of CW (DW and BW) via open-ocean convection (slope convection) is highlighted. Significant increasing and decreasing water volumes are shown with vertical arrows. Recent slowdowns of reduction in DW and BW are marked with hyphens in 2000s and 2010s. A thin green arrow denotes “a clue” and thin blue arrow indicates “another clue” 1 2 0

Figure 3.25. The same as Figure 3.18d, but a vertical DO profile in 1954 [Kim et al., 2001] is also represented by violet triangles and line. Plus (Dashed) lines indicate the upper (lower) boundary of CW at 1996 and 2015. Asterisk lines are for the upper boundary of BW at 1996 and 2015. Vertical DO profiles from 1954 to 1979 to 1996 and from 1996 to 2005 to 2015 denote “a clue” (green arrows) and “another clue” (blue arrows) to future changes for global ocean. 1 2 1

Figure A1. (a) Time series of HCA (shading), $\overline{\mathrm{TH}}'_1$ (red), $\overline{\mathrm{TH}}'_3$ (blue), and $\sum_{i=2}^{4}\overline{\mathrm{TH}}'_i$ (black dashed) in the EJS. Vertical green dashed lines indicate years for dividing the time series of HCA in the EAST and WEST into in- and out-phase periods. (b) Time series of HCA (shading), $\overline{\mathrm{TH}}'_1$ (red), $\overline{\mathrm{TH}}'_2$ (green), and $\sum_{i=2}^{4}\overline{\mathrm{TH}}'_i$ (black dashed) in the WEST..... 1 5 1

Figure A2. Spatial correlation map (a) between de-trended non-seasonal SST variation and $\overline{TH}'_1$ variation in the WEST (1982–2007), (b) between de-trended non-seasonal SST variation and $\overline{TH}'_1$ in the UB (1982–2011), and (c) between de-trended non-seasonal SST variation and $\overline{TH}'_1$ in the EAST (1982–2007). The non-seasonal SST is calculated by subtracting the monthly mean climatology. The shaded areas have a significant correlation coefficient at the 90% confidence level. Areas having a significant correlation coefficient at the 95% confidence level is also shown in (c) with yellow green color..... 1 5 2

Figure A3. A blue dot line indicates salinity (S) gradients between DSM and DSM minus 500 m ($|S_{z=DSM} - S_{z=DSM-500}|/500$ $[m^{-1}]$) during 1993–2016. A red dot line shows dissolved oxygen (DO) gradients between DOM and DOM minus 500 m ($|DO_{z=DSM} - DO_{z=DSM-500}|/500$ $[\mu mol/kg/m]$) during 1993–2016. ..... 1 5 3

1. Introduction

1.1. Global warming

According to the synthesis report of the IPCC (Intergovernmental Panel on Climate Change) fifth assessment report [IPCC, 2014] (Figure 1.1), the earth system has been experienced unequivocal warming since the 1950s and this warming is unprecedented over decades to millennia. The globally averaged land and ocean surface temperature are increased about 0.85 ℃ during 1880–2012 and global mean sea level rises about 0.19 m over the period 1901–2010. The global ocean has warmed by about 24×10^{22} J in the upper 2,000 m for the period 1955–2010, which means an increase of seawater temperature by 0.09 ℃ per unit volume [Levitus et al., 2012] (Figure 1.2). Especially, energy increased by ocean warming accounts for more than 90% of the energy accumulated in the climate system during 1971–2010. That is, the affection of the global warming is dominantly shown in the ocean with large heat capacity and mass rather than atmosphere. The main physical driver for the recent climate change is considered as an increase of anthropogenic greenhouse gas emissions since the pre-industrial era.

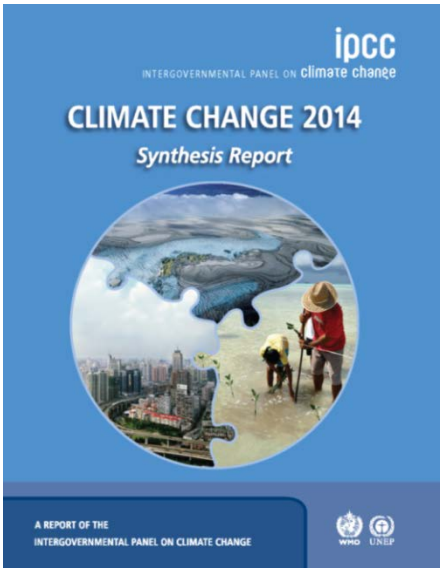

Figure 1.1. A cover page of synthesis report of the IPCC (Intergovernmental Panel on Climate Change) fifth assessment report [IPCC, 2014]

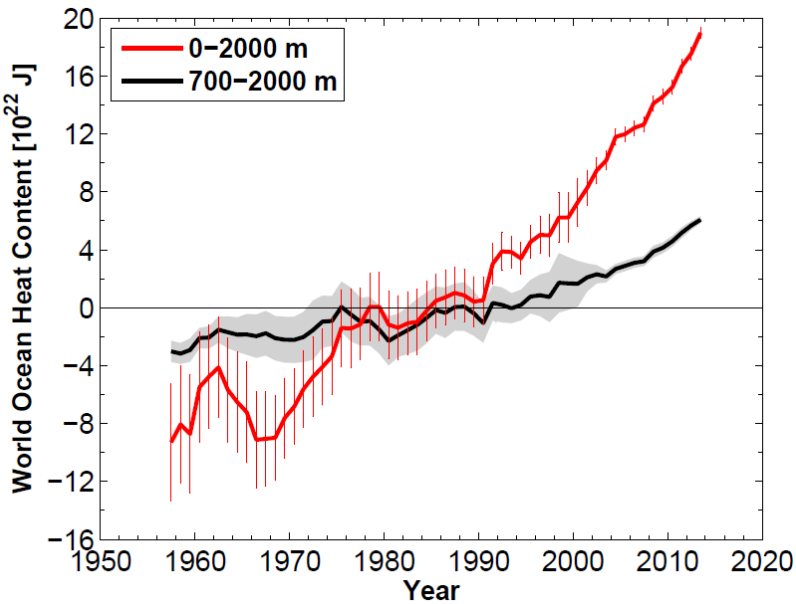

Figure 1.2. Reproduce the Figure 1 in Levitus et al. [2012]. A red (black) line indicates five-year running mean time series for the world ocean of heat content (**10^{22} J**) for the 0–2,000 m (700–2,000 m) layers. The vertical bar and grey-shaded area represent +/− two standard error about each time series.

1.2. East Sea (Japan Sea)

The East Sea (ES)[①] is a semi-enclosed marginal sea located in the northwestern Pacific (Figure 1.3a) with total area and average depth of about 10^6 km^2 and 1,700 m, respectively. The ES is one of the oceans where sea surface temperature (SST) has been warmed in recent decades (Figure 1.3a). It is composed of three basins (i.e., Japan Basin, Ulleung Basin, and Yamato Basin) deeper than 2,000 m and connected with neighboring seas via shallow (< 200 m) straits (Figure 1.3b). The ES is often called a miniature ocean because of its own thermohaline circulation and shallow sill depths.

In the southern part of the ES, the Tsushima Warm Current (TWC) originating from the Kuroshio enters the ES through the western and eastern channels of the Korea Strait with a larger volume transport through the western channel [Fukudome et al., 2010]. The TWC entering the ES through the Korea Strait is the main heat source of the upper ocean in the ES [Han and Kang, 2003], acts to compensate for the net heat loss from the ocean to atmosphere, and thus maintains an equilibrium state [Hirose et al., 1996]. An annual mean heat transport through the Korea Strait is 0.17 PW (1 PW = 10^{15} W), which is about one-tenth of the heat transport by the Kuroshio in the East China Sea [Park et al., 2016].

The TWC approaching the Korea Strait splits into three branches downstream of the Korea Strait (Figure 1.4a). The TWC through the eastern channel feeds the Nearshore Branch (NB) flowing along the west coast of Japan from the eastern channel to the Tsugaru Strait, which follows isobaths shallower than 200 m [Hase et al., 1999; Lee et al., 2016]. The TWC through the western

① All abbreviations used in the dissertation are shown in Table A1.

channel bifurcates into two branches: the Offshore Branch (OB) and the East Korea Warm Current (EKWC). The EKWC flows along the east coast of Korea, separates from the coast at around 38°N, and then meanders eastward [Chang et al., 2004]. Recently, a stable eastward current was found around 39.5°N west of 131°E [Ito et al., 2014], which appears to indicate a dual stable separation latitude of the EKWC. The OB turns to the east south of 36°N and merges with the NB around 132.5°E [Ito et al., 2014; Lee et al., 2016]. Part of the merged OB and NB (ONB) flows north- and northeastward towards the Tsugaru Strait and the ONB also merges with the separated EKWC west of the Tsugaru Strait.

Surface circulation in the subpolar region of the ES consists of basin- and subbasin-scale cyclonic gyres [Isobe and Isoda, 1997; Yoon and Kim, 2009], which is driven by the positive wind stress curl (WSC) in winter [Kim and Yoon, 1996] (Figure 1.4a). As part of this cyclonic gyre, the Liman Cold Current and the North Korea Cold Current (NKCC) flow southwestward along the coast of Russia and North Korea (Figure 1.4a). The NKCC continues to flow southward along the east coast of Korea. After collision with the EKWC, the upper NKCC separates from the coast together with the EKWC and meanders to the east forming the subpolar front of the ES near 40°N. Surface signature of the subpolar front is often captured by high SST gradients except for the summer [Park et al., 2004]. The subsurface water carried southward by the NKCC constitutes the North Korea Cold Water (NKCW, 1 ℃ < temperature < 5 ℃), which is identified below the warm water brought by the EKWC south of the subpolar front [Chang et al., 2002].

Highly variable upper circulation and associated currents on multiple timescales in the southern ES have been documented [Katoh, 1994; Mitchell et al., 2005; Ito et al., 2014], which includes the disappearance of the EKWC intermittently [Hong et al., 1984; Kim and Legeckis, 1986; Mitchell et al., 2005]. The path variability of the warm currents together with the cold current from the north results in the seasonal and interannual variations of upper layer thermal structure and temperature [Cho and Kim, 1996; 2000].

The ES also has deep and intermediate water formations similar with the global ocean [Seung and Yoon, 1995; Kim and Kim, 1996; Minami et al., 1999; Kim et al., 2001; Talley et al., 2003; Kim et al., 2004; Min and Warner, 2005; Postlethwaite et al., 2005]. The ES is well ventilated through processes of subduction, convection, and brine rejection, yielding that deep-water dissolved oxygen (DO) is highest in the Pacific [Kim et al., 2001; Kang et al., 2003a; 2004a; Talley et al., 2003; Postlethwaite et al., 2005; Talley et al., 2006]. Very cold and oxygen-rich deep-water masses in the ES, formerly called Japan Sea Proper Water (JSPW) [Uda, 1934], were subdivided into the Central Water (CW), Deep Water (DW), and Bottom Water (BW) using a highly precise measurements [Kim et al., 1996; Kim et al., 2004; Talley et al., 2006]. In a full-depth salinity profile, the deep salinity minimum (DSM) lies at a depth of around 1,500 m (Figure 1.4b) and defines the lower (upper) boundary of the CW (DW) [Kim et al., 1996; Kim et al., 2004]. With rare salinity measurements of sufficiently high vertical resolution, isotherms of 0.13–0.15 ℃ were previously used to determine the boundary between CW and DW [Kang et al. 2003b]. And Kim et al. [1996] first used the 1 ℃ isotherm as the upper boundary of the CW but the boundary was refined later as the 0.6 ℃ isotherm in

Kim et al. [2004] (Figure 1.4b) with a significant warming of 0.45 ℃ during 1969–2007 [Kim et al., 2001; Kim et al., 2008]. A benthic homogeneous layer (BHL) with a nearly constant potential temperature (θ) or DO characterizes BW [Gamo et al., 1986; Kim et al., 2004] (Figure 1.4b). A DO minimum (DOM) depth is found between DSM and upper boundary of BHL (UBHL), within the DW regime, presumably due to its relatively "old" age (Figure 1.4b). The DOM structure indicates that formations of CW (via open-ocean deep convection) and BW (via brine rejection and slope convection) are more active than that of DW [Kim et al., 2001; Kim and Kim, 1996; Kim et al., 2004; Talley et al., 2006].

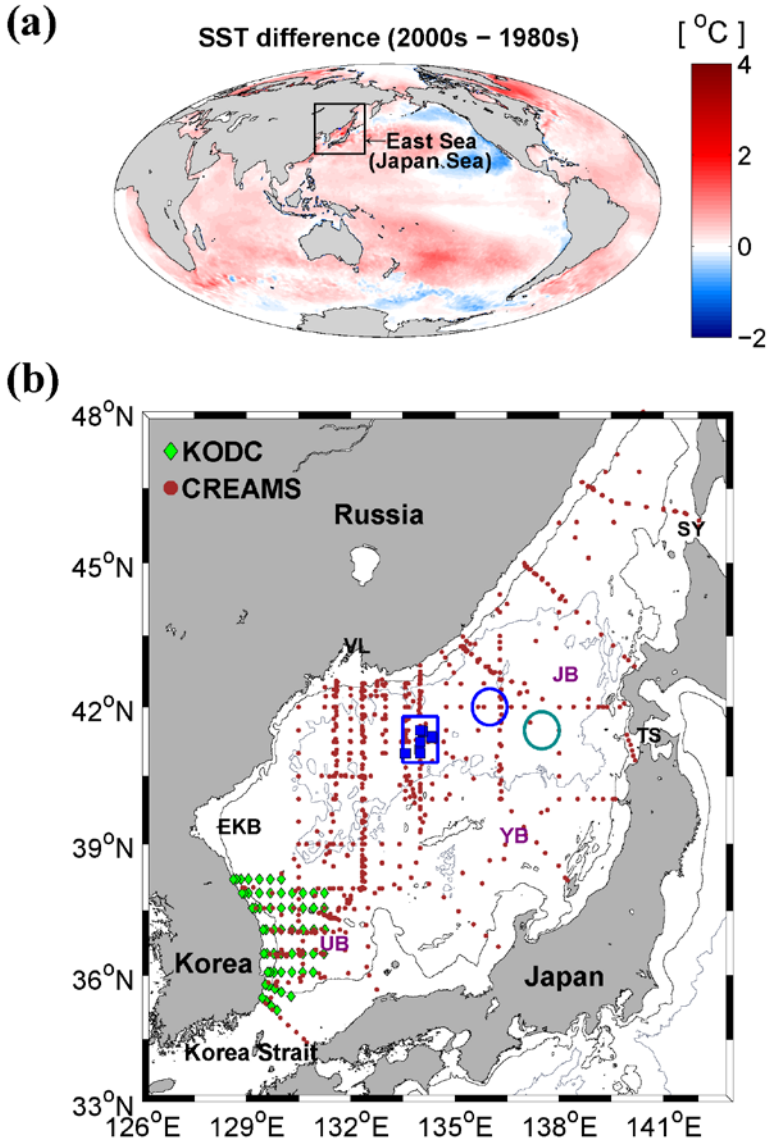

Figure 1.3. (a) Global sea surface temperature (SST) difference map between the 2000s and the 1980s with 0.1 ℃ color interval. A black box indicates the East Sea (Japan Sea). (b) The green diamonds denote stations of KODC (Korea Oceanographic Data Center) data and brown dots indicate stations where the hydrographic data were collected through the CREAMS (Circulation Research of the East Asian Marginal Seas) or EAST (East Asian Seas Time-series)-I cruises. A 500 m (3,000 m) isobaths is

represented with grey (black) contours. Also shown are three basins of the East Sea deeper than 2,000 m, the Japan Basin (JB), the Ulleung Basin (UB), and the Yamato Basin (YB). The data collected in the central JB or the Station C (centered around 134°E, 41.3°N, blue squares) are mainly used here. Other stations in the eastern JB are also remarked with blue and green circle, respectively. VL, EKB, SY and TS denote Vladivostok, East Korea Bay, Soya Strait and the Tsugaru Strait.

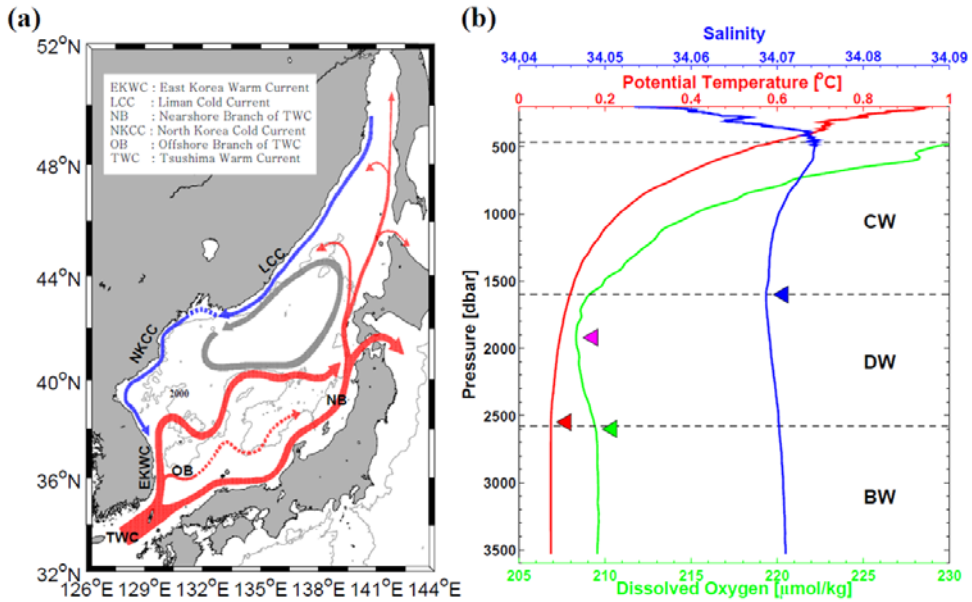

Figure 1.4. (a) Major surface currents of the East Sea with red denoting warm currents, blue cold currents, and grey subpolar gyre [Park et al., 2013]: East Korea Warm Current (EKWC), Offshore Branch (OB) and Nearshore Branch (NB) of the Tsushima Warm Current (TWC), North Korea Cold Current (NKCC), and the Liman Cold Current (LCC). A 2,000 m isobaths is denoted by grey contours. (b) Vertical profiles of potential temperature (red), salinity (blue), and dissolved oxygen (green) observed at Station C in October, 2005. The pressure range is from 200 to 3,600 dbar. A blue (magenta) arrow indicates a deep salinity (dissolved oxygen) minimum depth. An upper limit of benthic homogeneous layer detected in potential temperature (dissolved oxygen) profile is denoted by a red (orange) arrow. The layer between 0.6 ℃ isotherm and a deep salinity minimum depth is defined as Central Water (CW). Bottom Water (BW) is located within a benthic homogeneous layer and Deep Water (DW) is existed between CW and BW.

1.3. Previous works

1.3.1. Ocean heat content change

The ocean is a large heat reservoir and ocean heat content (OHC) plays a major role in heat balance of the Earth system [Levitus et al. 2000, among others]. The global OHC has experienced dramatic changes in recent decades [Levitus et al., 2000; 2005; 2012]. Especially, warming in the upper 700 m of the global ocean accounts for about 70% of heat increase in the upper 2,000 m layer, indicating importance of understanding how the upper ocean heat content varies in time [Levitus et al., 2012] (Figure 1.2).

The OHC variation can be described in terms of three processes: pure warming, pure heaving, and pure freshening [Bindoff and Mcdougall, 1994]. Because pure warming uniformly contributes to the heat content changes worldwide, Palmer et al. [2007] and Palmer and Haines [2009] introduced a new concept of relative heat content, which is the heat content changes relative to a fixed isotherm. They separated the relative heat content into depth and temperature contributions and revealed that the deepening or shoaling of a fixed isotherm is locally important, although the heaving effect is canceled out when it is spatially averaged on a global scale. The important contribution of the pure heaving effect to the OHC on a regional scale has been reported in various regions [Visbeck, 2003; Roemmich et al., 2007; Gille, 2008; Hill et al., 2008; Lozier et al., 2008].

Smaller marginal seas have also experienced the OHC variations, and pure heaving effect would also be important in the

marginal seas if ocean circulation controls isotherm changes over the region [e.g., Song et al., 2014]. The linear warming trend of non-seasonal OHC in the ES was shown to be about two times higher than those in the global and Pacific Oceans according to Na et al. [2012] (see Table 3.1).

Long-term OHC variability of the ES in the upper 300 m was reported to show a warming trend during 1968–2007 based on observational dataset, and the trend is superimposed on a major decadal fluctuation associated with the Northwestern Pacific decadal variability [Na et al., 2012]. They suggested that the decadal upper OHC variation in the ES is related to the 10 ℃ isotherm depth fluctuations reflecting the variability of the TWC mainly in the eastern part of the ES. However, I noted a spatial inhomogeneity of the long-term trend of OHC variations, a fast warming trend in the northeastern part and a slow cooling trend in the southwestern ES [see Figure 2 in Na et al., 2012], which was unaddressed and unexplained in Na et al. [2012]. Their cyclostationary empirical orthogonal function analysis depicted a dominant non-seasonal mode that reflects mainly the warming trend in the eastern ES because of its fast warming rate as compared to the weak cooling trend in the western ES.

While overall warming has been reported in the ES [Kim et al., 2008; Yeh et al., 2010; Na et al., 2012], the observed cooling trend localized in the Ulleung Basin is a very striking phenomenon and deserves more detailed investigation and explanation. Minobe et al. [2004] also suggested that the different mechanisms caused subsurface temperature (0–400 m) variations in the southwestern and northeastern ES from 1957 to 1996. Positive northward wind stress anomalies along the Eurasia coast are mainly responsible for

an interannual temperature variation in the southwestern ES, while a decadal temperature variation in the northeastern ES is mainly associated with changes in the strength of the Siberian High. However, it is not very clear how the local wind induces the subsurface temperature variation.

1.3.2. Deep ventilation change

Slowing of the meridional overturning circulation (MOC) associated with changes in the ocean ventilation system due to global warming has been reported since the late 1900s [Stocker and Wright, 1992; Manabe and Stouffer, 1993; Stocker and Schmittner, 1997; Hofmann and Rahmstorf, 2009; Rahmstorf et al., 2015]. Hydrographic observations at a transatlantic section along 25°N have suggested the slowdown of the Atlantic MOC (AMOC) during 1957–2004 [Bryden et al., 2005] and continuous mooring records collected from 2000 to 2009 at 16°N suggested a significant and consistent decrease of the southward volume transport of the North Atlantic Deep Water [Send et al., 2011]. Ocean or ocean-atmosphere coupled model simulations with scenarios of anthropogenic CO_2 increasing, predict that the AMOC will significantly slow down after several decades [Rahmstorf et al., 2015]. However, the stability of the AMOC is quite sensitive to the hydrological cycle [Stocker and Wright, 1992; Hofmann and Rahmstorf, 2009] as well as the rate of CO_2 increase [Manabe and Stouffer, 1993; Stocker and Schmittner, 1997; Yamamoto et al., 2015]. At the multi-millennium time scale, continued warming would enhance deep ventilation in the Southern Ocean [Yamamoto et al., 2015]. Nevertheless, future changes in MOC remain uncertain

because the feedback mechanisms between ocean-atmosphere system and the global warming are, in fact, diverse and complex [Seidov et al., 2001].

Considering the structures of deep-water masses, ventilation in the ES has been maintained with significant changes since the 1950s [Kim and Kim, 1996; Gamo et al., 2001; Kim et al., 2001; Kang et al., 2003b; 2004a; 2004b; Kim et al., 2004; Kim et al., 2008]. Due to its rapid overturn, compared to that in the global ocean, with timescale of the order of only decades [Kim et al., 2001; Kumamoto et al., 1998] and strong sensitivity to formation process of water masses [Kim et al., 2001; Talley et al., 2003] well isolated from all subsurface waters in the Pacific, changes in the ventilation system of the ES would provide an important implication on the future changes in MOC under the global warming. Results of the moving boundary box model (MBBM) suggested a shift in ventilation from the bottom to central/deep layers, resembling the weakening of deep ventilation in the global ocean [Kim and Kim, 1996]. Gamo et al. [2001] also suggested an upward shift of the deep ventilation using geochemical tracers, DO, and nutrients data during 1984–1998. Such shifts provide a clue to future changes in the global ocean [Manabe and Stouffer, 1993; Stocker and Schmittner, 1997; Kim et al., 2001]. It was even reported that the ES would become anoxic ocean due to decreasing of the BW formation [Gamo, 1999; Chen et al., 1999]. The BW was actually predicted to completely disappear by the 2030s as the CW replaces the BW [Kim and Kim, 1996]. However, the projection was slightly modified from the hydrographic data collected in 1990s' where the BW would no longer exist in 2040, with use of updated coefficients for the MBBM [Kang et al., 2003b] and the total oxygen content

would be maintained with oxygen supply into the CW [Kang et al., 2004b].

Despite these predictions, a sudden BW formation by a deep slope convection along the continental slope in the Peter the Great Bay was observed during the severe winter 2000–2001 [Kim et al., 2002b; Lobanov et al., 2002; Senjyu et al., 2002; Tsunogai et al., 2003]. A percentage of this replenishment was estimated 3 to 8 % of the BW [Kim et al., 2002; Tsunogai et al., 2003; Kang et al., 2004]. Cui and Senjyu [2012] reported that DO in the CW at the Yamato Basin also has been decreased contrary to the previous studies. Moreover, the MBBM projections suggested 13 years ago have not been diagnosed with more recent observations.

1.4. Main purposes

As mentioned in the previous studies, the east-west contrast of upper OHC variation south of the subpolar front in the ES was poorly understood and there was no quantitative access to explain the upper OHC variations. Moreover, the mode shift from bottom to intermediate/deep layers reported in the mid–1990s was thought to be related with the global warming but recent ES ventilation system change had yet to be reconfirmed by analyzing the data collected after this period.

Thus, in this study, the regional variation of the non-seasonal upper ocean (0–500 m) heat content (HCA) in the ES between 1976 and 2007 is re-visited using one additional data set from KODC (Korea Oceanographic Data Center) covering near-coastal region in the southwestern ES together with data used in Na et al. [2012]. It is reconfirmed that the HCA variation in the ES is mainly

determined by the upper ocean circulation change through using the decomposition method. In addition, causative mechanisms are sought for the east-west contrast of the HCA in south of the subpolar front of the ES previously documented but insufficiently explained.

To figure out recent changes of the ventilation system in the deep layer, the MBBM projections were documented 13 years ago, and are re-visited with recent observations. Temporal changes in the ventilation system are demonstrated with structures and volumes of deep-water masses (CW, DW, and BW) by analyzing the hydrographic data collected between 1993 and 2016 (19 cruises in total). Then, the future ventilation is newly projected based on 1-D advection-diffusion model and their association with winter ocean-atmosphere conditions in the northern ES is discussed.

Finally, I will discuss about overall variations of physical properties of seawater in the ES by synthesizing the results of upper ocean heat content and deep ventilation system changes. Moreover, as discriminating between the changes by warming effect and non-warming effect, I will suggest another implication of these results for the global ocean.

In this dissertation, most parts are written by referring two papers; One is “An east-west contrast of upper ocean heat content variation south of the subpolar front in the East/Japan Sea” published Journal of Geophysical Research: Oceans in 2016 and the other is “Re-initiation of bottom water formation in the East Sea (Japan Sea): Another clue to future changes in global ocean?” submitted to Scientific Reports and peer reviewing from June 22, 2017.

2. Data and Methods

2.1. Data

The HCA in the ES is calculated based on two observational temperature datasets: monthly mean temperature data from 1976 to 2007 used by Na et al. [2012] (NA12 data hereafter) and bimonthly KODC data from 1976 to 2011. The NA12 and KODC data are available in the upper 1,000 m and 500 m, respectively. Temperature in both datasets is arranged at 14 vertical levels (0, 10, 20, 30, 50, 75, 100, 125, 150, 200, 250, 300, 400, 500 m).

The NA12 data is based on temperature profiles collected in the World Ocean Database 2005 [WOD; Boyer et al., 2006], and it is quality-controlled, spatially and temporally smoothed data by the optimal interpolation scheme with a horizontal resolution of 0.5° [Minobe et al., 2004; Na et al., 2012]. Although the NA12 data covers a large area of the ES, I use NA12 data only south of 42°N because of a paucity of data in the northern ES.

The KODC data (http://kodc.nifs.go.kr) is in situ data that covers the Ulleung Basin including coastal area. The KODC data is based on bimonthly surveys in the southwestern ES from February to December conducted by the National Institute of Fisheries Science (NIFS) at fifty-eight stations (Figure 1.3b). The KODC data well covers the coastal area west of 130°E (Figure 1.3b) with higher spatial resolution of about 0.1° near the coast and relatively coarser resolution of about 0.3° offshore in the zonal direction. The horizontal spacing of the NIFS stations in the meridional direction is 0.5°. For quality control of the KODC data, the downloaded digital

data values are compared with tabulated values in annual reports published by the NIFS. Some data collected in odd months are linearly interpolated to locate them at the same even month intervals. Missing values from 1978 to 1981 are found at one station (36° 30′N, 130° 18′E), which are then filled with climatological bimonthly mean values. Regional temperature range outliers based on properties of the water masses in the ES [Kim et al., 2004] are removed and filled by linear interpolation in the vertical.

The two temperature datasets are linearly interpolated at every one meter interval to calculate the heat content. For stations shallower than 500 m, the heat content calculation is made down to observed deepest depths. Both NA12 and KODC salinity data are also used together with temperature data to calculate dynamic height anomaly (geopotential height anomaly divided by the acceleration of gravity) at surface relative to 500 m. For stations shallower than 500 m in KODC data, the reference level is taken as the maximum depth of available data. Quality control processes of KODC salinity data is the same as those of temperature data.

The hydrographic data used here were collected using the Conductivity-Temperature-Depth (CTD) instruments via 19 research cruises between 1993 and 2016 (Table 2.1) conducted through CREAMS (Circulation Research of the East Asian Marginal Seas) or EAST (East Asian Seas Time-series)-I programs. The CTD stations cover most parts of the ES, particularly the deepest part (deeper than 3,000 m) or middle of the JB in the north (Figure 1.3b). During the cruises, full-depth or shallow CTD casts were conducted at each station, and seawater samples were often collected at multiple discrete depths to analyse DO and other

variables. Details on the hydrographic measurements are summarized in Table 2.1. The data collected at all the stations were analyzed and compared, and here the results obtained particularly from the measurements at a group of stations (referred as station C) located in the central JB (centered around 134°E, 41.3°N; blue squares in Figure 1.3b) are shown to examine the structures and volumes of deep-water masses as the station was occupied by nearly all the cruises since 1990s [Kim and Kim, 1996; Kim et al. 2004]. It is noticed that the station C clearly represent the structural changes of deep-water masses in the ES with consistent results of 1-D advection-diffusion model.

Ancillary datasets used to understand the heat content variation include the Modern-Era Retrospective Analysis for Research and Applications (MERRA) daily wind at 10 m height (http://disc.sci.gsfc.nasa.gov/daac-bin/DataHoldings.pl) and the optimally-interpolated (version 2) Advanced Very High Resolution Radiometer (AVHRR) daily sea surface temperature (SST) data [Reynolds et al., 2007]. The MERRA wind data ($\overrightarrow{V_{10m}}$) from 1979 to 2011 has a spatial resolution of 1/2°×2/3°, and it is used for calculating the wind stress curl. The daily wind stress is calculated as $\vec{\tau} = \rho_{air} C_D \overrightarrow{V_{10m}} \left|\overrightarrow{V_{10m}}\right|$ ($\rho_{air} = 1.22$ kg/m^3), and C_D is computed following Large and Pond [1981]. Based on the MERRA daily wind data from 1979 to 2011, the monthly WSC is computed. Then wind stress curl anomaly (WSCA) is obtained by subtracting record-length monthly mean WSC from monthly mean WSC of each year, respectively. Winter WSCA is constructed by averaging the WSCA from December to February (DJF). Monthly mean SST data is produced using the daily AVHRR data available from 1982 to 2011 with a spatial resolution of 1/4°×1/4°. The monthly SST anomaly is

computed by subtracting the record-length monthly mean SST from the monthly mean SST for each year. Weekly sea surface height (SSH) data from 1993 to 2011 are also used to compute surface geostrophic currents and compare them with those calculated from dynamic heights. Moreover, SSH data are used for checking development of the subpolar gyre in the northern ES. The SSH field (1/4°×2/4°) is constructed from sea level anomalies obtained from Archiving, Validation and Interpretation of Satellite Oceanographic data (AVISO, http://www.aviso.altimetry.fr/duacs) and mean dynamic topography [Lee et al., 2009].

Two climate indices are examined to find causative atmospheric forcing for the heat content variation. The DJF Siberian High (SH) index is obtained from Pak et al. [2014], which is defined as area-mean sea level pressure anomalies over the SH center (45–55°N, 85–105°E). The SH together with a strong Aleutian Low to its east exerts direct and significant influences on northwesterly winds in East Asia during the winter [e.g., Wu and Wang, 2002]. Also, I examined the DJF Western Pacific teleconnection pattern (WP) index available from the National Oceanic and Atmospheric Administration Climate Prediction Center (http://www.cpc.ncep.noaa.gov/data/teledoc/wp.shtml). The WP reflects zonal and meridional variations in the position and strength of the East Asian jet stream in the entrance region of the Pacific. The WP index is derived by applying the rotated principal component analysis technique to the monthly mean standardized 500 hpa height anomalies in the 20–90°N.

Monthly mean AVHRR SST data and the MERRA2 monthly data [GMAO, 2015] from 1980 to 2016 with 0.5°×0.625° which contain surface heat fluxes, air temperature, evaporation, and precipitation

are used to identify winter sea surface conditions associated with deep-water formations in the northern ES. Monthly sea ice concentration data with a grid cell size of 25×25 km from Nimbus-7 SMMR, DMSP SSM/I-SSMIS Passive Microwave data provided at the National Snow and Ice Data Center (NSIDC) [Cavalieri et al., 2015] are used to quantify the sea surface salinity change relevant to brine rejection in the vicinity of the Tartarsky Strait. Winter sea ice concentration is calculated by averaging data from November to February for cases when the concentration exceeded 15 % only [Cavalieri et al., 1992]. The mixed layer depth (MLD) is determined using hydrographic data collected in the northern ES via CTD casts, profiling floats, eXpendable Bathy Thermograph, and the WOD 2005 during 1995–2004. For this purpose, a threshold of temperature difference $\Delta T = 0.2$ ℃ and a reference depth of 10 m were set following Lim et al. [2012]. The MLD in the northern ES is increased from November and the thickened layer is maintained until the following March [Lim et al., 2012]. Thus, the winter MLD is investigated from November to March and a total of 2210 MLDs in winter is used in this study.

Table 2.1. Information on CREAMS or EAST-I cruises between 1993 and 2016. *T*, *S*, and DO denote water temperature, salinity, and dissolved oxygen, respectively.

CREAMS cruise date	Observation Instrument	# of Stations	Observed variables	Pre- and Post-calibration	DO calibration	Remark	Reference
Aug. 12–19, 1993	SBE911 [a]	69	*T*, *S*			CTD casts down to 1,000dbar	Kim et al. [2004]
Jul. 10–21, 1994	SBE911	51	*T*, *S*				Kim et al. [2004]
Mar. 1–7, 1995	SBE911	35	*T*, *S*				Kim et al. [2004]
Jul. 24–Aug. 8, 1995	SBE911	45	*T*, *S*				Kim et al. [2004]
Feb. 17–24, 1996	SBE911	26	*T*, *S*				Kim et al. [2004]
Aug. 1–11, 1996	SBE911	35	*T*, *S*, DO				Kim et al. [2004]
Mar. 20–Apr. 8, 1997	SBE911	67	*T*, *S*, DO				Kim et al. [2004]
Feb. 22–Mar. 8, 1999	SBE911	43	*T*, *S*				Kim et al. [2004]
Jun. 14–Aug. 13, 1999	NBMK [b]	203	*T*, *S*, DO		O		Talley et al. [2003; 2004]
Feb. 2–Mar. 17, 2000	NBMK	81	*T*, *S*				Talley et al. [2003; 2006]

Apr. 16–20, 2001	NBMK	19	*T*, *S*				Lobanov et al. [2002]
Apr. 7–26, 2002	SBE911p [c]	15	*T*, *S*				
Oct. 15–27, 2005	SBE911p	43	*T*, *S*, DO	O			
May 10–20, 2007	SBE911p	23	*T*, *S*, DO				Kim et al. [2008]
Jul. 8–19, 2009	SBE911p	38	*T*, *S*, DO				
Oct. 13–27, 2012	SBE911p	42	*T*, *S*, DO	O	O	1 Hz data sampling [d]	
Apr. 15–29, 2014	SBE911p	28	*T*, *S*, DO	O	O		
Apr. 6–May 3, 2015	SBE911p	36	*T*, *S*, DO	O	O		
Apr. 5–15, 2016 [e]	SBE911p	23	*T*, *S*, DO			South of 40.5°N, West of 132.5°E	

[a] Sea-Bird Electronics 9 CTD unit and Sea-Bird Electronics 11 deck unit

[b] Neil Brown Instrument Systems MKIIIB CTD unit

[c] Sea-Bird Electronics 9plus CTD unit and Sea-Bird Electronics 11plus V2 deck unit

[d] Data sampling frequency of SBE911p is generally 24 Hz.

[e] A calibration date of the DO sensor is Feb. 5, 2016

2.2. Methods

2.2.1. Heat content calculation and decomposition

The heat content calculation follows the method of Palmer et al. [2007] and Palmer and Haines [2009]. Let the temperature data be defined by T(p,z,y,m) with p (= 1,2,⋯,P) for stations, z (= 0,1,2, ⋯,14) for depth levels, y (= 1,2,⋯, Y) for years, and m (= 1,2, ⋯,12 (NA12 data) and 2,4,⋯,12 (KODC data)) for months. The heat content from surface (z = 0) to the maximum depth ($z = H(p) \leq$ 500 m) of available data at station p, $Q_0^{H(p)}$, can be written as

$$Q_0^{H(p)}(p,y,m) = \bar{\rho} C_p H(p) T_H(p,y,m),$$

where $T_H(p,y,m)$ denotes the average temperature between sea surface and H(p). The $\bar{\rho}$ (density) and C_p (heat capacity) are constants values based on temperature and salinity that are averaged over whole periods and domain. Seawater density ranges from 1020 to 1030 kg/m^3 in the study region, and then $Q_0^{H(p)}$ changes by less than 1% for the density range.

$Q_0^{H(p)}(p,y,m)$ is further divided into four components based on isotherms representing water mass properties in the ES. Following Kim et al. [2004], temperature ranges of the TWW, ESIW, and JSPW are selected: temperatures over 10 ℃ (TWW layer), 5–10 ℃ (thermocline layer), 1–5 ℃ (ESIW layer), and temperatures below 1 ℃ (JSPW layer). Then, $Q_0^{H(p)}(p,y,m)$ can be written as

$$Q_0^{H(p)}(p,y,m) = \sum_{i=1}^{4} Q_i(p,y,m) = \bar{\rho} C_p \sum_{i=1}^{4} H_i(p,y,m) T_i(p,y,m),$$

where $Q_i(p,y,m)$ (subscript i denotes the i-th layer, i = 1,2,3,4) denotes heat content in each temperature range, and $H_i(p,y,m)$ and $T_i(p,y,m)$ denote the thickness and depth-averaged temperature of

each temperature range. Each T_i and H_i can be decomposed into seasonal and non-seasonal parts as

$$T_i(p,y,m) = T_i'(p,y,m) + \overline{T_i}(p,m)$$

[$\overline{T_i}(p,m) = \frac{1}{Y}\sum_{y=1}^{Y} T_i(p,y,m)$, the climatological monthly mean temperature]

$$H_i(p,y,m) = H_i'(p,y,m) + \overline{H_i}(p,m)$$

[$\overline{H_i}(p,m) = \frac{1}{Y}\sum_{y=1}^{Y} H_i(p,y,m)$, the climatological monthly mean thickness]

Then, $Q_0^{H(p)}(p,y,m) = \overline{\rho} C_p \sum_{i=1}^{4} (\overline{H_i} + H_i')(\overline{T_i} + T_i')$

$$= \overline{\rho} C_p \sum_{i=1}^{4} \overline{H_i}\,\overline{T_i} + \overline{\rho} C_p \sum_{i=1}^{4} (\overline{T_i} H_i' + \overline{H_i} T_i') + \overline{\rho} C_p \sum_{i=1}^{4} H_i' T_i'$$

The first term represents the seasonal variation of the heat content, and the last term is negligibly small as compared with other components. Hence, the HCA in the upper 500 m can be written as

$$HCA = Q_0^{H(p)}(p,y,m) - \overline{\rho} C_p \sum_{i=1}^{4} \overline{H_i}\,\overline{T_i} \approx \overline{\rho} C_p \sum_{i=1}^{4} (\overline{T_i} H_i' + \overline{H_i} T_i')$$

In addition, HCA in each temperature range becomes

$$\text{HCA of i-th layer} = \overline{\rho} C_p \overline{T_i} H_i' + \overline{\rho} C_p \overline{H_i} T_i'$$

As discussed by Bindoff and Mcdougall [1994], among the two terms in the above equation, the former represents an effect of pure heaving (hereafter, $\overline{T}H'_i$) and the latter can be regarded as an effect of pure warming (hereafter, $\overline{H}T'_i$). While HCAs above the JSPW layer represent HCAs in full layers occupied by the TWW, thermocline, and the ESIW, respectively, HCA of R_4 represents only a part of the HCA contained in the JSPW from 1 ℃ isotherm to 500 m depth.

Percentage of the variance is also calculated to quantify the

contribution of each decomposed component to the variation of total HCA. The percent of variance of $\overline{TH}'_i$ (i = 1, 2, 3, 4) is defined as

$$100\times(a) / \sum_{i=1}^{4}[(a)+(b)], \text{ where}$$

$$(a) = \sum_{y}\sum_{m}\{P^{-1}\sum_{p}\left(\overline{TH}_i'\right)\}^2 \quad \text{(Variance of heaving part)}$$

$$(b) = \sum_{y}\sum_{m}\{P^{-1}\sum_{p}\left(\overline{HT}_i'\right)\}^2 \quad \text{(Variance of warming part)}$$

The HCA calculation with the spatially non-uniform KODC data is rectangular in areas associated with temperature profiles at each of KODC stations extending half way to the next station horizontally. After calculating the HCA based on monthly or bimonthly data, a two-year low-pass filter is applied to a time series of the HCA and its decomposed parts using the 4^{th} order Butterworth filter in order to remove short-term variability, which could affect the calculation of long-term trend.

2.2.2. CTD data processing

All CTD data were processed and carefully calibrated with raw data except, for data from 1999 June and 2000 February cruises, for which only preliminary processed data are available (Table 2.1). They were handled using standard data processing programmes, those of Sea-Bird Electronics (SBE), except for the AUTOSAL calibration and pre- and post-cruise sensor calibrations to correct the absolute bias additionally [Talley et al., 2004]. The absolute value of the CTD data were found to be potentially biased (within 0.001 ℃ in temperature and 0.002 in salinity) compared with the final processed data used in Talley et al. [2003; 2004; 2006]. Most CTD data collected after 2002 were processed, with both pre- and

post-cruise sensor calibrations, following typical SBE data processing sequences [Sea-Bird Electronics, 2014] (Table 2.2). Figure 2.1a shows an example for pre-cruise (July, 2012, blue), post-cruise (June, 2014, red), and pre- and post-cruise processed θ−salinity diagram (April, 2014, black) at station C. As confirmed in this figure, the exact value of θ and salinity in an observation period could be obtained through pre- and post-cruise sensor calibration. Although the effects of thermal mass on data quality is generally important [Morison et al.,1994; Kim et al., 2000; Mensah et al., 2009], sensitivity tests with various combinations of input parameters indicate that final processed salinity and temperature below 500 m are nearly insensitive to the CellTM process, yielding an Root Mean Square (RMS) difference of less than the sensor accuracy (0.001 ℃ in temperature and 0.001 in salinity) (Figure 2.1b). More details about CTD data processing methods are explained in EAST-I Atlas [2016]②.

For cases where post-cruise calibration was unavailable, sensor drift calibration and pre-cruise calibration were applied to correct absolute values of salinity and temperature. The DO sensor data were calibrated using DO titrated from bottle samples by the Winkler method for cruises conducted in 1999, 2012, 2014, and 2015 (Figure 2.2). The equations and information for calibrated DO profiles at each cruise can be checked in Table 2.3.

For cases without bottle samples, DO profiles were calibrated by a drifting rate of the DO at 3,000 dbar assuming that BW DO linearly decreased between the periods [Gamo, 2011]. The DO profiles observed in August, 1996, March 1997, October, 2005, May,

② This book was non-officially published in May 31, 2016 by Research Institute of Oceanography, Seoul National University.

2007, and July, 2009 are drifted −17.13, −13.27, +9.18, +6.97 and +69.67 μmol/kg, respectively. Final-calibrated DO profiles at the station C during 1996–2015 are shown in Figure 2.3.

Table 2.2. SBE Data Processing sequences referred to Sea Bird-Electronics [2014]

SBE Data Processing	
CTD Raw data →	Data Conversion → Section → Wild Edit → Filter → Loop Edit → Align CTD → *CellTM → 1 dbar & 1 m Binaverage → Derive → Ascii Out

* Calculate a CTD thermal lag correction amplitude (α) and a time constant (τ or $1/\beta$) followed by Morison et al. [1994]

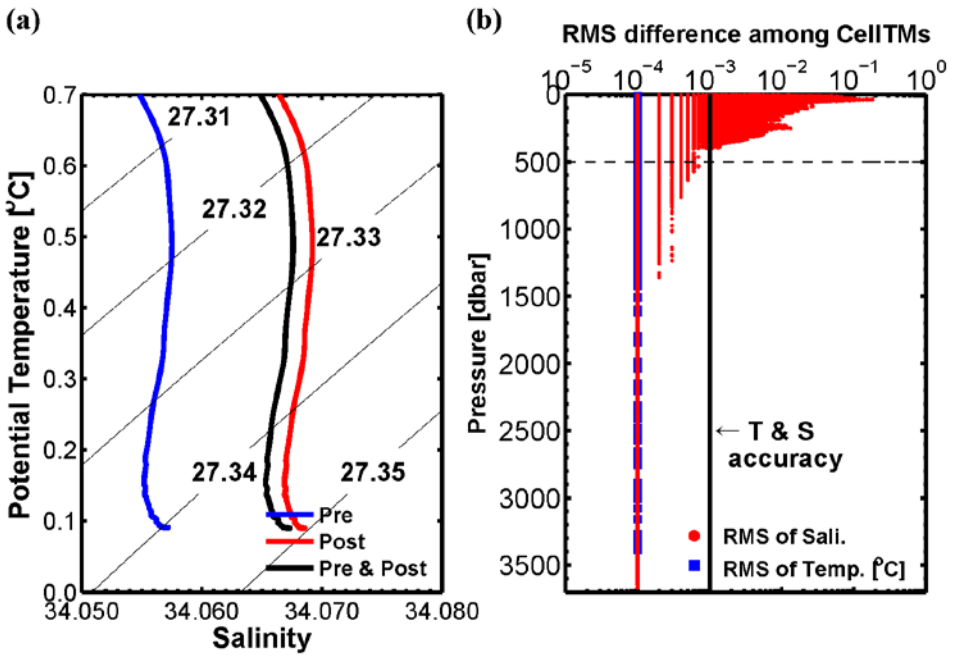

Figure 2.1. (a) Potential temperature ($\boldsymbol{\theta}$) – salinity (S) diagram at Station C with potential density contours observed in April, 2014. Pre (Post) - cruise calibrated sensor's data are represented by a blue (red) line. The data applied a pre- and post-cruise calibration is indicated by a black line. (b) RMS (Root Mean Square) difference among salinity (red dots) and temperature (blue squares) processed by four CellTM processes: Morison et al. [1994], Kim et al. [2000], Mensah et al. [2009], and Sea-Bird Electronics [2014]. Black solid line denotes an accuracy of temperature (T) and salinity (S). The x-axis for RMS difference is represented by a log-scale. Data of six cruises are used in this test: Oct., 2005; May, 2007; Jul., 2009; Oct., 2012; Apr., 2014; Apr., 2015.

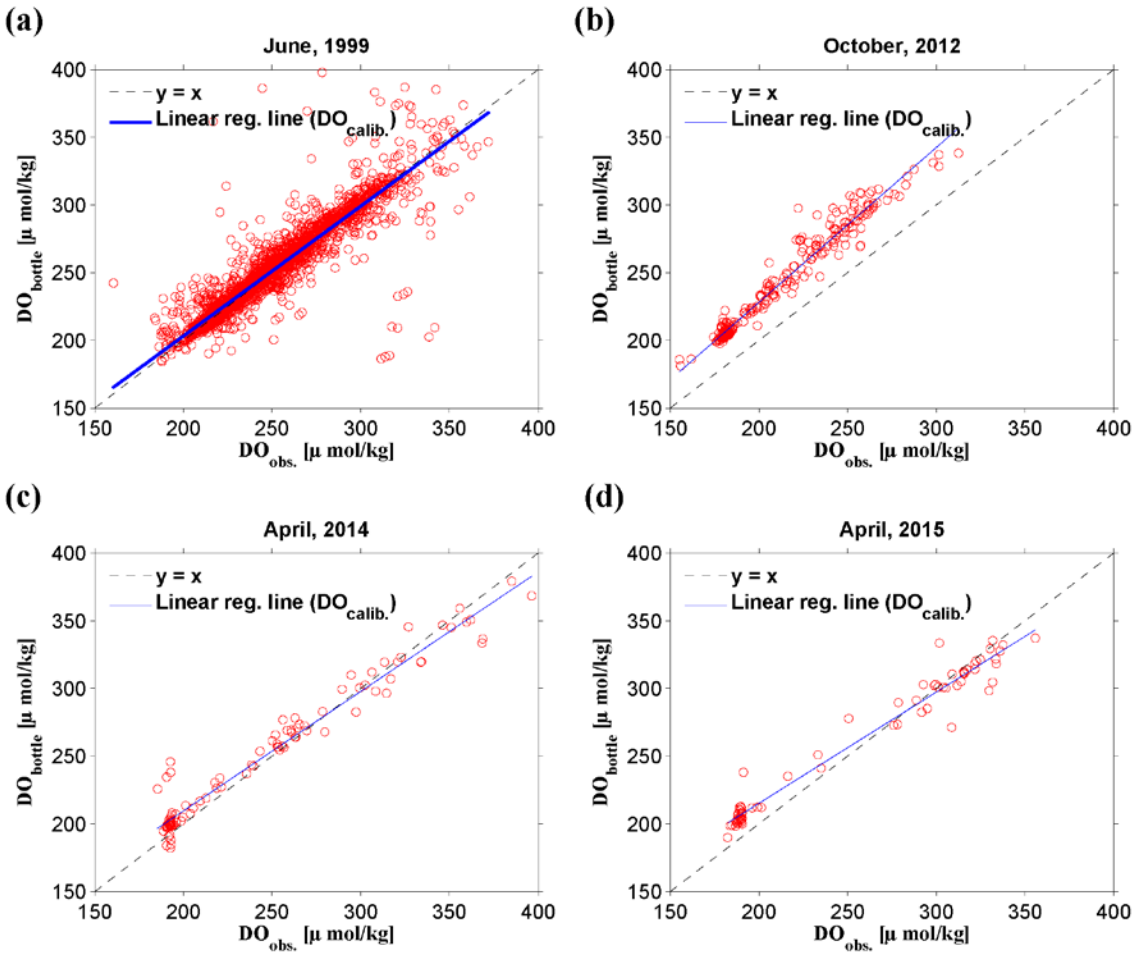
(a)
June, 1999
(b)
October, 2012
(c)
April, 2014
(d)
April, 2015
y = x
Linear reg. line (DO calib.)
DO bottle [μ mol/kg]
DO obs. [μ mol/kg]
150
200
250
300
350
400

Figure 2.2. (a) Relation between CTD dissolved oxygen (DO) sensor data ($DO_{obs.}$) and Winker bottle samples (DO_{bottle}) observed at June, 1999 (red dots). A blue line indicates a linear regression line obtained by using two variables (predictor = $DO_{obs.}$, dependent variable = DO_{bottle}) (b) The same as Figure 2.2a, but for October, 2012. (c) The same as Figure 2.2a, but for April, 2014. (d) The same as Figure 2.2a, but for April, 2015.

Table 2.3. Equations for calibrated DO profiles estimated with Winkler bottle samples and full-depth DO profiles at four cruises together with number of the bottle samples and RMS difference between the bottle data and CTD DO profiles.

Cruise date	Equation for calibrated DO profiles [μmol/kg]	RMS difference between Winkler bottle samples and full-depth DO profiles [μmol/kg]	Number of Winkler bottle samples
June, 1999	$DO_{calib.} = 0.96 \times DO_{obs.} + 11.24$	11.71	3,616
October, 2012	$DO_{calib.} = 1.14 \times DO_{obs.} - 0.72$	30.46	304
April, 2014	$DO_{calib.} = 0.88 \times DO_{obs.} - 32.98$	13.41	103
April, 2015	$DO_{calib.} = 0.82 \times DO_{obs.} + 50.80$	15.54	75

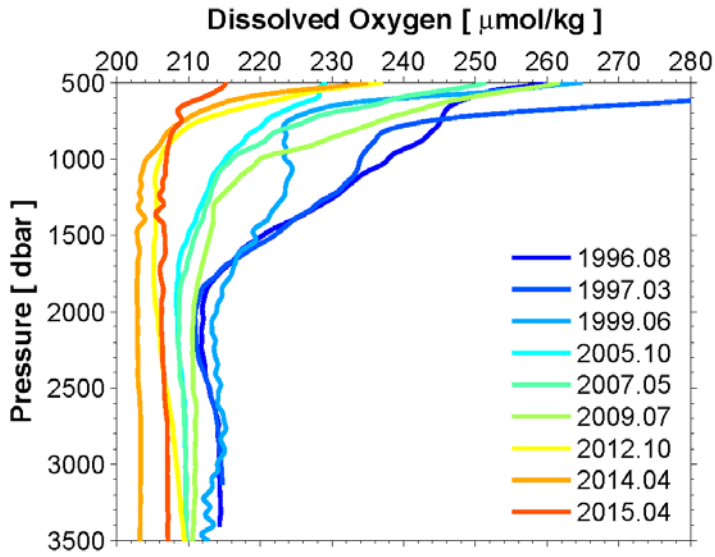

Figure 2.3. Final-calibrated DO profiles at Station C from 1996 to 2015.

2.2.3. Finding deep structures

The DSM is defined as a depth where salinity reaches its local minimum in the range of 600–3,000 m, as considered previously [Kim et al., 1996]. The depth uncertainty was estimated from depths where the difference in salinity at the DSM becomes 0.0001 (salinity resolution). The DSM in 2012 was much deeper than DSMs in the other years, which is partly because the CTD were not obtained at a sufficiently high sampling rate during that particular cruise (Table 2.1). The UBHL as a DW-BW boundary was estimated at vertical θ gradient of less than 0.001 ℃ (temperature accuracy) per 100-m range (typical number of scan is ~2,400). Its uncertainty range was set from a depth where θ becomes 0.001 ℃ higher than θ at the UBHL. The UBHL was also estimated from calibrated sensor DO profiles following a method previously used [Gamo et al., 1986], which showed no marked difference from UBHL derived using θ profiles (Figure 1.4b).

2.2.4. 1-D advection-diffusion model

The continuity equation for a specific variable q with no consideration of interior horizontal flow is

$$\frac{\partial q}{\partial t} = K\left(\frac{\partial^2 q}{\partial z^2}\right) - w\left(\frac{\partial q}{\partial z}\right) - \lambda q + J$$

Here, the q indicates the variables: θ, S (salinity), and DO (DO); K, w, J, λ, and z are vertical diffusion/mixing coefficient, vertical velocity (always positive), source ($J=0$ for θ and S), radioactive decay and the vertical axis, respectively [Craig, 1969]. It is assumed that a system is in a quasi-steady state mode and

radioactive isotopes are not considered in this equation. Then, a steady state 1-D advection-diffusion equation is given by

$$0 = K\left(\frac{d^2q}{dz^2}\right) - w\left(\frac{dq}{dz}\right) + J$$

A steady state 1-D advection-diffusion model [Munk, 1966; Craig, 1969] was widely used to simply understand thermohaline circulations and vertical distributions of DO with a single mixing parameter. Assuming that the JB is horizontally homogeneous in θ, salinity, and DO due to rapid horizontal mixing with horizontal currents [Kim and Kim, 1996] and the system is in a quasi-steady state mode, an 1-D advection-diffusion model can be applied to account for the changes in deep-water masses from 1950 to 2016 as used in Gamo and Horibe [1983] and Kim and Kim [1996].

Ratios between K and w ($Z^*=K/w$) and between J and w (J/w) are calculated from θ and DO profiles independently. The upwelling ($w > 0$) is inferred from the curvature of θ profile (Figure 2.4b), and the sign of J/w or J involves whether the oxygen is convectively (or for any other mechanism) added or not. The first step for this model is that two layers are chosen for CW and DW considering boundaries among deep-water masses (black dashed line in Figure 2.4a) and a linearity in the θ −salinity plot (red symbols in Figure 2.4a). Then, the θ profile (blue line in Figure 2.4b) in each layer is fitted to the Z^* from 0.2 to 2.0 km with a solution for no source term ($J=0$) (red line in Figure 2.4b). After finding Z^* value for each layer, the DO profile in each layer (blue line in Figure 2.4c) is fitted to J/w from −70 to 70 μmol/kg/km using a solution for a constant J (red line in Figure 2.4c). More detailed methods applied into the model are available in Kim and Kim [1996].

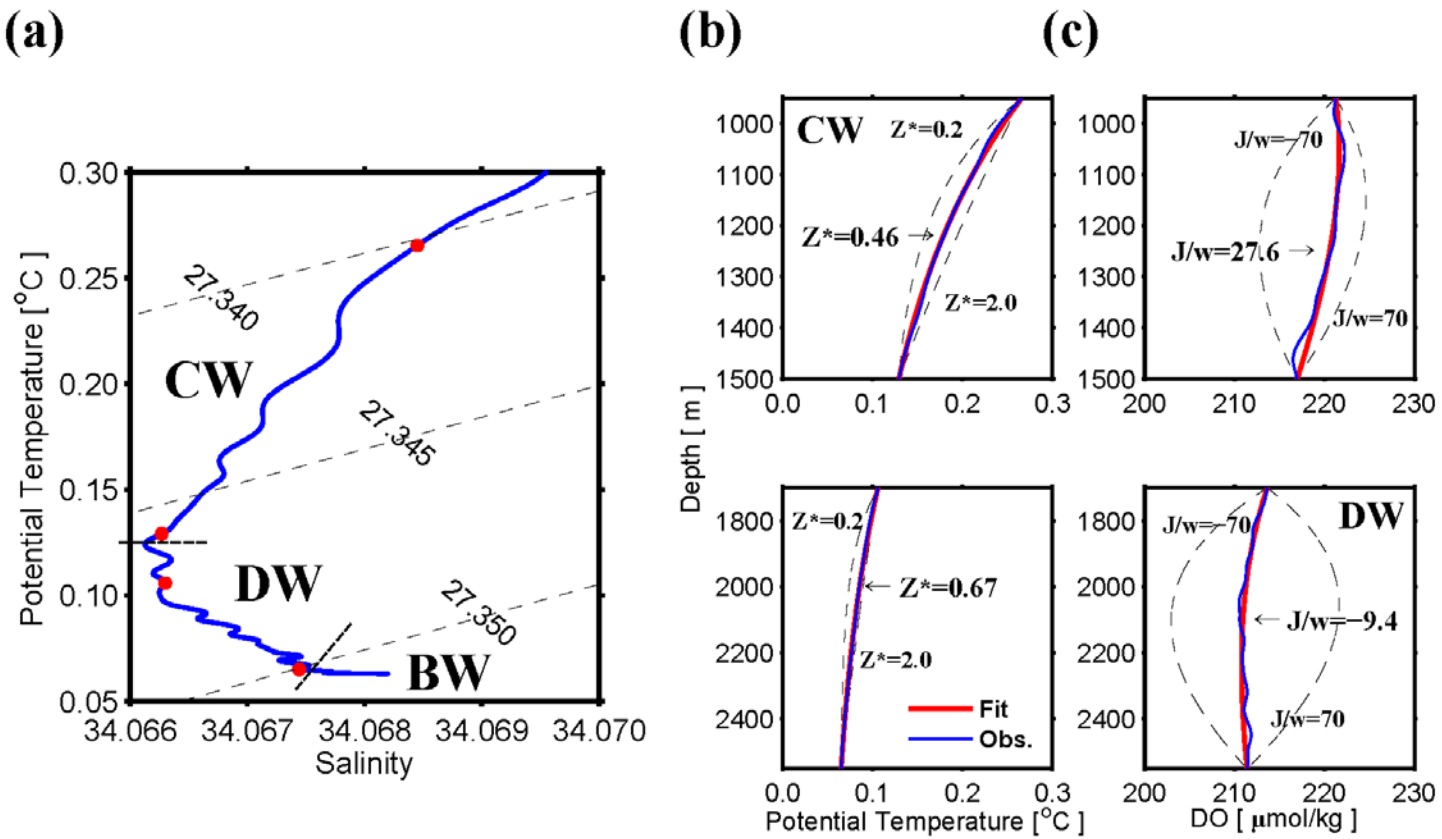
(a)
(b)
(c)
Potential Temperature [°C]
Salinity
0.30
0.25
0.20
0.15
0.10
0.05
34.066
34.067
34.068
34.069
34.070
27.340
27.345
27.350
CW
DW
BW
Depth [m]
1000
1100
1200
1300
1400
1500
1800
2000
2200
2400
CW
Z*=0.2
Z*=0.46
Z*=2.0
J/w=-70
J/w=27.6
J/w=70
Z*=0.2
Z*=0.67
Z*=2.0
Fit
Obs.
DW
J/w=-70
J/w=-9.4
J/w=70
0.0
0.1
0.2
0.3
200
210
220
230
Potential Temperature [°C]
DO [µmol/kg]

Figure 2.4. (a) Potential temperature ($\boldsymbol{\theta}$) – salinity(S) diagram at Station C with potential density contours observed in June, 1999. Solid dashed line marked between CW (DW) and DW (BW) indicates deep salinity minimum (upper limit of benthic homogeneous layer). Red dots in the CW (DW) represent the range of linearity in $\boldsymbol{\theta}-S$ diagram. 1-D advection-diffusion model is applied in these ranges. (b) Results of potential temperature profiles by the 1-D advection-diffusion model. Potential temperature profile in each layer is denoted by a blue solid line and potential temperature profile fitted to Z^* (K/w) is represented by a red solid line. Range of Z^* is from 0.2 to 2.0 km. (c) The same as Figure 2.4b, but for DO profiles. DO profile in each layer is denoted by a blue solid line and DO profile fitted to J/w is represented by a red solid line. Range of J/w is from −70 to 70 **μmol/kg/km**.

2.2.5. Significant level of trend and correlation

Estimates of statistical significance of linear trends and correlation coefficients (r) follow the methods in Emery and Thomson [1997]. When r is calculated using annual time series, the degrees of freedom is chosen as the data length, while linear trend and correlation are estimated using two-year low-pass filtered data, the degree of freedom is calculated by dividing effective decorrelation time scale into data length ($n_{\mathrm{eff}} = n / T_{\mathrm{e}}$). The effective decorrelation time scale (T_{e}) for low-pass filtered time series is calculated following these equations.

$$T_{\mathrm{e}} = 1 + 2\sum_{k=1}^{L} r_{xk} \text{ (trend case)}, \quad T_{\mathrm{e}} = 1 + 2\sum_{k=1}^{L} r_{xk} \bullet r_{yk} \text{ (correlation case)}$$

r_{xk} and r_{yk} mean auto correlation function for variable x and y. L is the first zero crossing of r_{xk} or $r_{xk} \bullet r_{yk}$. Number of degrees of freedom is necessarily not large for low-pass filtered time series, therefore I mainly consider r significant at the 90% confidence limit (CL) as well as the 95% CL.

3. Results

3.1. An east-west contrast of upper ocean heat content variation south of the subpolar front in the ES

The seasonal variation of OHC in the ES mentioned in Na et al. [2012] exhibits a typical variation of the mid-latitude northern hemisphere with maximum in September–October and minimum in February–March. Here, my focus is on the non-seasonal OHC variations in the ES.

The heat content based on the NA12 data is calculated and compared in two areas that represent the southwestern ES (referred to as WEST) and southeastern ES (referred to as EAST) (two black boxes in Figure 3.1a, 3.1b). The EAST represents the region of the fastest warming rate in the southeastern ES and the WEST represents the region of slow cooling rate according to Na et al. [2012]. Hereafter, the whole area covered by the NA12 data is referred to as the EJS, and the region covered by the KODC data is called the UB. About half of the UB stations are included in the WEST, and others lie outside of the WEST and cover the coastal area. The KODC data in the coastal area, however, is also included in the spatially-smoothed NA12 data because the KODC data is included in the WOD.

3.1.1. Characteristics of OHC variations in the ES

3.1.1.1. Linear trend of HCA

Figure 3.1a shows the spatial pattern of a linear HCA trend

between 1976 and 2007 based on NA12 data. The HCA has an increasing trend in a wide area of the EJS, and the maximum warming trend occurs east of 137°E and north of 38°N. However, the HCA in the WEST exhibits a localized cooling trend although it is statistically not significant at the 90% CL. The maximum warming rate in the EAST is twice as fast as the cooling rate in the WEST (Table 3.1). The EAST, where the fast warming of the HCA occurs, also corresponds to the region of fast SST warming trend with a maximum trend of 0.1 ℃/year (Figure 3.1b). On the other hand, SST in the WEST, where the HCA shows cooling trend, exhibits a slow warming trend not attaining the statistically significant level. According to NA12 data, the linear warming trend of HCA in the EJS is about twice as high as those in the global and Pacific Oceans (Table 3.1). The warming rate in the EAST is about twice as fast as that in the EJS, and about four times larger than the global ocean' s trend. Hence, the decreasing trend of HCA in the WEST acts to damp the increasing trend of HCA in the EJS.

An estimate of the linear trend based on the in situ KODC data in the UB yields about a three times faster cooling rate than that in the WEST based on NA12 data (Table 3.1). It is also noted that while the trend in the WEST is statistically insignificant when considering the confidence interval of the trend, the trend in the UB is statistically significant. The HCA trend maps (Figure 3.1a, 3.1c) in an overlapped area between WEST and UB east of 130°E show a 2–3 times faster cooling trend of HCA in KODC data as compared to that based on NA12 data, indicating an underestimate of the cooling trend in NA12 data. Significant cooling trends are observed mainly following the path of the EKWC (Figure 3.1c). If the WEST is replaced with the UB, and the linear trend of HCA in the EJS is re-

calculated, the fast warming rate shown in the EJS based solely on NA12 data disappears. Virtually, there exists no trend in the HCA ($-0.02 \pm 1.23 \times 10^6$ J/m^2/month). These differences in the HCA trend in the overlapped area and in the EJS are thought to arise from the spatial smoothing and missing data in the coastal region affected by the EKWC in NA12. It is confirmed by time series of HCA in the overlapped region shown in Figure 3.1c based on the NA12 data, original uneven KODC data, gridded KODC data, and spatially-smoothed KODC data (Figure 3.3e). The gridded KODC data is prepared by spatially interpolating the KODC data in 0.2°×0.5° grids in the overlapped area, and then the gridded KODC data is spatially smoothed using the Gaussian filter (with standard deviation, σ = 10) to produce the smoothed KODC data. The spatial smoothing is performed only with the KODC data inside the overlapped area. The time series of uneven and gridded KODC data match well, and show larger amplitudes of HCA as compared to that in NA12 data (Figure 3.3e). The linear trends of HCA in the overlapped area are $-6.84 \pm 5.27 \times 10^6$ J/m^2/month for the gridded KODC and $-1.83 \pm 2.07 \times 10^6$ J/m^2/month for NA12 data. For the smoothed KODC data, the amplitude of variation is reduced also with the reduced linear trend of $-4.11 \pm 3.16 \times 10^6$ J/m^2/month. This trend is still more than 2 times faster than that in the NA12 data because the spatial smoothing is only applied with KODC data inside the overlapped area. This comparison demonstrates the effects of spatial smoothing in the region affected by the western boundary current (EKWC) in NA12 data which can result in slower long-term trend of HCA as well as reduced amplitude of the OHC variations.

The HCA trend in the EJS shows slower warming in the upper 150 m and faster warming below 250 m as compared to that in the

global and Pacific ocean (Figure 3.2a). Hence, the faster warming rate in the upper 500 m in the EJS as compared to the global and Pacific ocean is mainly due to the fast warming of the subsurface water below 250 m. The faster warming of deep-water during 1996–2007 in the ES than the global warming rate was previously documented [e.g., Kim et al., 2008]. Percent variances accounted for by the linear trend in the upper 200 m in the EJS are also smaller than those in the global and Pacific ocean, while they are larger than those in the Pacific below 250 m and comparable to or larger than those in the global ocean below 350 m (Figure 3.2b).

Regional trends of the non-seasonal heat content in the EAST, WEST, and UB indicate the warming of the entire column in the upper 500 m in the EAST, and cooling between 75 m and 300 m in the WEST (Figure 3.2c), which results in the slower warming between 75 m and 300 m in the EJS (Figure 3.2a). In the UB, the cooling rate is peaked at the same depth level as in the WEST. However, the cooling rate in the UB is overall faster than that in the WEST. The cooling in the UB extends down to 500 m. Percent variances accounted for by linear trends as a function of depth indicate the higher contribution of the linear trends to the HCA in the EAST as compared to that in the WEST and in the UB whose percent variances are lower than 50% at any depth (Figure 3.2d).

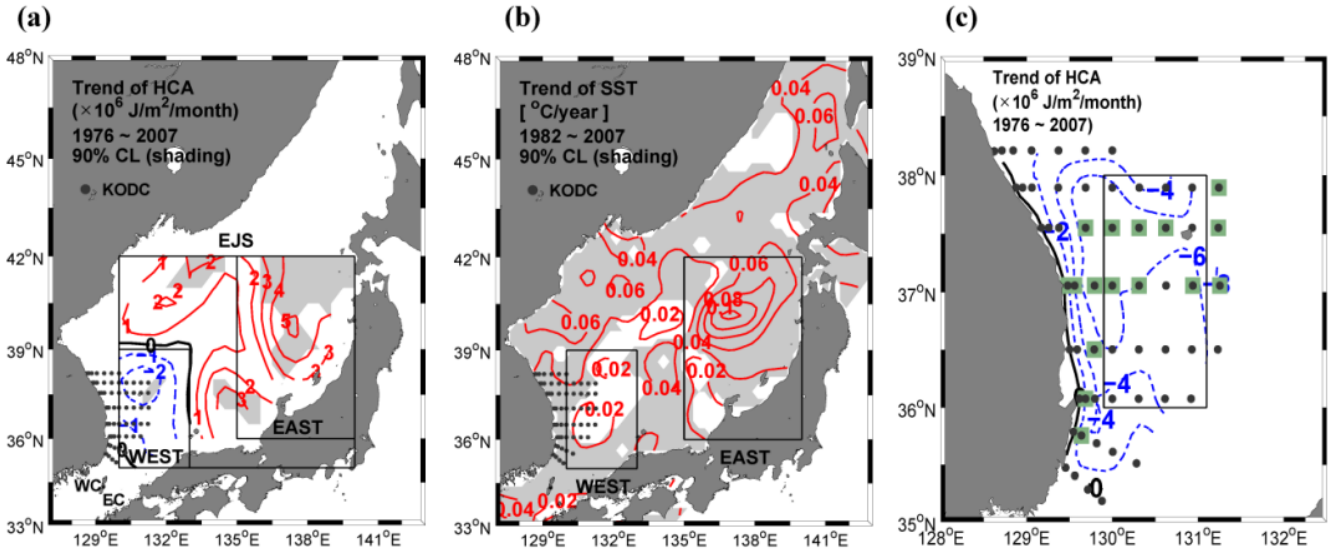

Figure 3.1. (a) Spatial pattern of long term (1976–2007) trends of non-seasonal heat content in the upper 500 m based on NA12 data [Na et al., 2012]. The shaded areas have significant trends at the 90% confidence level. The positive (negative) trend is shown by red solid (blue dashed) lines with zero value denoted by a black solid line. The contour interval is $\mathbf{1 \times 10^6\ J/m^2/month}$. The black-box regions EAST, WEST, and EJS correspond to 135–140°E and 36–42°N, 130–133°E and 35–39°N, and 130–140°E and 35–42°N, respectively. KODC stations are also shown by dots. WC (EC) denotes the western (eastern) channel of the Korea Strait. (b) The same as Figure 3.1a, but for the AVHRR sea surface temperature during 1982–2007. The contour interval is 0.02 ℃/year. (c) The same as Figure 3.1a, but for

the results in the region UB covered by KODC data. The contour interval is $\mathbf{2 \times 10^6\ J/m^2/month}$, the stations with a significant trend at 90 % confidence level are denoted by shaded squares. HCAs shown in Figure 3.3e are calculated in overlapped areas (black boxes) between the NA12 and KODC data.

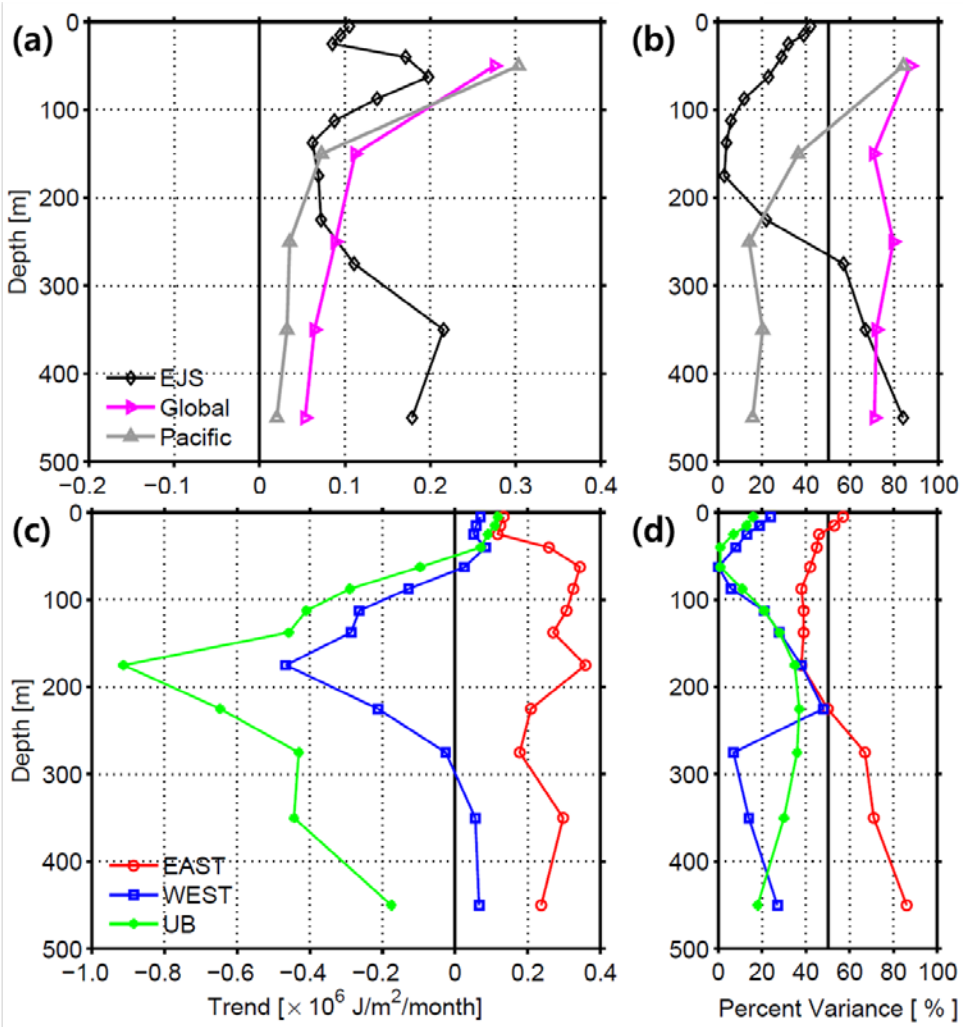

Figure 3.2. (a) Linear trends of non-seasonal heat content during 1976–2007 as a function of depth in the EJS (black diamond) together with those in the global ocean (magenta arrow) and Pacific Ocean (grey triangle) during 1955–2010 [from Figure 2 in Levitus et al., 2012]. (b) Percent variances accounted for by the linear trends as a function of depth in the EJS together with those for global and Pacific oceans [from Figure S3 in Levitus et al., 2012]. (c) The same as Figure 3.2a, but for the EAST (red), WEST (blue), and UB (green). (d) The same as Figure 3.2b, but for EAST (red), WEST (blue), and UB (green).

Table 3.1. Linear trends of non-seasonal heat content variation in the upper 500 m in the global ocean and Pacific Ocean during 1955–2010 [from Figure 2 in Levitus et al., 2012], and those in the whole area of NA12 data (EJS), southeastern ES (EAST), southwestern ES (WEST), and the region covered by the KODC data (UB) during 1976–2007 together with the 90% confidence level of the trend.

Region		Trend ($\times 10^6$ J/m^2/month)
Global ocean	(1955–2010)	0.61
Pacific ocean		0.50
EJS	(1976–2007)	1.13 ± 1.16
EAST		2.51 ± 2.29
WEST		-1.18 ± 1.27
UB		-4.75 ± 3.73

3.1.1.2. Interannual and decadal heat content variability

Time series of HCA are examined in the EJS and its sub-regions (EAST and WEST) to identify the similarity and difference in HCA other than linear trends using NA12 data first for data consistency (Figure 3.3a, 3.3b, 3.3c). Also, HCA time series in the UB together with that in the WEST (Figure 3.3d) are compared to look at the effects of spatial smoothing in the boundary current region in producing the HCA time series.

Decadal variation superimposed on an increasing trend characterizes the temporal variation of HCA in the EJS (Figure 3.3a) as documented by Na et al. [2012], and the warming trend in the EJS is mainly led by the warming in the EAST in spite of a slow cooling in the WEST (Figure 3.3b). HCA in the EAST shows negative anomalies before 1990, while positive anomalies persisted since then, resulting in a large increasing trend (Table 3.1). Similar to the HCA in the EAST, the HCA in the WEST is also characterized by quasi-decadal variability before 1995 with positive anomalies from 1976 to 1980 and from 1988 to 1994, and negative anomalies from 1981 to 1987 (Figure 3.3a). After 1995, the HCA in the WEST fluctuated between positive and negative anomalies on shorter timescales of 3–5 years, and total durations of negative anomalies (10 years) are longer than those of positive anomalies (3 years) resulting in the decreasing trend.

De-trended HCAs both in the EAST and WEST are dominated by decadal scale variation with periods of 10–12 years before 1995 (Figure 3.3c). The decadal variation became not so distinct from the mid-1990s, instead shorter-term variability replaced the decadal variation after 1995. Temporal variations of HCA in the EAST and WEST are poorly correlated with maximum correlation of 0.30

without removing the linear trend. On the other hand, de-trended time series of HCA between the EAST and WEST are correlated (r = 0.80) significantly at the 95% CL with HCA in the WEST leading that in the EAST by 21–22 months (Figure 3.3c).

The de-trended HCA in the EJS before 1995 is significantly correlated with those in the EAST and WEST with a maximum correlation of 0.94 with lags of 22–27 months (Figure 3.4a). This is consistent with the result of Minobe et al. (2004), who found that east-west phase difference of upper water temperature is about 2 years for the decadal first complex EOF mode. However, the maximum lagged correlation of the de-trended HCA in the EAST and WEST is reduced to 0.59 after 1995, which is not significant at the 95% CL. The lead-lag relationship between the HCAs in the EAST or WEST and the EJS before 1995 is such that the WEST leads EJS by 7 to 13 months with correlation of 0.94 (Figure 3.4b) and the EJS leads the EAST by 7 to 13 months with correlation of 0.97 (Figure 3.4c), which is almost consistent with lags of 22–27 months between the WEST and the EAST (Figure 3.4a).

The time series of HCA can be divided into in-phase and out-phase periods considering the sign of HCA in the WEST and EAST (Figure 3.3b). When HCA in the EAST has the same (opposite) sign with HCA in the WEST with longer than six months in a year, it is defined as the in-phase (out-phase) periods. During the out-phase (in-phase) periods, the amplitude of HCA in the EJS decreases (increases). The periods of 1976–1980, 1988–1989, and 1995–2007 correspond to the out-phase periods. Other periods such as 1981–1987 and 1990–1994 correspond to the in-phase periods. Hence, about two-thirds of the whole period corresponds to the out-phase periods. Although there were two short in-phase periods

(total 3 years) between 1995 and 2007 according to NA12 data (Figure 3.3b), this period is classified as the overall out-phase period considering a longer duration of the out-phase relationship (total 10 years). Moreover, the HCA in the UB remained negative for the time after 1995 (Figure 3.3d). Na et al. [2012] mainly addressed the in-phase variations of HCA in the ES and pointed out the importance of the depth variation of a 10 ℃ isotherm in causing those in-phase variations. Later, it is shown that the thickness variations of 10 ℃ isotherm are important during both the in-phase and out-phase periods, and those variations are associated with changes in the upper circulation.

The HCA derived from KODC data in the UB shows similar characteristics with that of NA12 data in the WEST (i.e., dominant quasi-decadal oscillations during 1976–1995), which has been suppressed since 1995 and interannual variations became more pronounced (Figure 3.3d). The interannual variation also existed in the UB prior to 1995, while it is not so obvious in the WEST. The HCA in the UB is well correlated with that in the WEST with a correlation of 0.83 at zero lag. After 1995, the HCA in the UB shows mostly negative anomalies, which contributes to an overall decreasing trend, the same as that in the WEST but with about three times faster than that in the WEST (Table 3.1). Hence, the HCA in the UB is characterized by a faster cooling trend and the larger amplitude of temporal variations as compared to those in the WEST. As mentioned earlier, this difference mainly arises from the spatial smoothing employed in NA12 data.

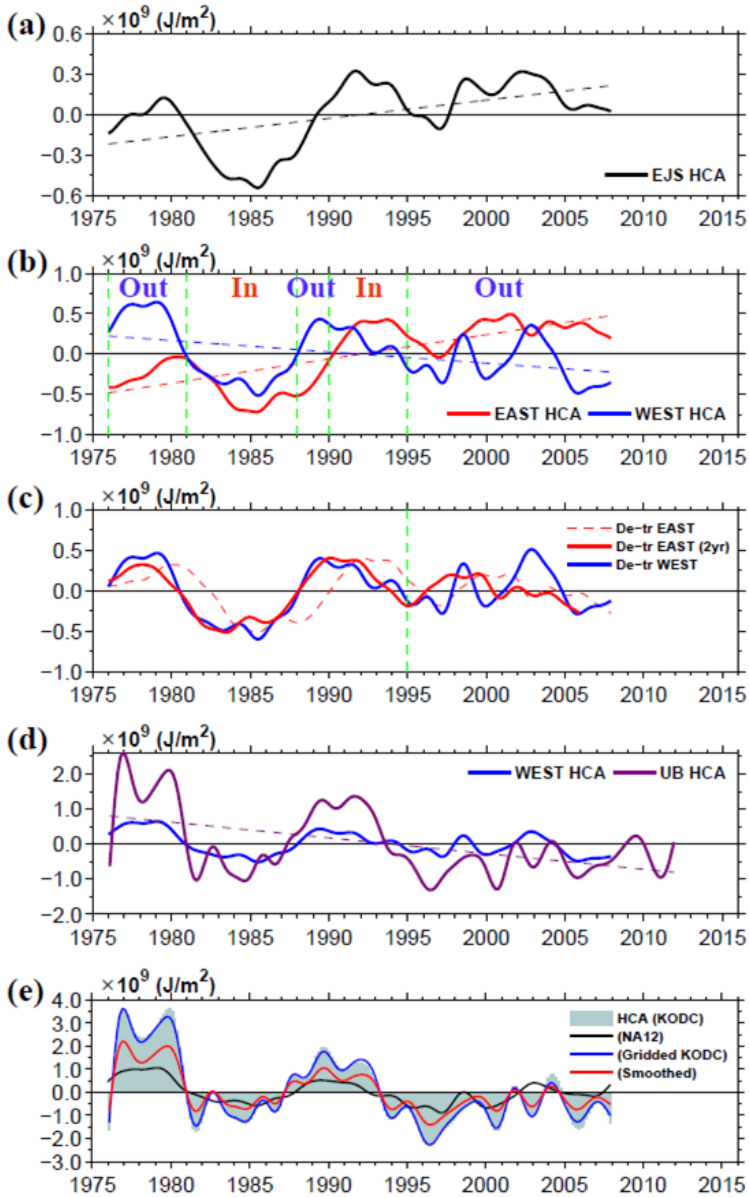

Figure 3.3. (a) Time series of HCA in the EJS during 1976–2007. The linear trend of HCA in the EJS is shown by a black dashed line. (b) Time series of HCA during 1976–2007 in the EAST (red) and WEST (blue) with their respective linear trends. Vertical green dashed lines indicate years for dividing the time series of HCA in the EAST and WEST into in- and out-phase periods. (c) De-trended time series of HCA in the EJS (dashed line), EAST (red line), and

WEST (blue line). For HCA in the EAST, the two-year advanced time series is shown. (d) Time series of HCA in the UB based on KODC data from 1976 to 2011 (purple) with HCA in the WEST based on NA12 data (blue). The linear trend of HCA in the UB is shown by a dashed line. (e) Time series of HCA using original KODC data (grey shade), gridded KODC data (blue line), gridded and smoothed KODC data by the Gaussian filter (red line), and NA12 data in an overlapped area between KODC and NA12 datasets enclosed by black box in Figure 3.1c (black line).

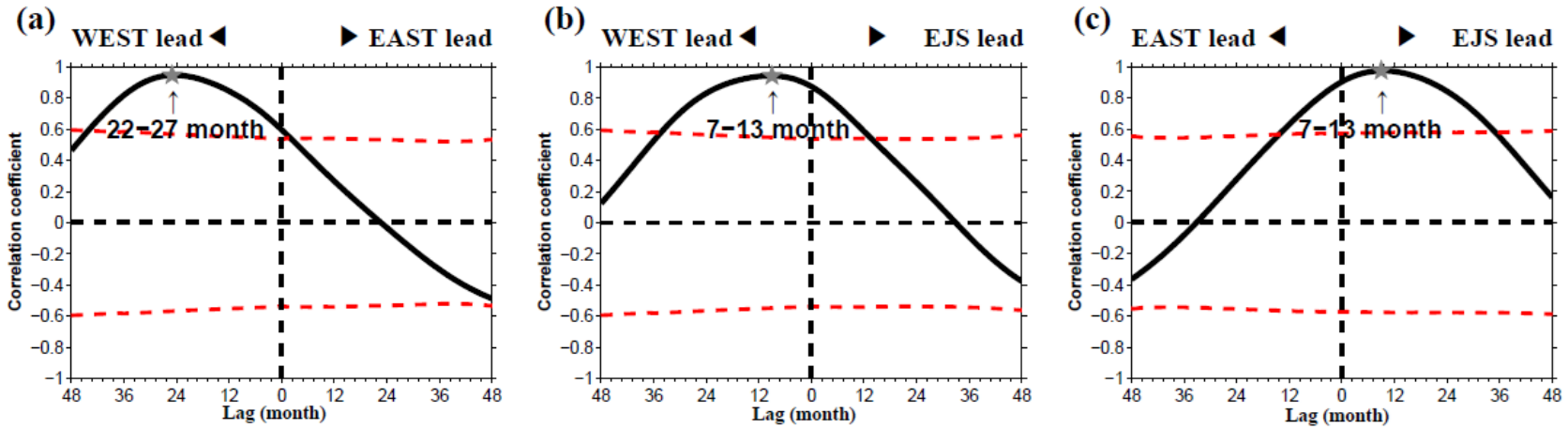

Figure 3.4. Lead-lag correlations (a) between HCA in the WEST and EAST during 1976–1994 (WEST leading), (b) HCA in the WEST and EJS (WEST leading), and (c) HCA in the EAST and EJS (EJS leading). All time series are detrended, and the maximum lead-lag correlations are indicated (star) with corresponding lags. The range of months indicates the same correlation values for those lags when the correlation is rounded off to 2 decimal digits. Red dashed lines represent the 95% confidence level. Degrees of freedoms, hence the 95% confidence levels are different depending on the lag.

3.1.2. Decomposition of HCA

As introduced in Section 2.2.1, HCA is decomposed into HCAs of four temperature ranges (R_1, R_2, R_3, and R_4) in order to investigate the contribution of different water masses to the HCA in the upper 500 m. The HCA of each temperature range is further decomposed into the heaving and warming parts, which results in a total of eight terms that control the HCA in the upper 500 m. The heaving parts ($\overline{T}H'_i$) contribute to an increase in HCA when the thickness (H_i) becomes larger than the long-term monthly mean values (positive H'_i). The warming parts ($\overline{H}T'_i$) also contribute to an increase in HCA when temperature (T_i) is higher than the long-term monthly mean temperature (positive T'_i).

The percent variance accounted for by the heaving and warming parts of each temperature range is shown in Table 3.2 together with the linear trend of each of the eight terms. The time series of HCA and heaving parts in the EAST and UB are shown in Figure 3.5. The heaving effect ($\overline{T}H'$) accounts for more than 90% of the HCA in the EAST and WEST.

Among the $\overline{T}H'_i$ parts of different temperature ranges, the thickness variation of the TWW layer warmer than 10 ℃ ($\overline{T}H'_1$) accounts for larger than 62% of the HCA in both the EAST and WEST (Table 3.2). Moreover, temporal variations of $\overline{T}H'_1$ in both the EAST and WEST are highly correlated with the HCA in both regions, indicating that the deepening and shoaling of a 10 ℃ isotherm is the major contributor to the HCA in the upper 500 m both in the southeastern and southwestern ES. Na et al. [2012] also suggested that the decadal upper ocean heat content variability in the ES is related to the variability of 10 ℃ isotherm depths

reflecting the variability of the TWC. The deepening or shoaling of the 10 ℃ isotherm ($\overline{T}H'_1$) is also a key factor for the HCA in the UB with the largest variance (~ 65%) and the highest correlation (> 0.88) with the HCA (Table 3.2 and Figure 3.5b).

However, the secondary contributors are different. In the EAST, time series of the integrated heaving effect of the layer enclosed by the 10 ℃ isotherm and 500 m ($\sum_{i=2}^{4} \overline{T}H'_i$) (dotted line in Figure 3.5a) is concomitant with the ESIW heaving ($\overline{T}H'_3$) (blue line in Figure 3.5a), indicating that $\overline{T}H'_3$ has the secondary importance. The temporal variation of the ESIW heaving accounts for 23% of the HCA in the EAST, and is significantly correlated with HCA in the EAST (r = 0.69) in a positive sense, which means that the thickening of the ESIW layer contributes to an increase in HCA (Table 3.2, Figure 3.5a). The long-term warming trend of the HCA in the EAST is also mainly due to the thickening of both $\overline{T}H'_1$ and $\overline{T}H'_3$ (Table 3.2). This occurs because the thickening of the ESIW layer accompanies the thinning of the JSPW layer below the ESIW layer down to 500 m, which is obvious from Table 3.2 in that $\overline{T}H'_4$ has a negative correlation with HCA and also a negative trend. On the other hand, the thickness variation of the thermocline layer ($\overline{T}H'_2$) rather than $\overline{T}H'_3$ has a secondary importance in determining the total HCA in the UB (Figure 3.5b) with a percent variance and a correlation with total HCA of 27% and 0.69, respectively. $\overline{T}H'_2$ also has a secondary importance in the WEST but with reduced percent variance (19%) and correlation (0.44) (Table 3.2).

Contribution of $\overline{T}H'_3$ in the WEST to HCA is relatively large (10.8%) as compared to that in the UB (3.9%). $\overline{T}H'_3$ in the WEST is also significantly correlated with HCA (r = −0.61) as compared to virtually no correlation of $\overline{T}H'_3$ with HCA in the UB. This implies

that the thickness variation of the ESIW (thermocline) layer becomes progressively less (more) important from the EAST to the WEST and from the WEST to the UB in determining the HCA in the upper 500 m. There has been a significant thickness variation of the ESIW layer in the EAST during the study period (Figure 3.5a), while the thickness of the ESIW has remained relatively stable in the WEST and UB (not shown). This is also reflected in the linear trends of $\overline{\mathrm{TH}}'_3$ in the EAST and UB (Table 3.2). There is virtually no trend of $\overline{\mathrm{TH}}'_3$ in the UB, while a significant positive trend of $\overline{\mathrm{TH}}'_3$ exists in the EAST. Both $\overline{\mathrm{TH}}'_1$ and $\overline{\mathrm{TH}}'_2$ showed predominantly negative anomalies starting from 1995, while $\overline{\mathrm{TH}}'_1$ experienced a decadal variation and $\overline{\mathrm{TH}}'_2$ remained mainly positive before 1995 (Figure 3.5b). Hence, both $\overline{\mathrm{TH}}'_1$ and $\overline{\mathrm{TH}}'_2$ have decreasing trends for the entire period (Table 3.2), which then contributes to the strong and statistically significant cooling trend of HCA in the UB for the entire period (Table 3.1). Although the $\overline{\mathrm{TH}}'_1$ trend in the UB is faster than that in the EAST, it is not significant at the 95% CL while the $\overline{\mathrm{TH}}'_1$ trend in the EAST is significant (Table 3.2), implying the OHC variability in the UB is mainly dominated by temporal fluctuations rather than trend, consistent with the percent variance of the trend in those regions (Figure 3.2d, Figure 3.3d).

Overall, the percent variances accounted for by the warming effect in the EAST and WEST are less than 3.2% (Table 3.2). The linear trends of the warming component for the ESIW layer ($\overline{\mathrm{HT}}'_3$) and the JSPW layer ($\overline{\mathrm{HT}}'_4$) have opposite trends of cooling of the ESIW layer and warming of the JSPW layer in both the EAST and WEST. The cooling of the ESIW layer is the fastest in the UB and the warming of the JSPW layer is the fastest in the EAST. The warming of the JSPW layer appears to be associated with a shift of

the ES ventilation system [Kang et al., 2003; Gamo et al., 2014]. The long-term cooling trend of the ESIW layer has been little documented and may be also related to changes in the ventilation system. It is noteworthy that the ESIW layer has experienced the fastest thickening trend in the EAST. However, the thickening trend slows down towards the west and shows a thinning trend in the UB (Table 3.2).

Table 3.2. Percent variance of each decomposed part of total eight components of HCA to HCA, cross correlation coefficients between each decomposed part and HCA, and the linear trend of each decomposed part (Trend) in the four regions defined in the text with 90% confidence level of the trend. $\overline{\mathbf{T}}\mathbf{H}_\mathbf{i}'$ denotes the i-th heaving component and $\overline{\mathbf{H}}\mathbf{T}_\mathbf{i}'$ the i-th warming component.

EAST	Water Mass	Temperature range (℃)	Part	Variance (%)	r	Trend ($\times 10^6$ J/m^2/month)
	TWW	$10 < T$	$\overline{\mathrm{T}}\mathrm{H}'_1$	62.6	0.95	1.41 ± 1.14
			$\overline{\mathrm{H}}\mathrm{T}'_1$	2.1	0.62	0.27 ± 0.25
	Thermocline layer	$5 < T < 10$	$\overline{\mathrm{T}}\mathrm{H}'_2$	2.1	0.09	-0.06 ± 0.16
			$\overline{\mathrm{H}}\mathrm{T}'_2$	0.9	0.96	0.20 ± 0.19
	ESIW	$1 < T < 5$	$\overline{\mathrm{T}}\mathrm{H}'_3$	23.3	0.69	1.19 ± 1.04
			$\overline{\mathrm{H}}\mathrm{T}'_3$	2.3	−0.67	-0.38 ± 0.32
	JSPW	$1 > T$	$\overline{\mathrm{T}}\mathrm{H}'_4$	4.5	−0.84	-0.52 ± 0.46
			$\overline{\mathrm{H}}\mathrm{T}'_4$	2.2	0.75	0.40 ± 0.30

WEST	Water Mass	Temperature range (℃)	Part	Variance (%)	r	Trend ($\times 10^6$ J/m^2/month)
	TWW	$10 < T$	$\overline{\mathrm{T}}\mathrm{H}'_1$	65.0	0.96	-0.71 ± 1.24
			$\overline{\mathrm{H}}\mathrm{T}'_1$	3.2	0.21	0.38 ± 0.40
	Thermocline layer	$5 < T < 10$	$\overline{\mathrm{T}}\mathrm{H}'_2$	19	0.44	-1.14 ± 0.98
			$\overline{\mathrm{H}}\mathrm{T}'_2$	0.3	0.87	-0.04 ± 0.08

	ESIW	$1 < T < 5$	$\overline{\mathrm{T}}\mathrm{H}'_3$	10.8	−0.61	0.36 ± 0.49
			$\overline{\mathrm{H}}\mathrm{T}'_3$	0.9	0.03	-0.15 ± 0.20
	JSPW	$1 > T$	$\overline{\mathrm{T}}\mathrm{H}'_4$	0.5	−0.01	-0.01 ± 0.11
			$\overline{\mathrm{H}}\mathrm{T}'_4$	0.3	−0.08	0.13 ± 0.14

UB	Water Mass	Temperature range (℃)	Part	Variance (%)	r	Trend ($\times 10^6$ J/m^2/month)
	TWW	$10 < T$	$\overline{\mathrm{T}}\mathrm{H}'_1$	65.1	0.88	-2.14 ± 2.51
			$\overline{\mathrm{H}}\mathrm{T}'_1$	1.9	−0.12	0.62 ± 0.25
	Thermocline layer	$5 < T < 10$	$\overline{\mathrm{T}}\mathrm{H}'_2$	27.9	0.71	-2.81 ± 2.73
			$\overline{\mathrm{H}}\mathrm{T}'_2$	0.1	0.71	-0.08 ± 0.11
	ESIW	$1 < T < 5$	$\overline{\mathrm{T}}\mathrm{H}'_3$	3.9	0.01	-0.18 ± 0.65
			$\overline{\mathrm{H}}\mathrm{T}'_3$	0.6	0.73	-0.43 ± 0.40
	JSPW	$1 > T$	$\overline{\mathrm{T}}\mathrm{H}'_4$	0.4	−0.76	0.24 ± 0.23
			$\overline{\mathrm{H}}\mathrm{T}'_4$	0.1	0.31	0.04 ± 0.11

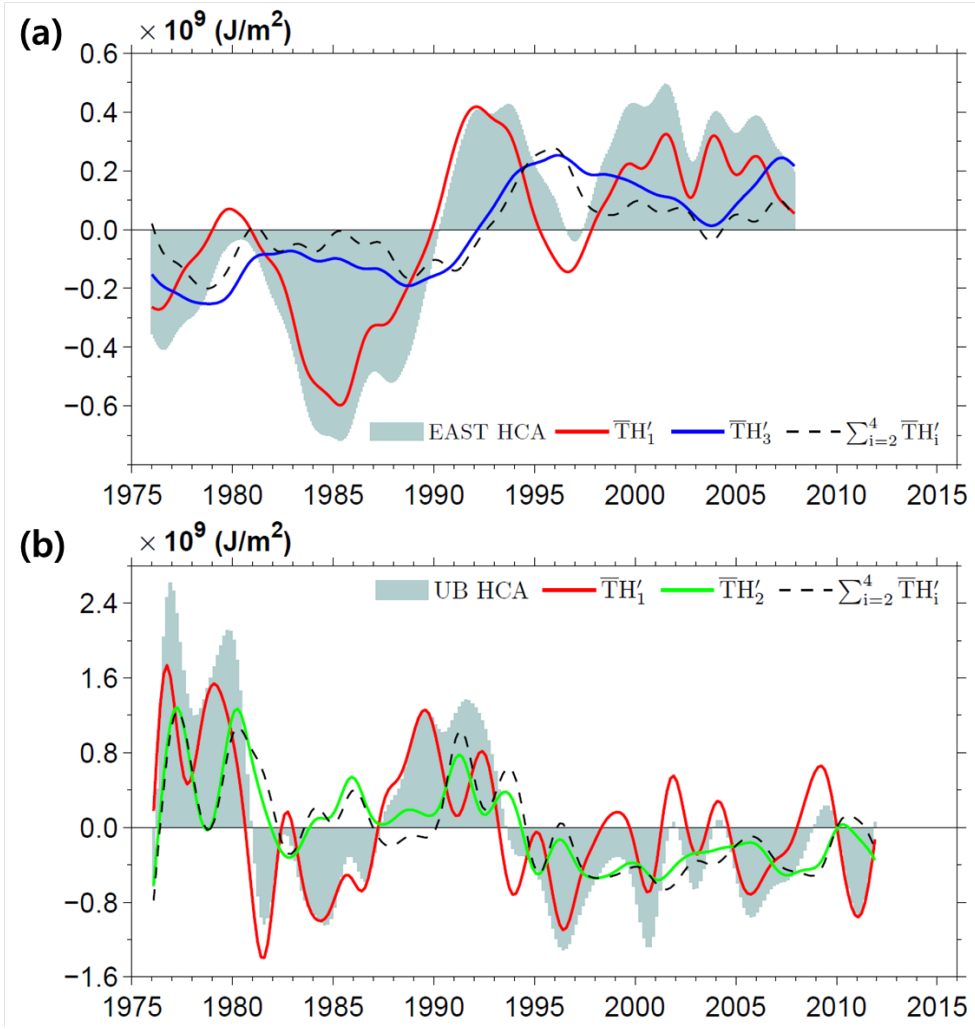

Figure 3.5. (a) Time series of HCA (shading), $\overline{\mathbf{TH}}'_{\mathbf{1}}$ (red), $\overline{\mathbf{TH}}'_{\mathbf{3}}$ (blue), and $\sum_{\mathbf{i=2}}^{\mathbf{4}} \overline{\mathbf{TH}}'_{\mathbf{i}}$ (black dashed) in the EAST (b) Time series of HCA (shading), $\overline{\mathbf{TH}}'_{\mathbf{1}}$ (red), $\overline{\mathbf{TH}}'_{\mathbf{2}}$ (green), and $\sum_{\mathbf{i=2}}^{\mathbf{4}} \overline{\mathbf{TH}}'_{\mathbf{i}}$ (black dashed) in the UB.

3.1.3. HCA and depth variation of 10 ℃ isotherm

Through the decomposition analysis, the heaving effect, especially the deepening or shoaling of the TWW layer warmer than 10 ℃ (H_1'), is shown to be a dominant component of the HCA in both EAST and WEST (also UB). However, linear trends of $\overline{T}H'_1$ in the EAST and WEST (UB) have an opposite sign of warming in the EAST and cooling in the WEST (UB). De-trended $\overline{T}H'_1$ in the EAST is shown to be significantly correlated with that in the WEST before 1995 (r = 0.95 at lags of 22–27 months), while all calculated correlations decreased below 90% CL after 1995. This implies two things, 1) the OHC variations south of the subpolar front in the ES are mainly determined by fluctuations of the 10 ℃ isotherm, and 2) the fluctuations of 10 ℃ isotherm depth in the EAST and in the WEST are determined by different mechanisms after 1995.

Horizontal distributions of the 10 ℃ isotherm anomaly in the EJS and the UB are shown in Figure 3.6 based on NA12 data and Figure 3.7 based on KODC data together with the mean 10 ℃ isotherm depths over the whole period. Although the depth anomalies in the UB (Figure 3.7) are about twice as large as those in the WEST (Figure 3.6) even in the overlapped area between the WEST and UB, the spatial pattern of anomalies seen in the UB is well captured in the WEST.

The 10 ℃ isotherm depth anomalies in the EJS show the same sign in a wide area when they are averaged over in-phase periods (Figure 3.6b and 3.6c). From 1981 to 1987, negative anomalies of a 10 ℃ isotherm depth are prevalent all over the EJS (Figure 3.6b), indicating shoaling of a 10 ℃ isotherm depth both in the EAST and WEST, which then resulted in the negative HCA anomalies (Figure

3.3a and 3.3b). During this period, negative anomalies of a 10 ℃ isotherm depth are also dominant in the UB (Figure 3.7b). The opposite case occurred during 1990–1994 (Figure 3.6c). The positive anomalies prevail extending south of 37.5°N in the WEST to northeast in the whole EAST, except for weak negative anomalies north of 37.5°N in the WEST. In the UB, positive anomalies are also predominant especially near the coastal region west of 130°E (Figure 3.7c). Negative anomalies extending in the northeast-southwest direction east of 130°E and north 36.5°N also correspond to the negative anomalies seen in the WEST (Figure 3.6c).

Large positive anomalies confined in the WEST (UB) and large negative anomalies off the northwestern coast of Japan characterized the out-phase period during 1976–1980 (Figure 3.6d, 3.7d). The anomaly map during 1995–2007 shows dominant negative anomalies mainly in the WEST, and mostly positive anomalies in other parts of the EJS (Figure 3.6e). Negative anomalies also occur in a wide area in the UB during the same period (Figure 3.7e). The anomalies in Figure 3.6e and 3.7e are weaker than the anomalies in other periods because of the long-period of averaging and dominant interannual variations during 1995–2007 (Figure 3.3b, 3.3d). Note also that the secondary contributors became more important in HCAs in both EAST and UB after 1995 (not shown), and the 10 ℃ isotherm has lesser contribution to HCA in both regions after 1995.

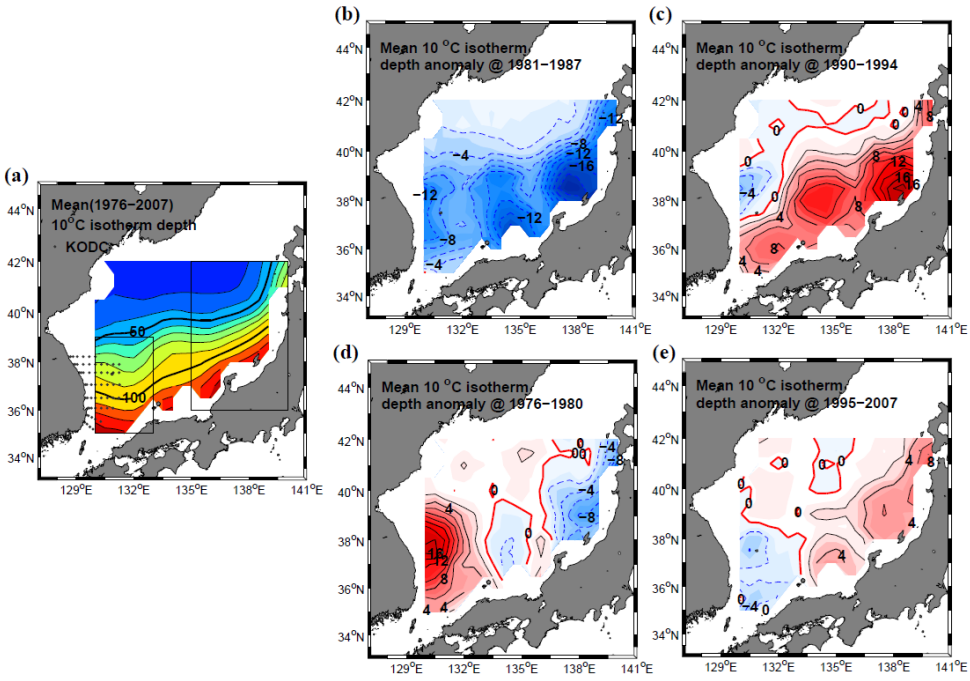

Figure 3.6. (a) Spatial pattern of long-term (1976–2007) averaged 10 ℃ isotherm depth in the EJS. Contour interval is 10 m. Black boxes indicate the WEST and EAST regions. (b)–(c) Horizontal distributions of 10 ℃ isotherm depth anomaly averaged over in-phase periods, 1981–1987 and 1990–1994. (d)–(e) Horizontal distributions of 10 ℃ isotherm depth anomaly averaged over the out-phase periods, 1976–1980 and 1995–2007. Contour interval is 2 m. The positive (negative) values are shown with black solid (blue dashed) lines and the zero value is denoted by red solid lines.

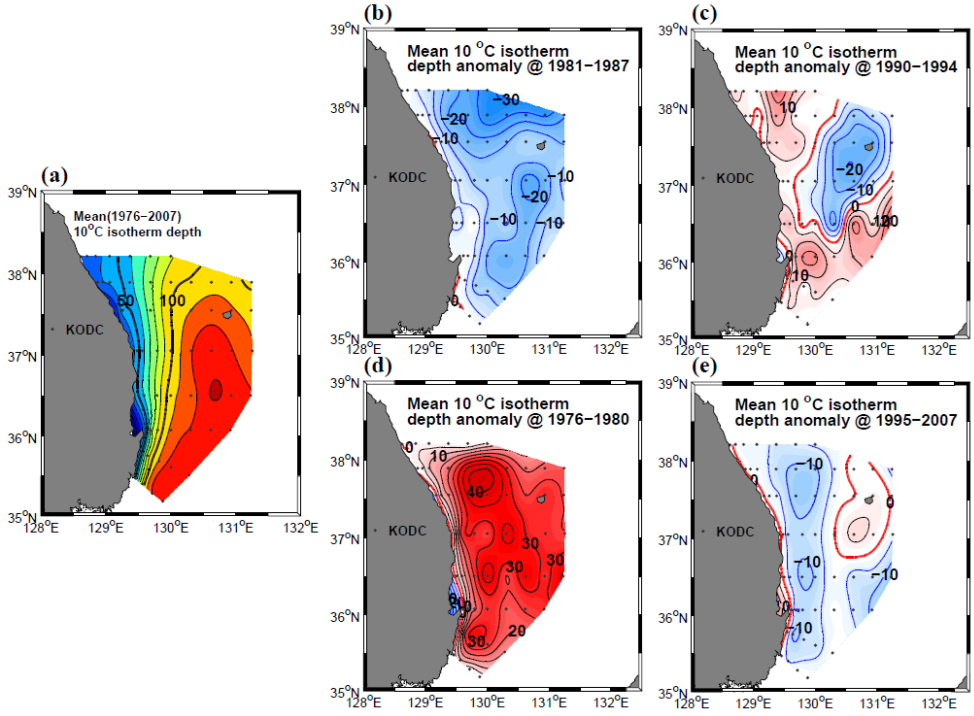

Figure 3.7. (a) The same as Figure 3.6a, but in the UB. (b)–(e) The same as Figure 3.6b–e, but in the UB. Contour interval is 5 m.

3.1.4. HCA and upper circulation

The spatial pattern of 10 ℃ isotherm has been documented to reflect the upper circulation in the ES [Gordon et al, 2002; Na et al., 2012]. Spatial distributions of the mean depth of 10 ℃ isotherm and average dynamic height at surface relative to 500 m based on NA12 data, and mean SSH during the period of 1976–2007 clearly demonstrate that the 10 ℃ isotherm depth well represents the upper circulation in the ES (Figure 3.8). The mean 10 ℃ isotherm depths are deepest in the southern and southeastern parts and decrease towards the northwest, which is natural in that the separated EKWC and ONB generally flow to east or northeast with deeper subsurface isotherms in the upper layer towards the southeast in a sense of geostrophy. The gradient of a 10 ℃ isotherm depth becomes steeper towards the northeast where the EKWC and the ONB merge and exit to the North Pacific through the Tsugaru Strait. Wave like features west of 134°E are due to the meandering of the EKWC after separating from the east coast of Korea. The EKWC hugging the east coast of Korea is not so well represented in NA12 data but it is well reflected by the steep gradient of the 10 ℃ isotherm depth and dynamic height near the east coast of Korea in the KODC data (Figure 3.7, 3.9d, 3.9e, and 3.9f).

Shown in Figure 3.9 are annual mean dynamic height fields for three years, 1977 when HCA in the EAST is negative and HCA in the WEST (UB) is positive, 1984 when HCA is negative both in the EAST and WEST (UB), and 1991 when HCA is positive both in the EAST and WEST (UB) (see Figure 3.3b and 3.3d). Higher dynamic heights with larger horizontal gradients, and farther northward

displacements of contour lines (e.g., 0.6 m isolines) are obvious when HCA in the WEST (UB) is positive in 1977 and 1991 (Figure 3.9a, 3.9c, 3.9d, and 3.9f) as compared to the dynamic height field in 1984 when HCA in the WEST (UB) shows negative anomaly (Figure 3.9b and 3.9e). This clearly shows that positive HCA in the WEST (UB) is associated with the stronger EKWC and farther northward penetration of the EKWC. This is also the case in the EAST. When HCA in the EAST is positive in 1991, dynamic heights are higher and the 0.6 m contour line is placed farther northwestward in the EAST as compared to the cases when HCA in the EAST shows negative anomalies in 1977 and 1984 (Figure 3.9a, 3.9b, and 3.9c). This indicates that positive HCA is related to the stronger and broader ONB.

Time series of section-averaged surface geostrophic velocities relative to the maximum depth of available data perpendicular to two sections in the EAST (see Figure 3.9a) and in the UB (see Figure 3.9d) are shown in Figure 3.10b and 3.10d together with time series of the TWW heaving ($\overline{TH}'_1$) in the EAST and UB. Surface geostrophic velocities computed from dynamic heights relative to 500 m and satellite altimetry-derived geostrophic velocities across those two sections during the period of 1993–2007 are well correlated with correlations higher than 0.75 (significant at the 95% CL) (Figure 3.10a and 3.10c). RMS differences between them in the UB and EAST are 4.7 cm/s and 0.93 cm/s, respectively, which might arise from the affection of southward and southwestward velocity in the lower layer. And NA12 data are spatially smoothed so RMS difference in the EAST is much smaller than that in the UB. The calculated geostrophic currents across the two sections reflect the intensity and poleward

extent of the EKWC in the UB and ONB in the EAST. Both time series in the EAST and UB between the TWW heaving and geostrophic currents are positively correlated with correlations higher than 0.60 (significant at the 95% CL), indicating that the deepening or shoaling of 10℃ isotherm depth in both regions, which is a major contributor for the OHC variations, are determined by the upper circulation, the EKWC in the UB and the ONB in the EAST. During 2003−2006, geostrophic currents showed weak positive values though the TWW heaving in the EAST was large positive. It is noted that the OB might develop in the northern part of this section during this period so northeastward velocity along the section from 2003 to 2006 would not detect the development of the ONB well. In the UB, northward geostrophic currents were fairly strong (~20 cm/s) also during 2003–2006 when the TWW heaving was positive but very small. These events need to be further investigated.

With the evidence of the TWW heaving, hence the OHC variations, related to the upper circulation mentioned in the above, the in-phase heat content variations in the eastern and western ES can be explained. During the period 1981–1987, negative anomalies of 10℃ isotherm depth occur in a wide area (Figure 3.6b and 3.7b) with negative HCA (Figure 3.3b and 3.3d). The upper circulation in this period is characterized by a poor development of the EKWC and the ONB (Figure 3.9b and 3.9e) resulting in weak geostrophic velocities across two sections in the UB and EAST (Figure 3.10b and 3.10d). When positive anomalies of 10 ℃ isotherm depth occur in a wide area (Figure 3.6c and 3.7c) also with positive HCA (Figure 3.3b and 3.3d) during 1990–1994, both the EKWC and ONB well develop (Figure 3.9c and 3.9f) with strong geostrophic

velocities across two sections in the UB and EAST (Figure 3.10b and 3.10d).

The east-west contrast of anomalies of the 10 ℃ isotherm depth (Figure 3.6d, 3.6e, Figure 3.7d and 3.7e) is also associated with the upper circulation. During the warm WEST (UB) and cold EAST period (Figure 3.6d and 3.7d), the EKWC well develops in the WEST (UB) reaching far to the north carrying its warm water with a deeper 10 ℃ isotherm (Figure 3.9a, 3.9d, Figure 3.10b and 3.10d), while the development of the ONB is restricted (Figure 3.9a and 3.10b). For the opposite case, warm EAST and cold WEST (UB) period (Figure 3.6e and 3.7e), the ONB well develops and transports warm water in a thick layer of the EAST (Figure 3.10b), while the EKWC poorly develops in the UB (Figure 3.10d).

Spatial distributions of correlation between non-seasonal SST variations and the TWW heaving provide further evidence of the importance of the upper circulation in the variation of the TWW heaving in the EAST and WEST (UB). The TWW heaving in the WEST is significantly correlated with the non-seasonal SST variation in a small part of the WEST but in a wider area north of the WEST between 38–41°N and west of 135°E (Figure 3.11a and Figure A2a). The areas with significant positive correlations exactly coincide with climatological SST frontal positions, western part of the subpolar front and its two western branches (see Figure 1 of Park et al., 2004). The positive correlation extends farther to the east along the subpolar front. A similar pattern is yielded in the correlation map between non-seasonal SST variation and TWW heaving in the UB (Figure 3.11b and Figure A2b) but now the area with significant positive correlations emerges along the east coast of Korea with broader area of correlation higher than 0.5. The

correlation maps indicate that when the EKWC with a thick layer warmer than 10 ℃ develops along the east coast of Korea and penetrates far to the north, it acts to not only increase HCA in the UB but also increase SST along the east coast of Korea and along the subpolar front of the ES.

When $\overline{TH'}_1$ in the EAST is large, overall SST warming occurs in a wide area of the ES north of 39°N (Figure 3.11c). However, the significant correlations (95% CL) with the SST variation mainly occur in the northeastern part of the ES including the northern half of the EAST. The relationship between $\overline{TH'}_1$ in the EAST and SST (Figure 3.11c) indicates that the increase of the HCA in the EAST by the thickening of the TWW layer due to the ONB results in the SST warming in the downstream region of the TWC, even north of the Tsugaru Strait, which is the main exit of the TWC to the North Pacific. This result is consistent with that of Onishi and Ohtani [1997] who show that the volume transport of the TWC south of the Tsugaru Strait is well correlated with that north of the Tsugaru Strait while the volume transport through the Tsugaru Strait has near steady transport. The result also suggests that the Tsugaru Warm Current and the Soya Warm Current carry warmer surface waters towards the North Pacific and Sea of Okhotsk when the HCA is large in the EAST.

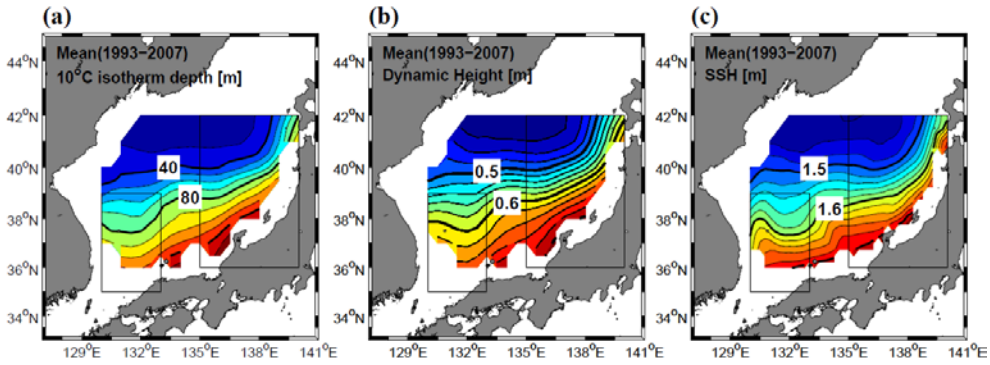

Figure 3.8. (a) Mean depth of the 10 ℃ isotherm during 1976–2007 for stations deeper than 500 m based on NA12 data. Black boxes indicate the WEST and EAST regions. The contour interval of black bold (thin) line is 40 (10) m. (b) The same as Figure 3.8a, but for the mean dynamic height (geopotential height anomaly at surface relative to 500 m divided by the acceleration of gravity in meters). The contour interval of black bold (thin) line is 0.1 (0.2) m. (c) The same as Figure 3.8a, but for the satellite-altimetry derived (AVISO) mean sea surface height (SSH). The contour interval of black bold (thin) line is 0.1 (0.2) m.

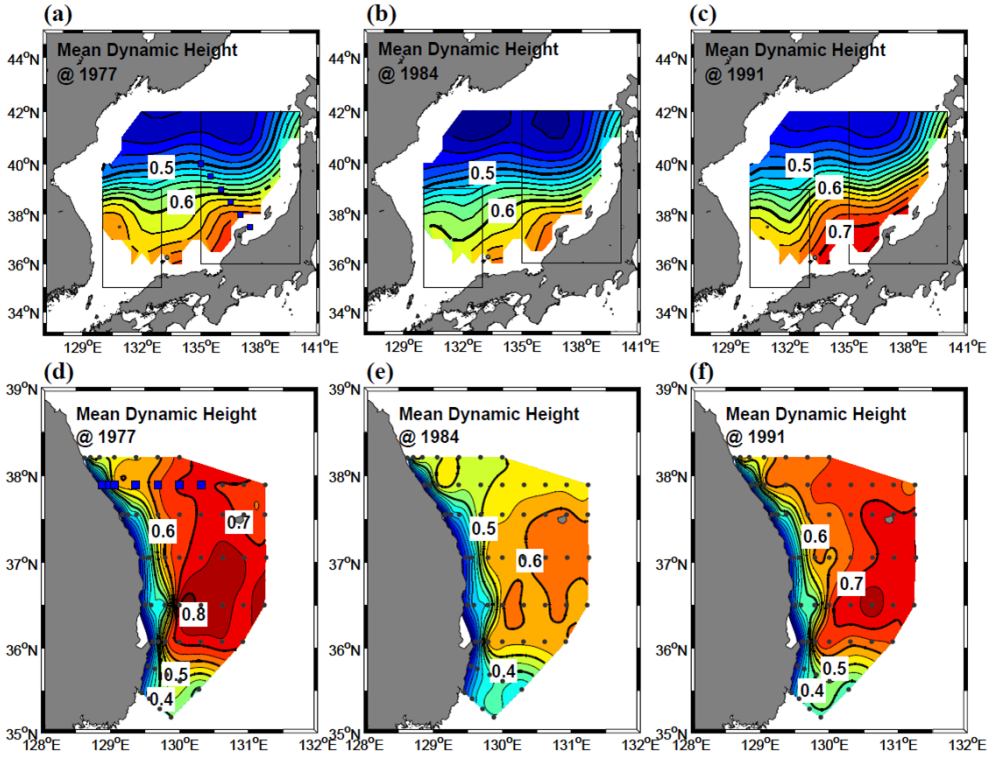

Figure 3.9. Spatial patterns of mean dynamic height (a, b, c) in the EJS based on NA12 data and (d, e, f) in the UB based on KODC data. (a), (d) in 1977, (b), (e) in 1984, and (c), (f) in 1991. Arrays of squares in (a) and (d) denote two sections where surface geostrophic currents are calculated using sea surface height data shown in Figure 3.10b and 3.10d.

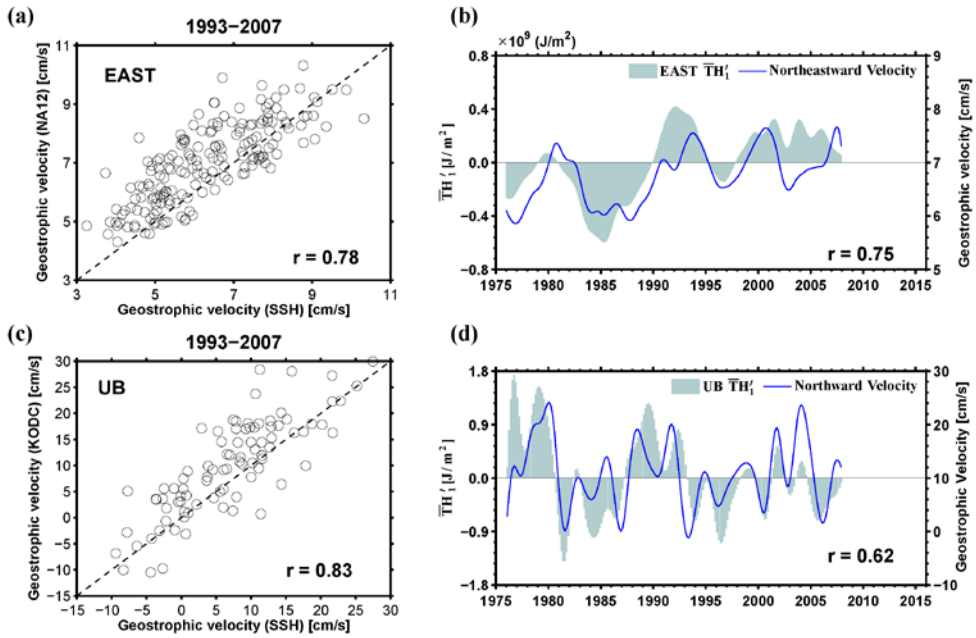

Figure 3.10. (a) Relation between section-averaged monthly surface geostrophic velocity relative to 500 m based on NA12 data and surface geostrophic velocity calculated from monthly mean AVISO SSH data along the section in the EAST shown in Figure 3.9a. Numbers on the bottom right denote correlation coefficients, which are both significant at the 95% confidence level. (b) Time series of $\overline{TH}'_1$ in the EAST (grey bar) and section-averaged northeastward geostrophic velocity (blue line) along the line shown in Figure 3.9a. The correlation coefficient is shown on the bottom right, which is significant at the 95% confidence level. (c) The same as Figure 3.10a, but for the relation between bimonthly surface geostrophic velocity calculated using KODC data and surface geostrophic velocity obtained using bimonthly-averaged SSH field along the section shown in Figure 3.9d. (d) The same as Figure 3.10b, but for the time series of $\overline{TH}'_1$ in the UB (grey bar) and northward geostrophic velocity (blue line) along the line shown in Figure 3.9d.

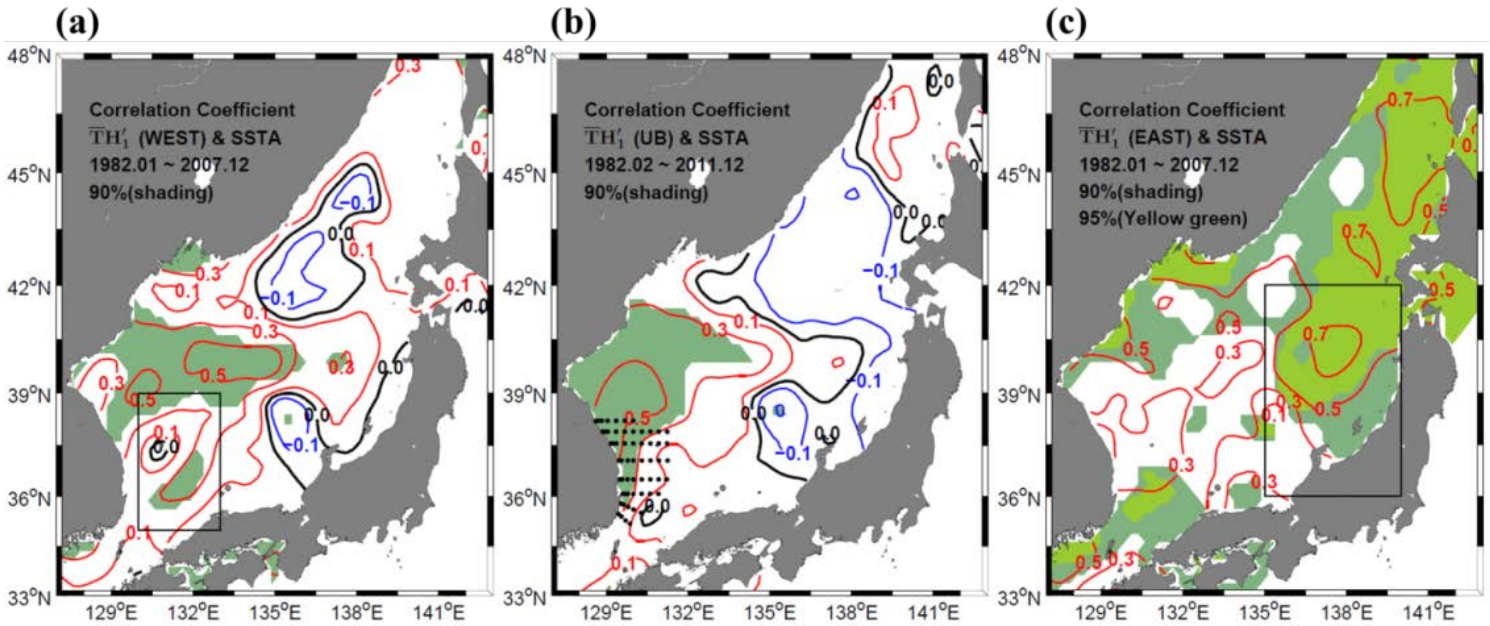

Figure 3.11. Spatial correlation map (a) between non-seasonal SST variation and $\overline{TH}'_1$ variation in the WEST (1982–2007), (b) between non-seasonal SST variation and $\overline{TH}'_1$ in the UB (1982–2011), and (c) between non-seasonal SST variation and $\overline{TH}'_1$ in the EAST (1982–2007). The non-seasonal SST is calculated by subtracting the monthly mean climatology. The shaded areas have a significant correlation coefficient at the 90% confidence level. Areas having a significant correlation coefficient at the 95% confidence level is also shown in (c) with yellow green color.

3.1.5. Causative mechanisms for HCA variations

The OHC variations in the upper 500 m in the southeastern and southwestern ES are shown to be mainly determined by the heaving of the TWW layer ($\overline{TH}'_1$), which is then associated with the upper circulation of the ES. I discuss possible mechanisms for the $\overline{TH}'_1$ variations in two sub-regions of the ES by investigating atmospheric and oceanic factors through lagged correlation analysis (Table 3.3, Figure 3.12). Time series of $\overline{TH}'_1$ in the UB is used instead of that in the WEST to represent the southwestern parts of the ES because the time series of $\overline{TH}'_1$ in the UB reflects the variation of the EKWC better than $\overline{TH}'_1$ in the WEST. The correlation between $\overline{TH}'_1$ in the UB and that in the WEST is 0.77 at zero lag and significant at the 95% CL. The correlation analysis is also carried out in two different periods (i.e., before and after 1995) because the characteristics and relationship of OHC variations in two sub-regions are different for those two periods. $\overline{TH}'_1$ in the EAST and UB have no seasonal dependency because their climatology were removed and the 2-year low-pass filter was also applied to them. And all time series are de-trended before the correlation analysis to focus on understanding the de-trended OHC variations.

3.1.5.1. Relationship between HCA and volume transport through the Korea Strait

The volume transport of the TWC through the Korea Straits is examined to investigate its possible role in the thickness variation of the TWW layer ($\overline{TH}'_1$) in the EAST and UB (Figure 3.12a). Time series of the volume transport used in this study is based on Takikawa and Yoon [2005] from 1976 to 1994 and Fukudome et al.

[2010] from 1997 to 2006. They are all directly-measured transports using the vessel-mounted acoustic Doppler current profiler. The volume transports through the entire Korea Strait, and the eastern and western channels are referred to as VT, EVT, and WVT, respectively. The WVT is larger than the EVT, and its variation is well correlated with the VT variation before 1995 (r = 0.58) and after 1995 (r = 0.88) (Table 3.4). A significant negative correlation exists between the WVT and EVT with a maximum correlation of −0.48 at a two-year lag before 1995. However, the correlation between the WVT and EVT degraded after 1995 and became statistically insignificant after 1995. It should be pointed out that the WVT and EVT show better correlations with the TWW heaving depending on the periods considered rather than the VT and heaving (Table 3.3).

Before 1995, the thickness variation of the TWW layer both in the EAST and UB are negatively correlated with WVT with correlations significant at the 95% CL (Table 3.3), which means that when the WVT is large (small), the TWW layer shoals (thickens) in both regions. It should be noted that the WVT variation has the maximum correlation with $\overline{\mathrm{TH}}'_1$ in the UB at zero lag, while the maximum correlation between WVT variation and $\overline{\mathrm{TH}}'_1$ in the EAST is detected at a two-year lag (WVT leading). This means that when the WVT increases, $\overline{\mathrm{TH}}'_1$ in the UB decreases, followed by a decrease in $\overline{\mathrm{TH}}'_1$ in the EAST after two years. This lead-lag relationship also corresponds to a lag of 24 months of the $\overline{\mathrm{TH}}'_1$ in the UB and EAST with the former leading the latter before 1995. The $\overline{\mathrm{TH}}'_1$ in the EAST is positively correlated with the EVT variation at zero lag before 1995 (Table 3.3).

The correlation analysis between the volume transports through

the Korea Strait and $\overline{TH}'_1$ variations in the EAST and UB before 1995 suggests the following scenario. When the WVT is low, the EKWC extends far to the north resulting in the deepening of the TWW layer and an increase in the HCA in the UB. A larger EVT follows the low WVT after two years, which then ONB develops in the eastern ES and the TWW layer deepens in the EAST resulting in an increase in the HCA in the EAST. There exists a negative correlation between the WVT and $\overline{TH}'_1$ in the UB, the larger the WVT, the weaker the EKWC influence and vice versa. The boundary current separation from the coast is influenced by coastal orientation, bottom topography, and inertia of the current [Ozgokmen et al., 1997]. A numerical model study using a two-layer quasi-geostrophic model showed that an increased volume transport through the Korea Strait leads an early separation of the EKWC due to a combined effect of the inertia and convex-type coastal geometry in its southwestern part [Lee, 1999]. However, the separation latitude moves farther north to about 39°N under a decreased transport condition. If the correlation analysis is performed using VT, it is also negatively correlated with the $\overline{TH}'_1$ variation in the UB at zero lag and the $\overline{TH}'_1$ variation in the EAST at two year lag before 1995 but with weaker relationships as compared to those between the $\overline{TH}'_1$ variations and WVT (Table 3.3). That may be due to a poor correlation between EVT and $\overline{TH}'_1$ in the UB or the EAST.

After 1995, the relationship between the $\overline{TH}'_1$ variation in the EAST or in the UB and transport variations becomes complicated. In the EAST, a significant positive correlation occurs between the $\overline{TH}'_1$ variation and the VT at two year lag but only significant at the 90% CL. In the UB, there is no significant correlation between the

$\overline{TH}'_1$ variation and the WVT, while a significant negative correlation occurs between the $\overline{TH}'_1$ variation and the EVT at one year lag. Moreover, the $\overline{TH}'_1$ variation in the UB which had a negative correlation with the VT before 1995 shows a positive relationship at zero and two year lag after 1995, but only significant at the 90% CL. This change in the relationship between volume transports and the TWW layer thickness after 1995 is not understood and deserves further study. A short data length after 1995 may also lead the correlation analysis as inconclusive.

Table 3.3. The largest correlation coefficients at zero lag (upper part) and lagged correlation coefficients (lower part) between de-trended $\overline{TH}'_1$ in the EAST or in the UB and de-trended climate indices and volume transport components through the Korea Strait. The cross correlation coefficients are calculated with lags up to 2 years with those significant at the 95% confidence level highlighted in bold. Other listed cross correlation coefficients are significant at 90% confidence level. Left (right) number in parentheses denotes lags in months (degrees of freedom). DJF WP, DJF SH, VT, WVT, and EVT denote the winter (December–February) Western Pacific teleconnection pattern, winter Siberian High, total volume transport through the Korea Strait, and volume transports through the western channel and though the eastern channel, respectively.

$\overline{TH}'_1$ (EAST)	DJF WP	DJF SH	VT	WVT	EVT
76–94		**−0.57 (0, 19)**		**−0.49 (0, 19)**	**0.4 (0, 19)**
95–2007	0.42 (0, 13)				
$\overline{TH}'_1$ (UB)	DJF WP	DJF SH	VT	WVT	EVT
76–94	**0.53 (0, 19)**	**−0.61 (0, 19)**	**−0.44 (0, 19)**	**−0.57 (0, 19)**	
95–2007	**0.70 (0, 13)**		0.36 (0, 10)		

$\overline{TH}'_1$ (EAST)	DJF WP	DJF SH	VT	WVT	EVT
76–94			**−0.52 (24, 17)**	**−0.72 (24, 17)**	
95–2007		**−0.50 (24, 11)**	0.46 (24,8)		
$\overline{TH}'_1$ (UB)	DJF WP	DJF SH	VT	WVT	EVT
76–94			**−0.50 (12, 18)**		−0.33 (24,17)
95–2007			0.53 (24, 8)		**−0.75 (12, 9)**

Table 3.4. Cross correlation coefficients between winter SH and WP, between VT and WVT or EVT, and between WVT and EVT. Cross correlation coefficients significant at the 95% confidence level are highlighted in bold. Left (right) number in parentheses denotes lags (degrees of freedom). Parameters on the left column lead those on the right and vice versa.

Lead	Lag	Total period (76–07)	Before 1995 (76–94)	After 1995 (95–07)
DJF SH	DJF WP	**−0.38 (0, 32)**	**−0.50 (0, 19)**	
Lead	Lag		Before 1995 (76–94)	After 1995 (97–06)
VT	WVT		**0.58 (0, 19)**	**0.88 (0, 10)**
VT	EVT		**0.70 (0, 19)**	**0.68 (0, 10)**
WVT	EVT		**−0.48 (2 year, 17)**	

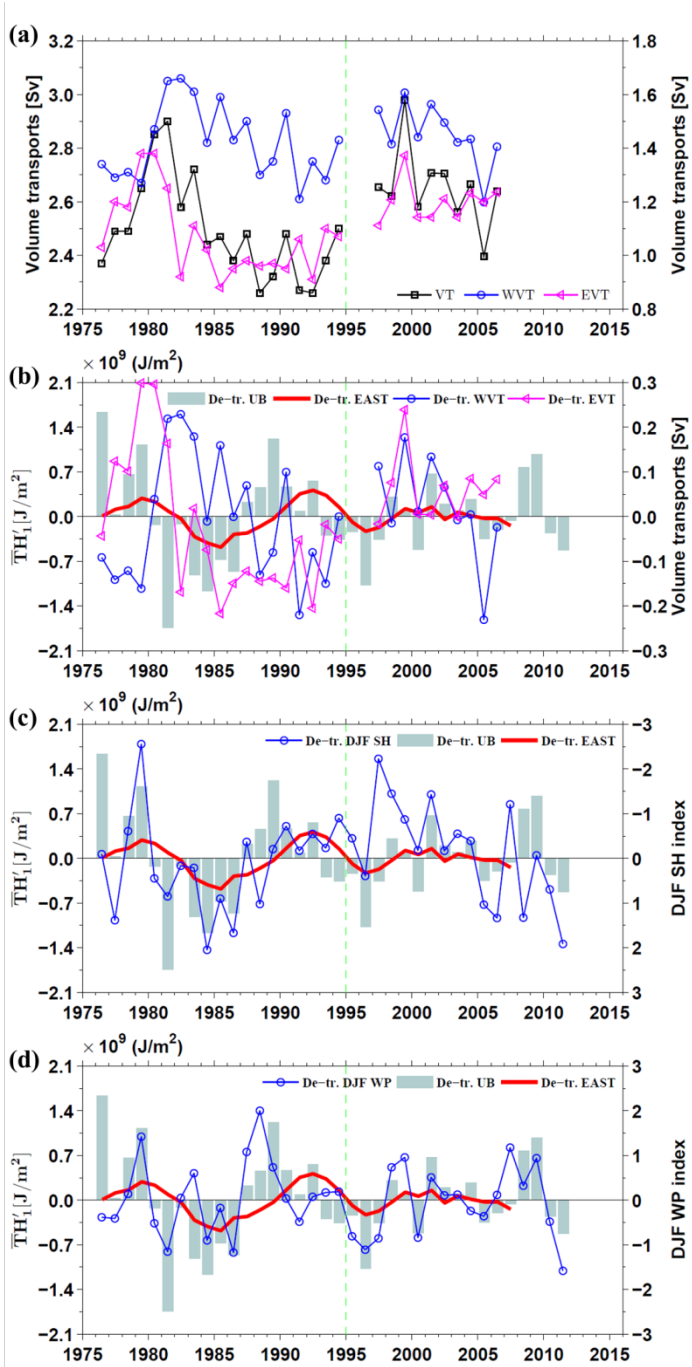

Figure 3.12. (a) Time series of annual mean volume transports through the Korea Strait (VT, black square), the western channel (WVT, blue circle), and the eastern channel (EVT, pink triangle). The left y-axis is for the VT and the right y-axis is for the WVT and

EVT. (b) Time series of annual mean $\overline{\mathbf{TH}'_1}$ in the UB (grey bar), in the EAST (red solid line), WVT (blue circle), and EVT (pink triangle). (c) Time series of wintertime Siberian High (SH) index (blue circle), and annual mean $\overline{\mathbf{TH}'_1}$ in the UB (grey bar) and in the EAST (red line). The right y-axis is for the SH index, with reversed values. (d) Time series of wintertime Western Pacific teleconnection pattern (WP) index (blue line), and annual mean $\overline{\mathbf{TH}'_1}$ in the UB (grey bar) and in the EAST (red line). All time series in (b)–(d) are de-trended.

3.1.5.2. Relationship between HCA and winter wind stress curl

Reports have been given of the importance of wind and/or WSC forcing in the upper circulation of the ES [e.g., Hogan and Hurlburt, 2000; Trusenkova et al., 2009]. Spatial pattern of the winter-mean WSC (Figure 3.13a) is characterized by alternating positive and negative WSC from the area off Vladivostok and to the East Korea Bay (EKB, see Figure 1.3b for locations), which is fairly consistent with those previously documented with other reanalysis products [e.g., Yoon and Kim, 2009]. The annual mean WSC pattern is very similar to the winter WSC pattern because of weak and changeable wind in summer [Nam et al., 2005]. Positive WSC in the northern and northeastern ES generates basin-wide cyclonic circulation in the JB [Yoon et al., 2005]. The positive WSC in the EKB related with development of cyclonic eddy was shown to influence the separation of the EKWC [Kim and Yoon, 1996; Yoon et al., 2005]. Based on results from numerical model experiments, Trusenkova et al. (2009) suggested that the anticyclonic WSC forcing in the southern ES results in the stronger EKWC and northward shift of the TWC.

In order to identify any influence of the winter WSC on the TWW heaving, time series of the winter WSCA over the entire ES and annual mean $\overline{TH'_1}$ in the UB and EAST are compared. The spatial correlation map between the TWW heaving in the UB and the winter WSCA shows significant negative correlations in the northeastern ES (maximum $r = -0.7$) and near the EKB (maximum $r = -0.5$), and also significant positive correlation (maximum $r = 0.3$) off the North Korea coast (Figure 3.13b). Considering the mean WSC pattern (Figure 3.13a), the negative correlations dictate that the weakening of positive WSC in the northeastern ES and in

the EKB is related with an increase in the TWW heaving in the UB. In association with the upper circulation, this implies that the EKWC penetrates farther to the north when the positive WSC in the northern ES, hence the cyclonic circulation in the JB, weakens, resulting in the thick TWW layer and positive HCA in the UB. This scenario is obviously identified in mean SSH distributions (Figure 3.14). From a mean SSH pattern at the period when the TWW heaving in the UB is over $2 \times 10^8\,\mathrm{J/m^2}$ (Figure 3.14b), it is shown that gradients of SSH are weaker than the total period mean state in the subpolar gyre region (shrinking of surface cyclonic circulation) and a northward bending contour which represents development of the EKWC is strongly developed in the UB. When the TWW heaving in the UB is below $-2 \times 10^8\,\mathrm{J/m^2}$ (Figure 3.14c), gradients of SSH are higher in the subpolar gyre region and 1.5 m contour is more shifted to the southward than the total period mean pattern (strengthening of surface cyclonic circulation). And a northward bending contour is hardly found in the UB. Mean SSH at the periods of positive or negative TWW heaving in the UB also show the similar patterns with the above.

The reduced positive WSC in the EKB can also provide a favorable condition for the farther northward penetration of the EKWC. It is considered to make the cyclonic eddy weak, then southward current along east of the Korean coast which can suppress development of the EKWC would be diminished. The strengthening and weakening of the cyclonic circulation in the JB and the associated development of the EKWC in the western ES also explain the SST variations along the subpolar front in relation with the TWW heaving (Figure 3.11a, 3.11b). It is noted that if the annual mean WSCA is used instead of the winter-mean WSCA, no

significant correlation is found, implying that wintertime wind forcing is mainly responsible for the development of the EKWC and OHC variations in the UB.

Contrary to the significant relationship between the TWW heaving in the UB and WSC, the winter WSCA little affects the heaving in the EAST (Figure 3.13c). Significant positive correlation at the 95% CL appears in a small area off the mid-west coast of Japan, but they are weakly correlated with maximum correlation of 0.3. The development of the ONB in the EAST is hardly affected by the changes in the wintertime WSC.

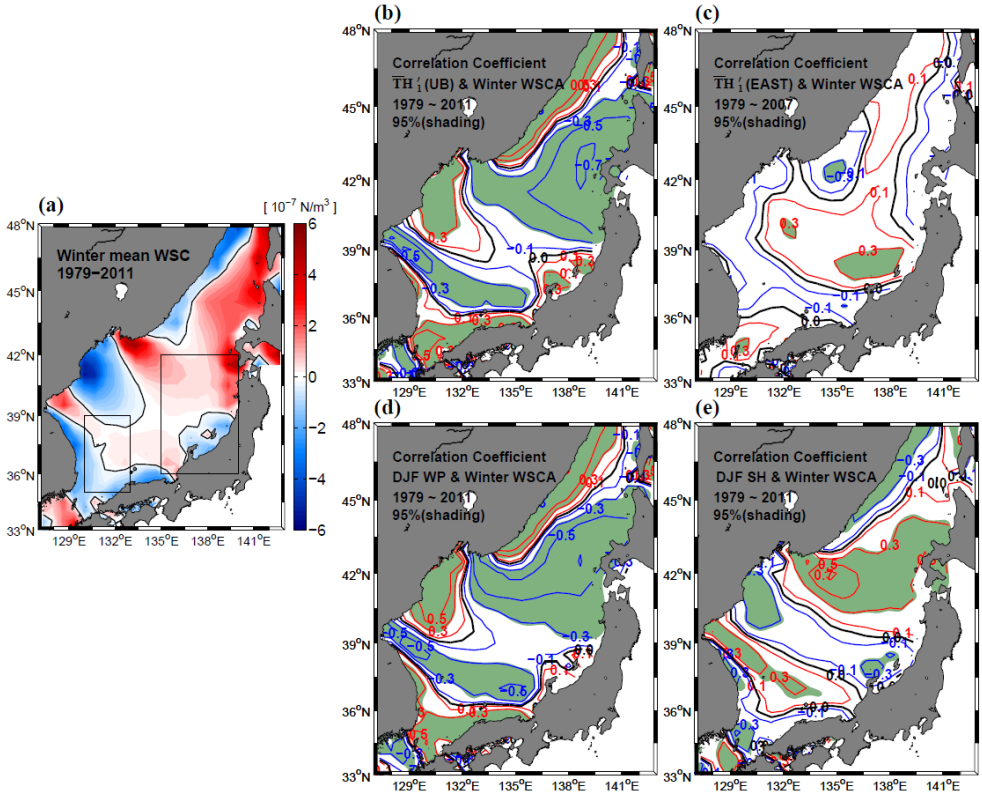

Figure 3.13. (a) Spatial pattern of winter-mean wind stress curl (WSC) (December–February) during 1979–2011. Black contour line denotes the zero WSC. (b) Spatial correlation map between de-trended annual mean $\overline{TH}'_1$ in the UB and the de-trended winter-mean wind stress curl anomaly (WSCA) during 1979–2011. The WSCA is calculated by subtracting the monthly mean WSC. The shaded areas have a significant correlation coefficient at the 95% confidence level. (c) The same as Figure 3.13b, but for correlation between de-trended annual mean $\overline{TH}'_1$ in the EAST and the de-trended winter-mean WSCA during 1979–2007. (d) The same as Figure 3.13b, but for correlation between de-trended winter-mean WP and WSCA during 1979–2011. (e) The same as Figure 3.13b, but for correlation between de-trended winter-mean SH and WSCA during 1979–2011.

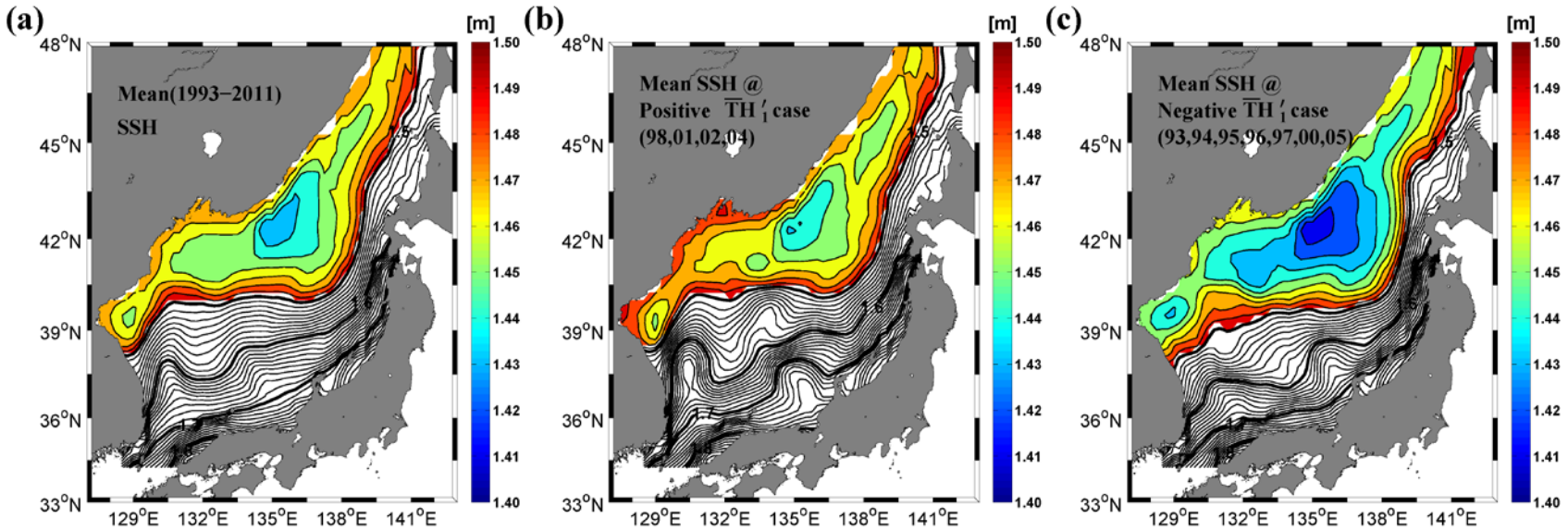

Figure 3.14. (a) The mean sea surface height [m] during 1993–2011 with a color scale shown in the right. An interval of a black (bold) line is 0.01 m (0.1 m). (b) The same as Figure 3.14a, but for the periods when de-trended $\overline{\mathbf{TH}}'_{\mathbf{1}}$ in the UB is over $\mathbf{2 \times 10^8\ J/m^2}$ (1998, 2001, 2002, and, 2004) (c) The same as Figure 3.14a, but for the periods when de-trended $\overline{\mathbf{TH}}'_{\mathbf{1}}$ in the UB is below $\mathbf{-2 \times 10^8\ J/m^2}$ (1993, 1994, 1995, 1996, 1997, 2000, and 2005).

3.1.5.3. Influence of the Siberian High and Western Pacific teleconnection pattern

The significant relationship between the HCA in the UB and winter WSC is shown in the previous section. The WSC field is known to be related with the WP in the North Pacific [Ishi and Hanawa, 2005], and an anomalous anticyclone strengthens in the mid-latitude of the East Asia area north of 30 °N during the positive WP phase [Choi and Moon, 2012]. The wintertime SH, which is closely related with the East Asian Winter Monsoon [Wu and Wang, 2002], is also expected to influence the winter WSC field because the strength of a northwesterly wind is determined by the intensity of the SH and the winter wind field is spatially inhomogeneous (e.g., Kawamura and Wu, 1998; Nam et al., 2005). Here, the relationship between the TWW heaving and the WP or SH is examined. I only consider the winter WP and SH indices because of the significant contribution of winter WSC forcing to the TWW heaving in the UB as mentioned earlier (Figure 3.13b).

The spatial correlation maps between the winter WSCA and the winter WP or winter SH during 1979–2011 show a close relationship between the WSC and those atmospheric indices (Figure 3.13). The winter WP (SH) shows significant negative (positive) correlations with the winter WSCA in the northeastern ES and near the EKB, and significant positive (negative) correlations off the North Korea coast. This relationship implies that the strengthening of the positive WSC in the northeastern ES and the EKB occur during the periods of either the negative phase of WP or the intense SH or both. The correlation maps in further indicate that the OHC variations in the UB is significantly influenced by those atmospheric indices via the variations of the WSC field in

the northern ES (Figure 3.13b, 3.13d, 3.13e).

The correlation analysis confirms that the variation of the TWW heaving in the UB and the WP index are positively correlated with significant correlation at the 95% CL regardless of the periods before and after 1995 with higher correlation of 0.7 during 1995–2007 than the correlation of 0.53 during 1976–1994 (Table 3.3). The SH is also significantly correlated with the TWW heaving in the UB during 1976–1994, and the correlation between the TWW heaving in the UB and the SH is higher than the correlation between the heaving and the WP. No significant correlation, however, is obtained between the TWW heaving in the UB and the SH after 1995. The SH intensity with linear trend decreased since the mid-1980s and marked minimum intensity in the late 1990s, followed by a gradual recovery of its intensity (not shown). Hence, the SH intensity influenced the TWW heaving in the UB when it was strong (1976–1994) through the WSC forcing, while its influence on the TWW heaving in the UB was indistinct when the SH remained weak during 1995–2011.

In the East, correlation between $\overline{TH}'_1$ and DJF WP never exceeds the 95% CL during the two periods before and after 1995. After 1995, it is increased to 0.42 but it just exceeds the 90% CL (Table 3.3). This poor relationship between the heaving in the EAST and the WP is also connected with the poor correlation between the TWW heaving in the EAST and the wintertime WSCA (Figure 3.13c). While the WP affects the ES mainly through changes in the WSC field, the TWW heaving in the EAST is little influenced by the WSC forcing resulting in the poor correlation between the WSC (Figure 3.13c) or the DJF WP (Table 3.3) and the TWW heaving in the EAST.

The correlation analysis between the SH and the TWW heaving in the EAST shows significant negative correlations at the 95% CL before and after 1995 but at zero lag before 1995 and with a two-year lag after 1995 (Table 3.3). Minobe et al. [2004] found the strong decadal co-variability between the SH and the upper layer temperature in the eastern ES during 1957–1996. Na et al. [2011] also suggested that the SH has a good relation with the wintertime heat content change in the ES during 1968–2007. They explain that cold ocean temperature anomalies especially in the eastern ES are generated by strong cold-air outbreaks from the Siberian coast implying an influence of the air-sea het exchange. However, the OHC variations in the EAST are primarily determined by the TWW heaving associated with the upper circulation according to my decomposition analysis.

As was shown in Figure 3.13c, the TWW heaving in the EAST is poorly correlated with the WSC, hence other oceanic forcing associated with the SH would influence the TWW heaving in the EAST. It might be hypothesized that the strong SH in winter accompanying strong northwesterly winds over the ES induces the southwestward Ekman transport, which would then suppress the development of the ONB in the EAST resulting in the reduced HCA in the EAST. Horizontal distribution of wintertime mean wind speed during 1979–2011 shows two areas of wind speed maxima, off Vladivostok and west of the Tsugaru Strait (Figure 3.15a). Dynamic height fields superimposed on winter-mean wind speed distributions in 1986 and 1990, when the respective $\overline{TH'}_1$ in the EAST is negative and positive, show the suppressed ONB towards the west coast of Japan when the wind was stronger in 1986 as compared to the broader ONB in 1990 when the wind was weaker, which seems

to support the hypothesis (Figure 3.15b, 3.15c). However, there were cases when the ONB well developed offshore in the EAST although the northwesterly wind was strong. A spatial correlation map between the TWW heaving in the EAST and wind speeds over the entire ES also does not exhibits any significant correlation. It is left as the future work how the SH influences the OHC variations in the EAST.

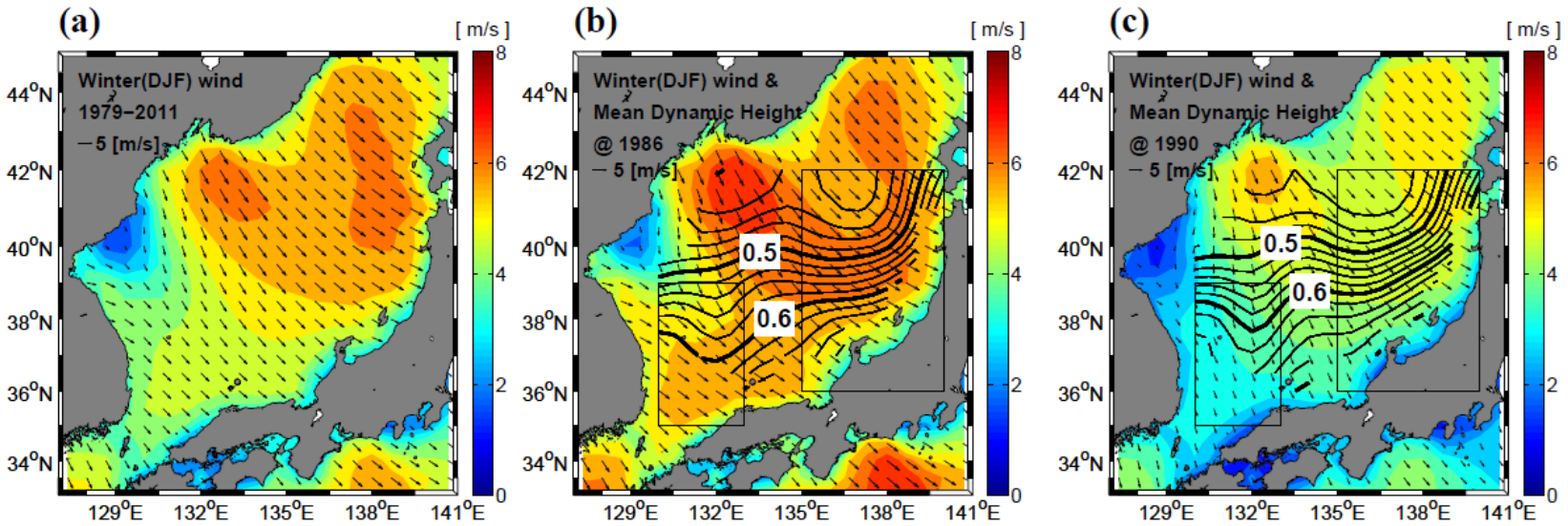

Figure 3.15. (a) Spatial pattern of mean wind vectors and wind speed (color) during 1979–2011. (b) The same as Figure 3.15a, but for the mean wind in 1986. Annual mean dynamic height relative to 500 m in 1986 is also shown with solid lines. (c) The same as Figure 3.15b, but for the mean wind and dynamic height in 1990.

3.2. Re-initiation of bottom water formation in the ES: Another clue to future changes in global ocean

3.2.1. Observations on deep structural changes

At station C, the DSM and UBHL have continuously deepened since 1950, but their deepening rates have significantly slowed down in the recent years (Figure 3.16). The linear trend of the deepening of 0.13–0.15 ℃ isotherms as a proxy of the DSM [Kang et al., 2003b] from 1950 to the mid-1990s is approximately 19 m/year (open circles in Figure 3.16), whereas that of the deepening DSM becomes less than 7 m/year after the mid-1990s (red circles in Figure 3.16). Considering the isotherm proxy after the mid-1990s (purple triangles in Figure 3.16), the linear deepening rate has not significantly changed since 1950 (Table A3). This is partly due to the warming of the deep-water masses below the 500 m in the ES [Kim et al., 2001; Kim et al., 2008], indicating the importance of the DSM in detecting structural changes. The linear deepening rate of the UBHL, defined using DO profiles, was 27 m/year between 1969 and 1994 (open squares in Figure 3.16). It reached close to zero (purple asterisks in Figure 3.16) or only 4 m/year, when defined using θ profiles (magenta squares in Figure 3.16), between 1994 and 2015. Based on these observations, two different fits were applied to represent trends of the deepening isotherms and/or DSM; linear fitting from 1950 to 1998 (linear warming trend) and logarithmic fitting from 1999 to 2015 extending up to 2060 (red lines in Figure 3.16) where the two periods are selected to optimize the results of 1-D advection-diffusion model shown below. Regarding the UBHL based on θ and DO, only one

logarithmic fit was applied for the entire period (1950–2060) (red lines in Figure 3.16).

From 1965 to 2020, the CW−DW boundary is deeper than the linear fit of the boundary projected by the MBBM [Kang et al., 2003b] (red solid vs black dashed lines in Figure 3.16), This indicates more accelerated and decelerated CW−DW boundary deepening before and after 1990s, respectively, than that projected with constant water formation (red solid vs black dashed lines in Figure 3.16). Such changes in the deepening rate of the CW−DW boundary yielded a DSM depth shallower by ~270 m in 2040 than that in the previous projection, e.g., new and old projections yield 1,930 and 2,200 m, respectively. More interestingly, the UBHL is fitted to be markedly shallower than the previous prediction, e.g., 2,700 m vs 3,100 m for 2020 and 2,850 m vs 3,500 m for 2040 (Figure 3.16). New fits to recent observations project that the UBHL or BW would not disappear by the 2040 as previously suggested. Consistent variations of the DSM and UBHL are found using data collected at other stations in the JB (Table A3).

The UBHL deepening is accompanied by declining BW DO in the JB which also slowed down in 2000s (Figure 3.17). The linear rate of the decreasing BW DO was estimated to be −0.76 μmol/kg/year during 1977–1999 for eastern JB [Gamo, 2014](green circles in Figure 1.3b and Figure 3.17) whereas the trend is significantly relieved to −0.45 or −0.38 μmol/kg/year during 1996–2015 based on DO observations at Station C (blue squares in Figure 1.3b and blue solid line in Figure 3.17) and Station E (blue circles in Figure 1.3b and blue dashed line in Figure 3.17), respectively. Linear rate of BW saturation DO was also estimated as negative value due to the warming, − 0.0098 μmol/kg/year during 1979−1998 and

−0.0154 μmol/kg/year during 1996−2015. These results indicate that the decreasing trend of BW DO was significantly slowed down compared to that in the past although the declining rate of BW saturation DO was increased with strong warming in the recent decade. And the slowdown of the decline in BW DO in the 2000s is consistent with the slowdown of the UBHL deepening, supporting formation of more BW than that in the latest decade.

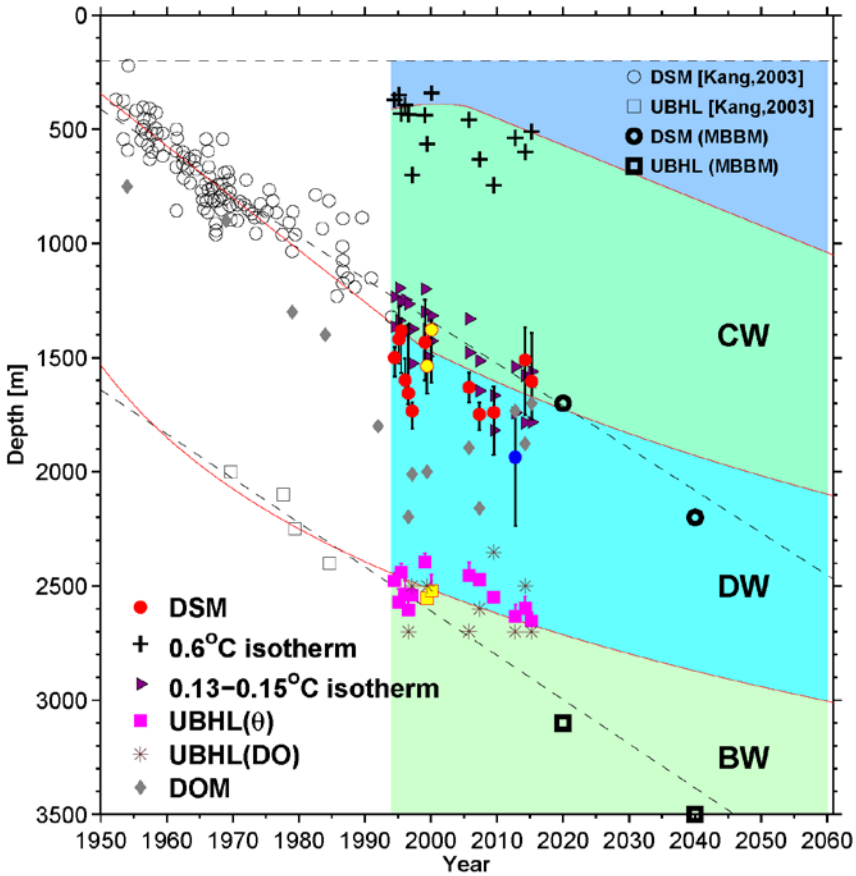

Figure 3.16. Time series of the boundaries between Central Water (CW) and Deep Water (DW) defined by 0.13–0.15 ℃ isotherms (open circles [Kang et al., 2003b] and purple triangles) or deep salinity minimum (DSM, red circles), between DW and Bottom Water (BW) or upper limit of benthic homogeneous layer (UBHL, derived from potential temperature; magenta squares or dissolved oxygen; open squares [Kang et al., 2003b] and brown asterisks), and depth of dissolved oxygen minimum (DOM, grey diamond) for 67 years from 1950 to 2016. Isotherms of 0.6 ℃ used for upper boundary of CW are shown with crosses. Data collected in 1999 (June), 2000, and 2001 using different Conductivity-Temperature-Depth (CTD) instruments are shown with yellow circles and squares. The DSM observed in 2012 is denoted with a blue circle.

Three black dashed lines denote the upper boundary of the CW fixed at 200 m, and linear fits to the observed CW–DW and DW–BW boundaries (from top to bottom), previously reported using data from 1950 to 1996 [Kang et al., 2003b] (not shaded). Red solid lines are new fits to the up-to-dated boundaries. Vertical bars indicate an uncertainty of the boundary depth.

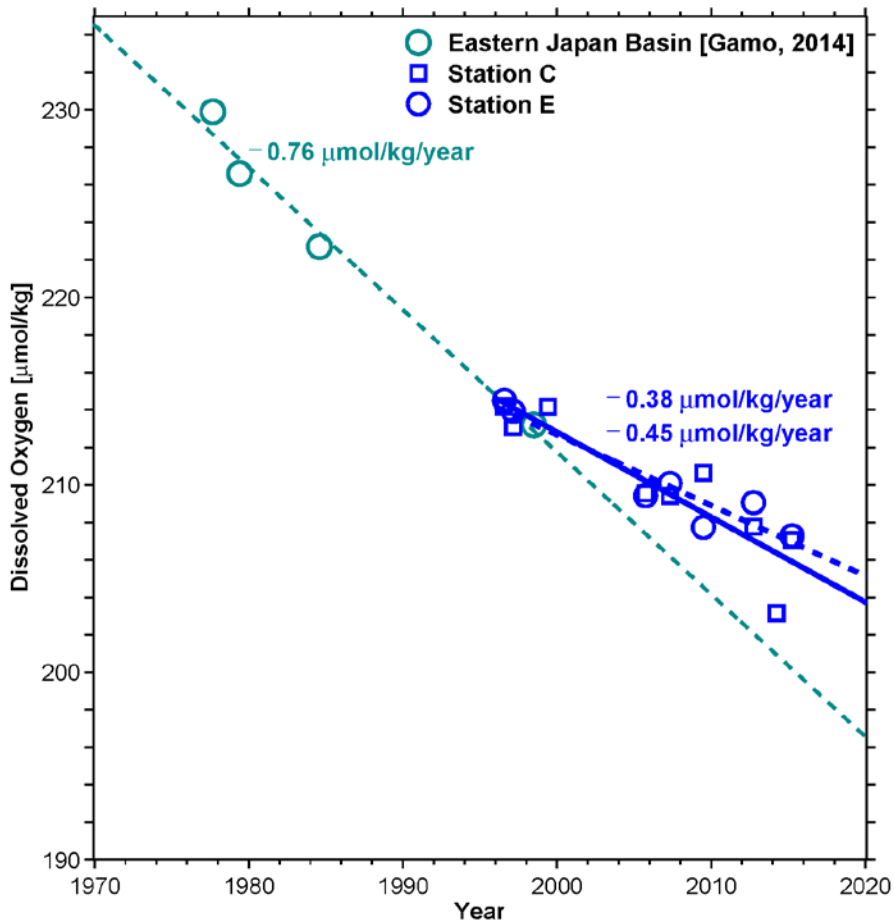

Figure 3.17. Time series of Bottom Water (BW) dissolved oxygen (DO) observed from 1977 to 2015 in the Station C (blue squares), Station E (blue circles), and eastern JB (green circles) [Gamo, 2014] where are shown in Figure 1.3 as blue square, blue circle, and green circle, respectively. A green dashed line indicates a linear trend of declining BW DO in the eastern JB between 1970 and 2020, derived using data collected from 1977 to 1999. The blue dashed (solid) line shows for the same linear trend between 1996 and 2020 but with data collected at Station E (Station C) from 1996 to 2015.

3.2.2. 1-D advection-diffusion model

Kim and Kim [1996] first suggested the regime shift of deep ventilation system in the ES using the results of 1-D advection-diffusion model with CTD data observed at the JB in August, 1996. However, results of 1-D advection-diffusion model estimated from profiles at station C in April, 2015 are quite different with those in 1996 (Table 3.5). First of all, θ (DO) at the boundary depths is significantly increased (decreased) in 2015. And the Z^* values in CW (DW) is reduced (increased) from 0.571 (0.564) to 0.453 (0.945) km. It would be interpreted as weakening (strengthening) of diffusion/mixing and/or strengthening (weakening) of upwelling velocity in CW (DW). Moreover, J/w in CW has a negative sign and its magnitude is even bigger than that in DW while the absolute value of J/w in DW is significantly decreased. That is, contrary to the results in 1996, DO supplement into CW is stagnated but DO is more convectively added to DW in 2015. To examine changes of Z^* and J/w more precisely, the 1-D advection-diffusion model is applied to θ and DO profiles observed at station C in each cruises (Figure 3.18). The upper and lower limits of CW and DW for applying the 1-D advection-diffusion model are denoted in Table A4. The J/w and Z^* before 1994 shown in Figure 3.18 are the results of 1-D advection-diffusion model by using the θ and DO profiles at the JB digitized from previous studies [Kim and Kim, 1996; Chen et al.,1999].

The Z^* values for CW (DW) obtained from the θ profiles shows decreasing (increasing) tendency during 1996 and 2015 as shown in the comparison between the results in 1996 and 2015 (Figure 3.18a). But if the period is extended to 1950, the Z^* values for CW

and DW generally increase in time, indicative of an enhanced diffusion/mixing and/or weakened upwelling, but remain below 1.0 km, and are always higher for DW than for CW (Figure 3.18a). Such high Z^* values for DW in the last decade is more consistent with a typical range of Z^* in the North Pacific (0.8–1.0 km) [Chen et al., 1999] than before (0.4–0.6 km). Low Z^* values denote the importance of upwelling relative to diffusion/mixing in determining curvature of θ profiles, and are found for CW (when compared to DW) and for the previous (when compared to the last) decades (Figure 3.18a and 3.18b).

However, the long-term trend in Z^* for CW and DW should be carefully investigated because the Z^* values before 1990 obtained from θ profiles with discrete bottle samples would be underestimated as the curvature of θ profiles is strengthened when the number of sampling depth is small. A difference between the Z^* values (Figure 3.18a) and Z* estimated with subsampled θ profiles during 1994–2015 actually yields from 0.2 to 0.4 km. Moreover, the Z^* values for DW are more sensitive to selection of the layer than those for CW. For example, Z^* for DW in 2007 (February, 1996) increase up to 1.8 (1.2) km with extending the DW layer by 100 m. For the CW, such extended layer hardly affects to Z^* and J/w except 2005 when J/w significantly varies from −7.3 to 0.7 μmol/kg/km. In this case, a mean value (−3.3 μmol/kg/km) is used (Figure 3.18c).

More importantly, the J/w values obtained from the DO profiles (for given Z^* values) also significantly vary in time and among the water masses (Figure 3.18c). In the 1990s, highly positive J/w values for CW (more than +25 μmol/kg/km) with an increasing trend are found for CW and negative J/w values (less than

– 10 μmol/kg/km) with a decreasing trend are found for DW, indicating increased (decreased) convective supply of DO to CW (DW) layer. This implies a shift of the ventilation system from DW (particularly below DOM and BW) to CW above DOM in the 1990s, as previously suggested [Minami et al., 1999; Kim et al., 2001; Gamo et al., 2001; Kim et al., 2002a; Kang et al., 2003b]. Note that the DOM had continuously deepened during the 1990s as compared to that towards the end of the 1970s (DO profiles no. 1 vs no. 2 in Figure 3.18d). In the 2000s, however, *J/w* values for CW abruptly decreased and its sign changed from positive to negative with zero crossing in 2005, indicating reduced CW formation in 2000s. However, *J/w* values for DW clearly increased, approaching zero in 2016 (Figure 3.18c) with shallower DOM (DO profiles no. 2 vs no. 3 in Figure 3.18d). Another shift in the ventilation system from CW back to BW and DW below DOM accounts for such *J/w* changes, and the consequent slowdown of the BW DO declining rates (Figure 3.17 and Figure 3.18d). The DOM had continuously deepened by the mid-1990s as previously reported [Gamo et al., 1986; Kim and Kim, 1996; Chen et al., 1999] but the trend reversed in 2000s and became as shallow as 1,700 m in 2015 (vs 2,200 m in 1996) with less clear (smeared) DOM structures (grey diamonds in Figure 3.16, Figure 3.18d and Figure A3) supporting more DO supplied into the deep-water masses (BW and DW below DOM) in 2000s.

Table 3.5. Compare the boundary values and fitting coefficients (Z^*, J/w) between 1996 and 2015 applied in the 1-D advection-diffusion model.

August, 1996	Layer	Item	q at Z_0	q at Z_m	Z^* [km]	J/w [μmol/kg/km]
		Depth [m]	1500	800		
	CW	θ [℃]	0.1183	0.2798	0.571	+27
		DO [μmol/kg]	222	238		
		Depth [m]	2500	1600		
	DW	θ [℃]	0.0645	0.1082	0.564	−18.4
		DO [μmol/kg]	219	219		
April, 2015	**Layer**	**Item**	q at Z_0	q at Z_m	Z^* [km]	J/w [μmol/kg/km]
		Depth [m]	1400	800		
	CW	θ [℃]	0.1752	0.3575	0.453	−4.2
		DO [μmol/kg]	206	208		
		Depth [m]	2650	1650		
	DW	θ [℃]	0.0929	0.1404	0.945	−3.2
		DO [μmol/kg]	207	206		

※ Z_0 (Z_m) is the lower (upper) boundary depth for each layer.

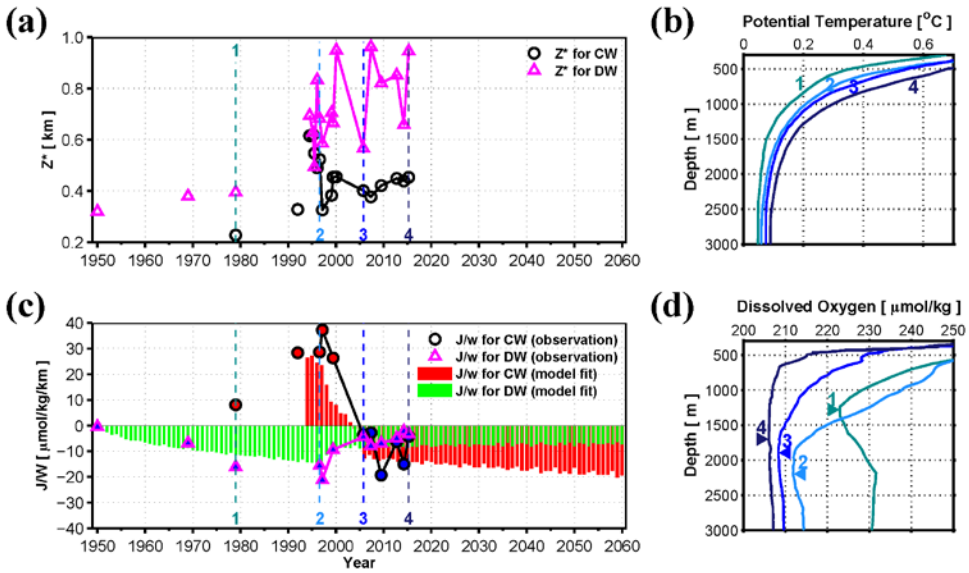

Figure 3.18. (a) Time series of *Z** at station C. *Z** values for CW and DW are shown with magenta triangles and black circles, respectively. (b) Vertical profiles of potential temperature for four periods (1979, 1996, 2005, and 2015) marked with vertical dashed lines in Figure 3.18a and 3.18c. (c) Time series of *J/w* at station C. *J/w* values for CW and DW are shown with magenta triangles and black circles, respectively, filled with red (positive) and blue (negative) colors. *J/w* for CW and DW, independently estimated from the water boundary fits shown in Figure 3.19b (J/w_{MOD}), is shown with red and green vertical bars, respectively. (d) The same as Figure 3.18b, but for dissolved oxygen.

3.2.3. Significant role of convective DO supply for changing deep-water structures

The DO source term (J) is decomposed into the convective supply (J_C) originating from the surface of the northern ES and biological consumption (J_B), i.e., $J = J_C - J_B$. Then, the J_C can be expressed as below [Kang et al., 2004b]:

$$J_C\ [\mu\text{mol/kg/year}] = C_0 \times Q/V$$

where C_0 is surface water DO in μmol/kg, Q is volume transport from the surface to the deep-water in km^3/year, and V is volume of the deep-water mass in km^3. Then, the source term J/w

$$J/w = J_C/w - J_B/w = C_0/w \times Q/V - J_B/w$$

is estimated from time-varying Q and V obtained from the time rate of changes in CW and DW volumes from the fits shown in Figure 3.19 assuming C_0/w and J_B/w are constant in time. To calculate the volume of CW, the upper boundary of CW defined as the 0.6 ℃ isotherm depth [Kim et al., 2004] (plus symbols in Figure 3.16) is additionally fitted to a two-dimensional curve from 1994 to 2005 and a linear line after 2005. The volume changes of CW, DW, and BW are then estimated by using the linear relationship between depth and area [Kim et al., 2002a] (Figure 3.19). The J_B for CW (DW) was estimated to 1.73 (0.75) μmol/kg/year by the minimum complexity water mass model with chemical tracer data observed in the ES [Jenkins, 2008]. The C_0 is set to 320 μmol/kg as used previously [Kang et al., 2004b], yielding J_B/w of 7.3 (1.4) μmol/kg/km for CW (DW) with the constant C_0/w of 1350.2 (616.6) μmol/kg/km/year.

The magnitude and temporal structures of *J/w* values modelled using the above equation for the period from 1950 to 2060 (J/W_{MOD}, vertical bars in Figure 3.18c) are consistent with those derived from observed vertical *DO* structures (symbols in Figure 3.18c). The two independent approaches (derived from modelled and observed results) commonly show the highly positive *J/w* in mid-1990 and abrupt decrease in mid-2000 for CW, and low negative *J/w* value in mid-1990 and abrupt increase in mid-2000 for DW. If I assume that surface saturated DO (C_0) is linearly decreased from 340 to 300 μmol/kg during 1930-2080 due to the warming of SST, reconstructed *J/w* values almost show the same result with the modeled *J/w* values in Figure 3.18c (vertical bars). RMS difference between them is 0.36 μmol/kg/km for CW and 0.14 μmol/kg/km for DW. The successful reconstruction of *J/w* with temporal changes in the deep-water boundary and volume suggests that *J/w* variations are primarily controlled by the rate of deep-water formation rather than biological consumption (appropriate assumption of time-varying J_C and constant J_B). Thus, the slowdown of CW formation and re-initiation of ventilation into the BW (and DW below DOM) accounts for the observed changes in deep-water structure.

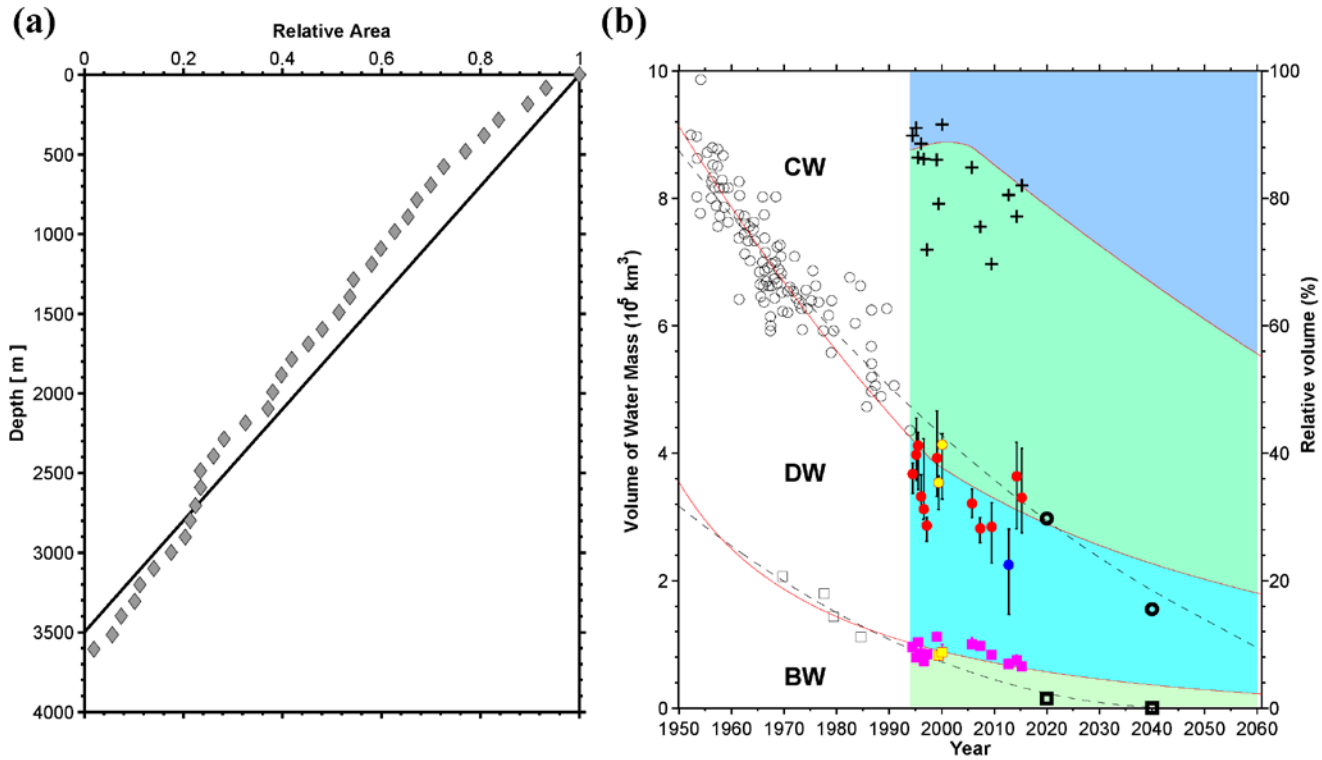

Figure 3.19. (a) Relationship between East Sea area and corresponding depth digitized from Kim et al. [2002a]. (b) Time series of the volumes of CW, DW, and BW calculated from the linear relationship of Figure 3.19a. Markers are the same as Figure 3.16.

3.2.4. Winter surface atmospheric and oceanic conditions associated with ES ventilation system change

The CW–DW (DW–BW) boundary fitted to the observations (Figure 3.16 and Figure 3.19b) and the DO source term modelled using the above equation (J/w_{MOD}) are extended to 2060 for CW (DW) (Figure 3.18c), which provides a new projection of ventilation. The new projection suggests continuous reduction of deep-water masses but with changed rates for different waters. CW (DW and BW) is reduced with increasing (decreased) rates because of decreasing of CW (increased BW). BW is believed to be formed by the slope convection of highly dense surface water along the continental slope in the northern coast, e.g., off the Peter the Great Bay [Talley et al., 2003; Tanaka, 2014]. As mentioned in section 1.3.2, in winter 2000–2001, newly formed BW by the slope convection of dense surface water with properties of very low θ (as severely cooled), high salinity (brine injected while forming sea ice), high DO, and low nutrients, was observed in the vicinity of the station C [Kim et al., 2002b; Lobanov et al., 2002; Senjyu et al., 2002; Tsunogai et al., 2003]. The deep slope convection in winter 2000–2001 was reproduced by using the streamtube model [Tanaka, 2014] where the dynamics of the descending water along the slope are accounted for by the interaction between bottom friction and water entrainment in a stratified, rotating system [Smith, 1973; 1975]. Based on the streamtube model, the dense surface water normally descends to below 1,500 m corresponding to BW along the slope. On the other hand, the CW is considered to be formed by the open-ocean convection of relatively less dense surface water. Thus, more BW and less CW formation implies that winter sea surface

density (SSD) in the northern ES (a purple box in Figure 3.20) became higher in the recent decades, caused by factors such as more severe cooling, more brine rejection, less freshwater and less heat fluxes. A previous study suggested that increased salt flux by transport of TWC enhanced SSD over northern ES from the 1990s to 2000s [Park, 2007], whereas this paper discussed changes in SSD by air-sea fluxes and the effect of brine rejection in the last decades.

The SSD is primarily determined by atmospheric forcing, e.g., net heat flux and fresh water flux. So the flux anomalies obtained by removing the averaged patterns in winter are investigated to know how the flux anomalies every winter affect to SSD changes in comparison with the mean winter condition. In this study, the net heat flux is positive when ocean loses heat and fresh water flux is positive when evaporation exceeds precipitation. The winter mean net heat flux and fresh water flux are totally upward in the ES (Figure 3.20).

First of all, a positive linear relationship (r = 0.86) exists between anomalies of net heat and fresh water fluxes at the sea surface, which reinforced to control SSD during 1980–2016 (Figure 3.21). Positive net heat flux (cooling) and positive fresh water flux (salinization), which increase SSD, are more common either before 1990 (grey circles in Figure 3.21) or after 2000 (red circles in Figure 3.21) than 1990s' (blue circles in Figure 3.21). Time-integrated fluxes show such contrasting conditions between 1990s(blue square in Figure 3.21) and 2000s(red square in Figure 3.21). During the winter between 2000 and 2001, when the deep slope convection was observed [Kim et al., 2002b; Lobanov et al., 2002; Senjyu et al., 2002; Tsunogai et al., 2003], both heat and

fresh water flux anomalies are strongly positive (red star in Figure 3.21).

To examine temporal changes of temperature and salinity in determining SSD, wintertime sea surface salinity (SSS) change (blue filled circles in Figure 3.22) is estimated from the fresh water flux anomaly during 1980–2016 by using a highly correlated (r = 0.80), linear relationship, at a lag of one month (flux leads), between the flux and the salinity observed at the uppermost depth for the 19 cruises in the northwestern ES (a black box in Figure 3.20). Similarly, the wintertime SST change (red triangles in Figure 3.22) is estimated from the net heat flux anomaly for the same period by using the one month lagged linear relationship between the flux and AVHRR SST in the area (r = −0.82, flux leads). The method above is used to determine changes in SSS and SST associated with surface air-sea fluxes only. The linear regression of net heat flux to SST explains 62 % of variance in the AVHRR SST, indicating a significant role of the air-sea heat exchange. It is also suggested that the atmospheric cooling plays an important role for occurring the deep convection in the northern ES together with the salt flux of the TWC [Park, 2007]. As shown in the good positive relationship between net heat and fresh water flux anomalies (Figure. 3.21), the SSS and SST averaged over the northwestern ES (a black box in Figure 3.20) clearly demonstrate cold and saline (high SSD) surface conditions in 2000s and before 1990 compared to the 1990s (red triangles and blue circles in Figure 3.22).

Surface buoyancy flux anomalies into the northern ES (bars in Figure 3.22) are also quantified by combining the net heat and freshwater fluxes following the method previously suggested [Speer and Tziperman, 1992]. These anomalies show

more positive values (increasing SSD) in the last decades than the 1990s and the sign of its 5-year running mean time series shifted from negative to positive in late 1990s and early 2000s (black bold line in Figure 3.22). If I convert positive surface density flux anomalies in the 2000s into water mass transformation rates on the assumption that an isopycnal outcrop area is the black box region in Figure 3.20 with $\Delta\rho = 5\,\mathrm{kg/m^3}$, water mass transformation rates [Speer and Tziperman, 1992] are estimated from 0.28 to 0.48 Sv similar with the total rate of deep-water formation in MBBM (~ 0.49 Sv) [Kang et al., 2003b].

HCA is also estimated using NA12 data in a black box region in Figure 3.20. HCA in the northern ES shows an increasing trend ($1.24\pm1.50\,\mathrm{J/m^2/month}$) during 1976−1994 but after that, its trend becomes very weak ($0.02\pm0.40\,\mathrm{J/m^2/month}$). As shown in the net heat flux and winter SST changes in the recent decade, slowdown of the warming is also detected in the upper ocean (0−500m) in the northern ES.

Because the SSD is likely more affected by the time-integrated freshwater flux than heat flux in 2000s contrasting other periods (red square in Figure 3.21), the increased SSS may primarily (and decreased SST secondly) enhance slope convections in the northern ES. Furthermore, changes in brine rejection with sea ice formation in the northern ES could also contribute to the increased SSS, and thus SSD since the late 1990s. Winter sea ice concentration in the Tartarsky Strait (area shown with black dots in Figure 3.23a), which had a significant decreasing trend ($-0.75+0.49\,\%/\mathrm{year}$) before 1995 (green line in Figure 3.23b), was increased about 8% in the late 1990s and it has been maintained interannual variations with no significant trend after 1995 (a blue

line in Figure 3.23b). Sea ice concentration in the Tartarsky Strait is thought to co-vary with that in front of the Vladivostok due to the strong connection between two regions by the Liman Cold Current along the Primorye coast (Figure. 1.4a) so its variations represent sea ice variations in the northern ES. Thus, we believe the high SSD condition is caused primarily by increased SSS via enhanced air-sea freshwater flux (more evaporation) in the northern ES, more brine rejection in the Tartarsky Strait, or more salt flux from the TWC into the northern ES [Park, 2007], and then secondarily by decreased SST via severe cooling in the northern ES. All these factors are responsible for more active BW formation through the slope convection in the recent decades.

In contrast to the enhanced slope convection, open-ocean convection forming CW, represented by thick well-mixed layers [Talley et al., 2003], decreased with reduced mixed layer depth (MLD). The MLD deeper than 500 m, considered to be suitable for CW formation [Talley et al., 2003], was observed in 37 (among 1545 in total) θ profiles observed during 1995–2000 in the northwestern JB, and the maximum MLD reaches deeper than 1,200 m (color symbols in Figure 3.23a). However, such a deep (> 500 m) MLD is found in only 2 (among 665 in total) θ profiles during 2000–2004 (after winter 1999–2000 when the latest open-ocean convection was observed [Talley et al., 2003]). In short, the results indicate significantly reduced probability of the open-ocean convection in the 2001–2004 compared to the 1995–2000, accounting for the CW reduction with negative J/w in the last decade (Figure 3.16, 3.18c and 3.19b).

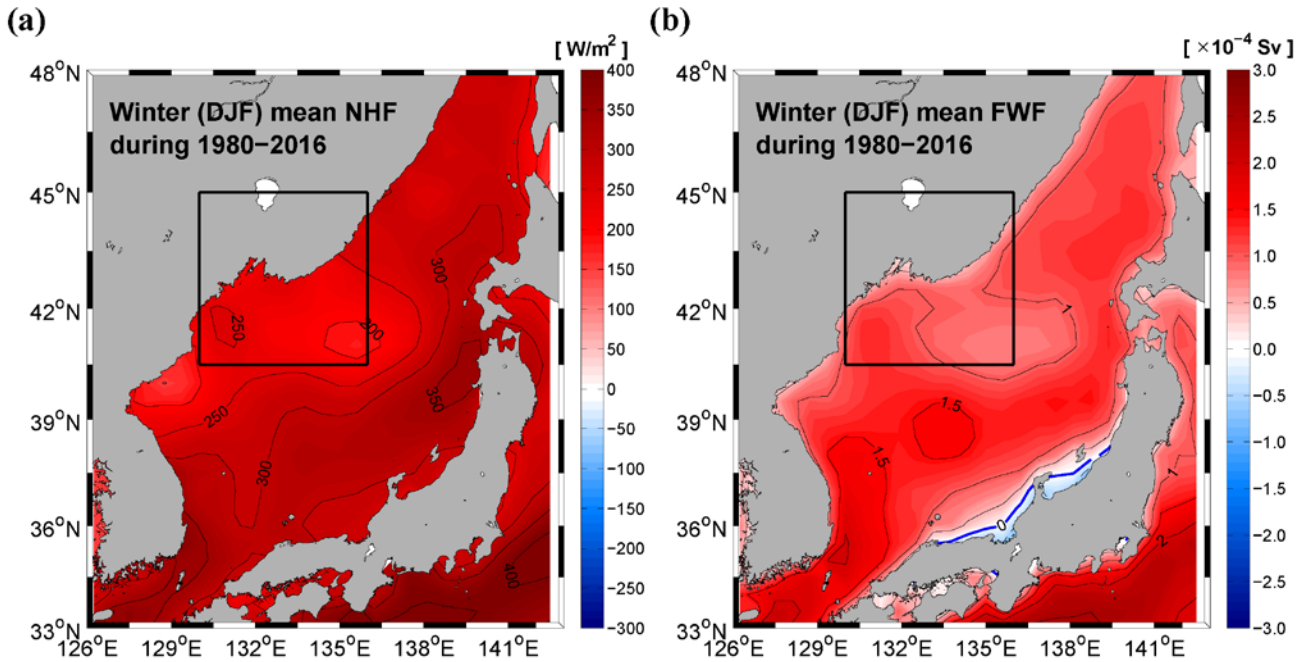

Figure 3.20. (a) The winter (DJF) mean net heat flux (NHF) during 1980–2016. The northwestern East Sea where the surface fluxes are averaged (see texts for details) is remarked with a black box. The NHF is positive when ocean loses heat. (b) The same as Figure 3.20a, but for the fresh water flux (FWF). The FWF is positive when evaporation is larger than precipitation.

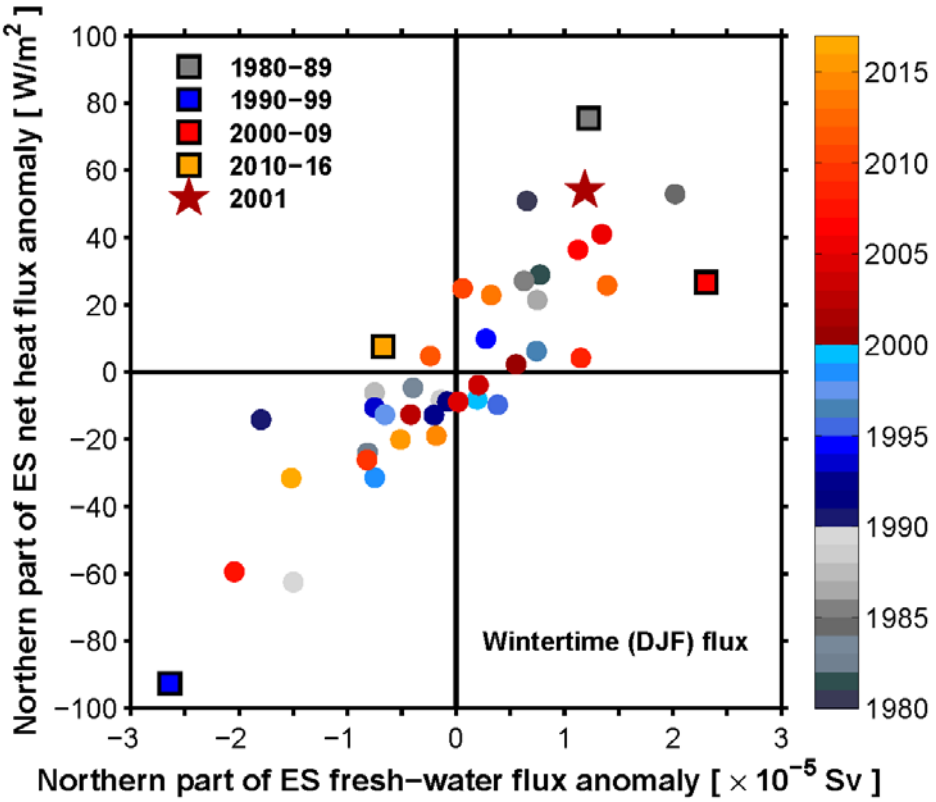

Figure 3.21. Winter (DJF) fresh water flux anomaly (evaporation minus precipitation; positive when ocean loses freshwater) vs. net heat flux anomaly (positive when ocean loses heat) averaged in a black box region in Figure 3.20 during 1980–2016. The integrated anomalies of fresh water and heat fluxes for 10-year-segments starting from 1980 are shown with colored squares (1980s, 1990s, and after 2000s are marked with grey, blue, red, and orange colors). The red star denotes the case of 2000–2001 winter when the slope convection was observed with sufficiently high sea surface density (SSD).

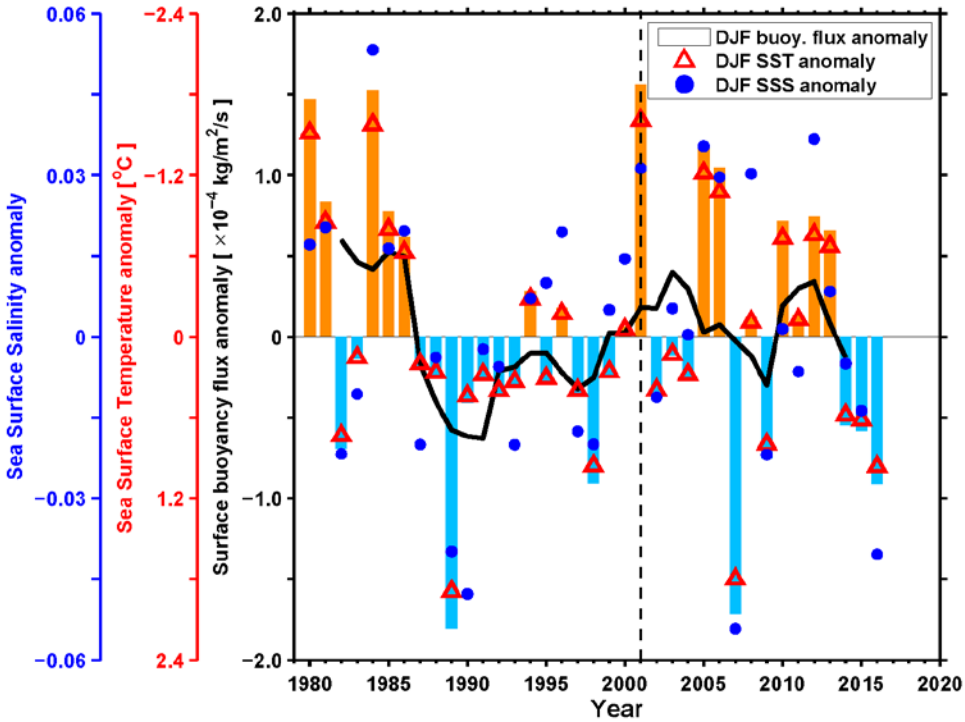

Figure 3.22. Changes in sea surface salinity (SSS, blue circle) and sea surface temperature (SST, red triangle), both averaged over the area marked with the black box in Figure 3.20, regressed from the flux anomalies. The surface buoyancy flux anomaly out of (into) the area is represented by vertical orange (sky blue) bars with 5-year running mean (thick black line). The y-axes are for the changes of SSS (blue), SST (upside down, red), and surface buoyancy flux (black). And a black dashed line indicates values in winter, 2001.

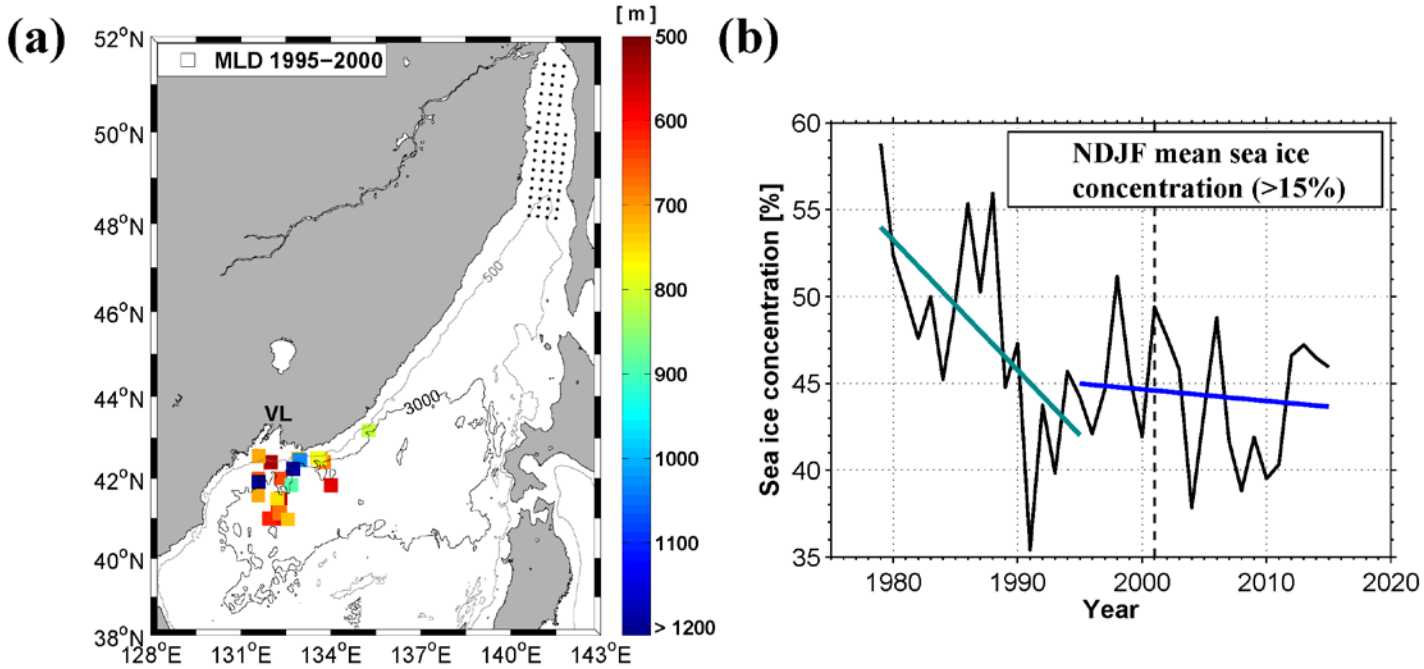

Figure 3.23. (a) Locations where the winter mixed layer depth deeper than 500 m was observed for the period 1995–2000 with a color scale shown in the right. (b) Time series sea ice concentration [%] (cases exceeding 15% only) averaged over the Tartarsky Strait region (marked with black dots in Figure 3.23a) from November to February between 1979 and 2015 (black line), and its linear trends from 1979 to 1995 (green line) and from 1995 to 2015 (blue line). VL denotes the Vladivostok, Russia.

4. Discussion

4.1. Comparison between variations in the recent decade and those in the past

Physical properties of seawater in the ES commonly have shown significant changes since the mid-1990s or the early 2000s. First of all, for the upper ocean heat content change, before 1995 when the out-phase periods are dominant, HCA in the UB was mainly varied in a quasi-decade period, influenced by WVT and winter WSC forcing related with SH and WP. HCA in the EAST was also characterized by quasi-decadal fluctuations affected by EVT and the strength of the SH so it was highly correlated with HCA in the UB, although HCA in the UB leads the HCA in the EAST about two years. However, HCA in the UB shows interannual variations rather than decadal fluctuation in association with winter WSC forcing only related with WP after 1995. And, relations between HCA in the EAST and SH becomes insignificant at zero lag and causative factors for HCA in the EAST are inconclusive. Due to these variations, HCA in the EAST and UB becomes uncorrelated.

As finding from structures and DO of deep-water masses, the ES ventilation system was shifted from bottom to intermediate/deep layers in mid-1990s and its primary reason was considered as low SSD conditions in the northern ES due to the global warming. However, local buoyancy flux has been increased by cooling, brine rejecting and salt flux of the TWC since the early 2000s, providing an evidence for maintaining the three-layered deep-water structures with re-initiation of the BW formation in the recent years.

Thus, the variations of physical properties in the upper and lower layer of the ES in the recent decade which are quite different from those in the past would imply a possibility of changing the conditions or processes determining physical properties of seawater after the mid-1990s or early 2000s. And it may be associated with the North Pacific regime shift in 1998/1999, which is characterized by a significant warming in the southwestern and central North Pacific and a prominent cooling in the Northwestern and eastern North Pacific [Jo et al., 2013].

4.2. Warming effect on physical properties of seawater changes in the ES

Among the variations of physical properties of seawater in the ES, the changes due to the global warming are found in the warming effect of the TWW layer and deep ventilation system in the mid-1990s. The warming effects of the TWW layer in all sub-regions of the ES have linear increasing trends during 1976-2007 which are significant at 90% CL except the WEST case (Table 3.2 and Table A2). Along with the warming of the TWW layer, effects of warming of the thermocline layer in the EAST and EJS, and JSPW layer in all sub-regions also have linear increasing trend during the same period (Table 3.2 and Table A2). However, the warming effects of each layer are not the main driver for HCA variations and only contributed to below 4% of HCA.

The CW replaced the BW with more CW and less BW formation in the mid-1990s due to the global warming. An effect of warming induces forming less dense surface water which is hard to be convected to the bottom layer and then the ES ventilation mainly

occurred in the intermediate and deep layers rather than the bottom layer. Warming of temperature below 500 m (about 0.45 ℃) is also detected in historical θ profiles observed at the northern ES during 1969–2007, but it is shown to be hardly related with the recent structural changes.

4.3. Non-warming effect on physical properties of seawater changes in the ES

Non-warming effects on physical properties of seawater changes in the ES are identified in many ways. First of all, it is confirmed that the heaving effect of the TWW layer related with the upper ocean circulation changes is the main factor for HCA variations. In other words, HCA in the UB (EAST) is mainly determined by the affection of the EKWC (ONB). The causative mechanism for the development of the EKWC is considered as the meridional shift of the subpolar front by WSC forcing in the northern ES. And the WVT has the out-phase relations with the heaving effect of the TWW layer in the UB before 1995. The development of the ONB would be suppressed by the strong winter monsoon. And the EVT shows the in-phase variations with the heaving effect of the TWW layer in the EAST before 1995.

The ES ventilation system has been changed by enhancing BW formation since the mid–1990s with the high SSD influenced by strong surface buoyancy flux (cooling and brine rejection) into the northern ES. The increased VT from 1990s to 2000s also contributed to the high SSD with salt flux [Park, 2007].

4.4. Implications for the global ocean

From the results of distinguishing the warming and non-warming effects, it can be concluded that non-warming effects are more important than warming effects to determine the recent changes of physical properties of seawater in the ES. By the way, the importance of heaving effects on ocean heat content variations and a possibility on global MOC re-strengthening in the recent decade have other meanings for the global ocean.

4.4.1. Importance of the heaving effect on ocean heat content variations

In the North Atlantic Ocean, a warming trend of OHC over the past 50 years is spatially non-uniform; a warming in the sub-tropics and tropics whereas a cooling in the subpolar region [Lozier et al., 2008]. It was suggested that the OHC variations are mainly influenced by wind and buoyancy forcing associated with the North Atlantic Oscillation (NAO) index. Especially, the sub-tropics warming is due to an isotherm deepening with strengthening of the subtropical gyre by wind stress changes related to the continuous positive NAO in recent years [Visbeck, 2003; Leadbetter et al., 2007; Lozier et al., 2008].

The heaving effect is also important on the long-term trends in OHC of the Southern Ocean. The OHC in the upper 1,000 m of the Southern Ocean has been substantially warmed since the 1930s and the warming signal is predominant within the Antarctic Circumpolar Current (ACC) [Gille, 2008]. A poleward wind shifts associated with the positive phase of Southern Annular Mode (SAM) induces a

poleward migration of ACC and then, the OHC in the Southern Ocean is increased. In addition, the South Pacific subtropical gyre is also strengthened in recent decade by an intensification of positive WSC east of the New Zealand under the positive SAM index [Roemmich et al., 2007; Hill et al., 2008]. Due to the spin-up of the gyre, temperature or dynamic height of this region has been significantly increased since the early 1990s [Roemmich et al., 2007; Hill et al., 2008].

It is concluded that the upper OHC variation in the ES which has an east-west contrast trend is primarily controlled by the heaving effect of the TWW layer and causative factors for the upper ocean circulation changes are considered as the local wind or WSC forcing related with the WP and SH index. Overall, the ES OHC variations have many things in common with those in the global ocean, supporting the idea of 'miniature ocean, East Sea'.

4.4.2. A possibility on global MOC re-strengthening

Senjyu et al. [2002] suggested that the BW formation in winter 2001 would not only supply DO in the bottom layer but also strengthen the thermohaline circulation in the ES. Recent observations on deep-water structures in the ES, therefore, would represent the re-strengthening of MOC in the ES via re-initiation of the deep ventilation in the ES. In particular, it is occurring even under the continued warming.

These results on vigorous changes in the ES ventilation system provide significant global implications. Especially, the ES ventilation system change in recent decades under the continued warming would be consistent with what are predicted in the Southern Ocean.

The significantly weakened ventilation from BW to CW in the mid-1990s (Figure 3.24) is analogous to the ceased deep-water formation in the Southern Ocean over a course of a few hundred years [Manabe and Stouffer, 1993; Kim et al., 2001], providing the "a clue" to future changes (thin green arrow in Figure 3.24 and Figure 3.25). The weakened ventilation is represented by changes in DO profiles from 1954 to 1979 to 1996 due to more DO supply into CW with open-ocean convection (Figure 3.25) and increase of the CW volume (Figure 3.24), The re-initiation of the BW formation during the latest decades, accompanying by changes in DO profiles from 1996 to 2005 to 2015 due to more DO supply into DW and BW (Figure 3.24 and Figure 3.25) and conditions favorable for the enhanced slope convection (Figure 3.21, 3.22 and 3.23), yields the slowdown in declining BW DO (Figure 3.17). This most recent change in the ventilation system is analogous to the enhanced deep ventilation, which was recently projected for the Southern Ocean with a multi-millennium simulation [Yamamoto et al., 2015], providing "another clue" to future changes (thin blue arrow in Figure 3.24 and Figure 3.25) and the idea of 'East Sea as a miniature ocean'.

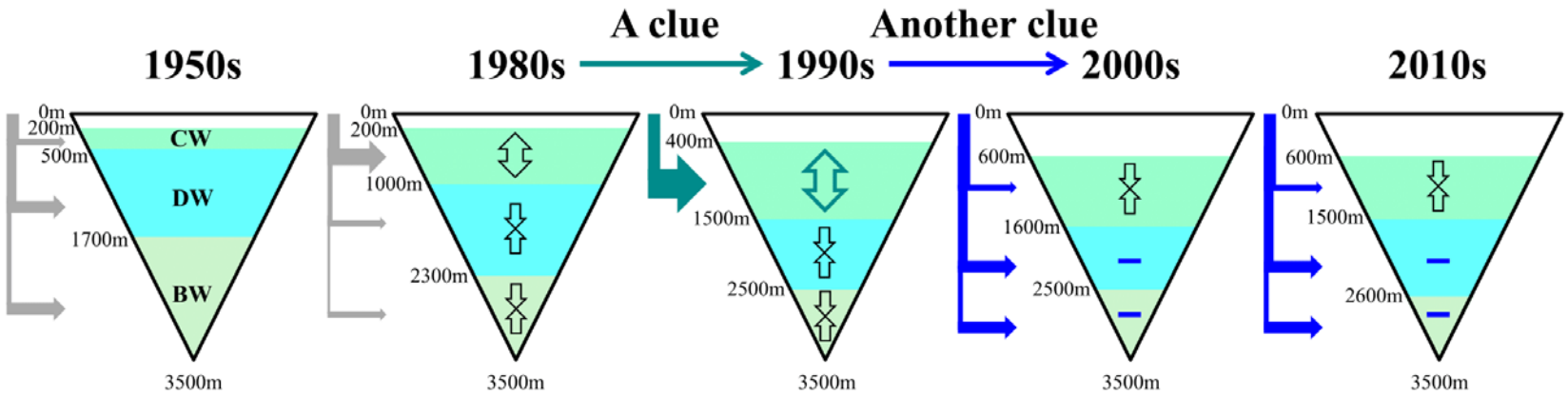

Figure 3.24. Schematics of changes in the East Sea ventilation since the 1950s. Vertical water boundaries are shown for representing periods; (1950s, 1980s, 1990s, 2000s, and 2010s, with significant changes in 1990s and 2000s) following the volumes of deep-water masses (CW; Central Water, DW; Deep Water, and BW; Bottom Water). Convective supplies of water volume (e.g., transport) and DO (e.g., flux) from the surface are marked with thick filled arrows where the formation of CW (DW and BW) via open-ocean convection (slope convection) is highlighted. Significant increasing and decreasing water volumes are shown with vertical arrows. Recent slowdowns of reduction in DW and BW are marked by hyphens in 2000s and 2010s. A thin green arrow denotes “a clue” and thin blue arrow indicates “another clue”.

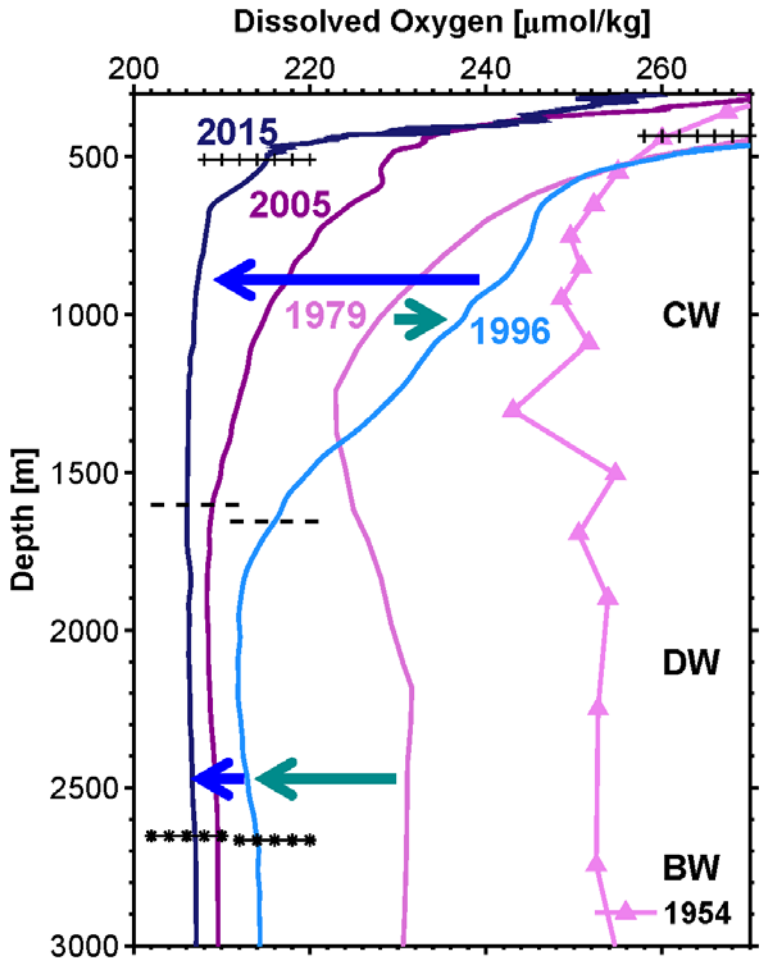

Figure 3.25. The same as Figure 3.18d, but a vertical DO profile in 1954 [Kim et al., 2001] is also represented by violet triangles and line. Plus (Dashed) lines indicate the upper (lower) boundary of CW at 1996 and 2015. Asterisk lines are for the upper boundary of BW at 1996 and 2015. Vertical DO profiles from 1954 to 1979 to 1996 and from 1996 to 2005 to 2015 denote "a clue" (green arrows) and "another clue" (blue arrows) to future changes for global ocean.

5. Conclusions and suggestions for the future study

In this study, temporal variation of non-seasonal heat content anomaly (HCA) down to 500 m in the East Sea (ES) south of the subpolar front (southward of 42 °N) during 1976–2007 and recent changes in structures and volumes of deep-water masses in the ES observed on CREAMS cruise data from 1993 to 2016 are investigated. The main results of these researches are summarized below.

(1) An anomalous cooling trend of HCA during 1976 and 2007 is found in the southwestern ES, while rest of the area south of the subpolar front has a warming trend with the fastest warming trend west of the Tsugaru Strait in the eastern ES, consistent with the result of Na et al. [2012]. This spatial contrast is also concurrent with a spatially different warming rate in the daily sea surface temperature (SST) in the two regions, faster SST warming in the eastern ES and slow SST warming in the western ES.

(2) According to the spatially-smoothed gridded data [Na et al., 2012], the area-averaged HCA exhibits a warming trend that is twice as fast as the global ocean's warming trend in the upper 500 m. A localized weak cooling trend in the southwestern ES was also revealed by Na et al. [2012]. However, the trend estimate based on in situ data in the Ulleung Basin that cover the zone of western boundary current (KODC data) yields four times faster cooling rate than that from the gridded data in the southwestern ES, and there exists virtually no linear trend of HCA south of the subpolar front if the KODC data are used instead of the gridded data in the

southwestern ES. This demonstrates that caution should be exercised in heat content calculation using spatially-smoothed data especially in regions affected by strong and narrow boundary currents.

(3) Temporal variations of HCA both in the southeastern and southwestern ES are characterized by predominant decadal-scale and in-phase variations before 1995. During this period, HCA in the western ES leads that in the southeastern ES. The decadal variation of HCA becomes indistinct after 1995 in both regions. Instead, interannual variations become dominant and the HCAs in the two regions are poorly correlated.

(4) Decomposition of HCA components into the warming and heaving effects of four temperature ranges representing characteristic water masses in the ES reveals that the major contribution to the HCA, including long-term trends in both regions, comes from the deepening or shoaling of 10 ℃ isotherm depths and associated heat content variations ($\overline{T}H'_1$, TWW heaving). This accounts for higher than 60% of the total variance of the HCA in both regions. The thickness variation of the East Sea Intermediate Water layer and the thermocline layer are also important factors in the southeastern and southwestern ES, respectively, with a percent variance larger than 20%.

(5) Significant correlations between the TWW heaving and surface geostrophic currents crossing two sections affected by the EKWC and the ONB demonstrate that the HCA in the ES mainly arise from the upper circulation variability. Spatial correlation maps between the TWW heaving and SST in the western and eastern ES provide further evidence of the important role of the upper circulation in determining the HCA.

(6) Correlation analysis between directly measured volume transports through the eastern (EVT) and western (WVT) channels of the Korea Strait and the TWW heaving in the southeastern and southwestern ES shows a different lead-lag relationship before and after 1995, which is not so well understood. Nevertheless, a consistent explanation is possible about the relationship before 1995 based on correlations significant at the 95% CL. As a previous study noted, when the WVT is large, an early separation of the EKWC occurs, which acts to reduce the TWW heaving because of the shoaling of the layer warmer than 10 ℃. This process results in a decrease in HCA in the southwestern ES. A decrease in the EVT follows the WVT increase after two years, which then ONB poorly develops in the southeastern ES, which causes a shoaling of the layer warmer than 10 ℃ and a decrease in the HCA in the southeastern ES.

(7) The TWW heaving in the southwestern ES is significantly correlated with changes in the winter wind stress curl in the northeastern ES and the East Korea Bay, which are then shown to be closely related with the winter Western Pacific teleconnection pattern (WP) and Siberian High (SH) indices before 1995. The weakening of positive wind stress curl in those regions during the positive WP and negative SH allows farther northward penetration of the EKWC in the southwestern ES due to the weakening of the cyclonic subpolar gyre in the northern ES, resulting in the deepening of the upper layer warmer than 10 ℃. However, as the intensity of the SH weakened after 1995, the TWW heaving is only significantly correlated with the WP but not with the SH. The heaving of the TWW layer in the southeastern ES is poorly correlated with the wind stress curl field and the WP, while it shows

significant negative correlation with the SH before and after 1995. It is yet to be discovered how the SH influences the heat content variation in the southeastern ES.

(8) Series of vertical profiles of potential temperature and dissolved oxygen collected in the central Japan Basin in the ES clearly show that the deepening of deep salinity minimum (CW–DW boundary) and upper limit of the benthic homogeneous layer (DW–BW boundary) have slowed down since mid-2000s.

(9) Slowdown the declining rate of BW dissolved oxygen is also detected after the mid-1990s although BW saturation dissolved oxygen is rapidly decreased in the recent decade due to the strong warming. This variation supports re-initiation of the BW formation in the latest decade.

(10) Using one-dimensional advection-diffusion model I suggest a halt of CW formation and continued formation of DW in the mid-2000s, supporting significant changes of ventilation system in the latest decade. This result is more convinced by the successful reconstruction of the results of one-dimensional advection-diffusion model with only using the volume changes of deep-water masses.

(11) More chances for the slope convection with the enhanced surface buoyancy flux (by cooling, brine rejection, and salt flux of the TWC) into the northern ES to form the BW, and fewer chances for the open-ocean convection with the reduced MLD to form the CW, overall supporting the three-layered deep-water structure in the ES without a loss of the BW at least by 2040.

(12) Through researching about HCA variations and ES ventilation system changes, physical properties of seawater in the upper and deep ocean in the recent decade are experienced different phases compared to those in the past.

(13) As discussed about warming and non-warming effects, I can figure out that the local oceanic and atmospheric forcing is more important than the effect of global climate change in determining the recent changes of physical properties of seawater in the ES.

(14) The importance of the heaving effect in HCA and re-initiation of the BW formation in the ES are analogous with observed or predicted results in the global ocean so the idea of ‘miniature ocean, East Sea’ is still valid.

This study illustrates recent changes of physical properties of seawater in the ES under the continued global warming but there are still many questions for future studies. First of all, I note that spatially-averaged temperature at 200 m in the southwestern ES is well correlated with the first EOF mode of temperature at 50 m in the Yellow Sea with predominantly negative temperature anomalies since 1995 [Park et al., 2011]. This relation strongly suggests a connection of the southeastern ES with the North Pacific [Na et al., 2012] and a connection of the southwestern ES with the Yellow Sea. Thus, future work is required to investigate the linkage of the east-west contrast of heat content variations in the ES with temperature variations in the North Pacific and the Yellow Sea along with oceanic and atmospheric processes making those connections. Thickness and temperature variations of the subsurface layers also need future investigation in association with any change in the ventilation of the ES. Especially, the long-term variation of ESIW is actively studied recently [Nam et al., 2016; Yun et al., 2016] so heaving and warming components of the ESIW layer should be compared with these results.

Moreover, it is demonstrated that the linear fitting lines for deep-water structures in the past are inappropriate to represent the

recent deep structural changes in the ES. Thus, the balance equations used in the Moving Boundary Box Model should be modified by the newly fitting lines for boundaries of deep-water masses [Figure 3.15 and 3.17b] and a fate of the BW needs to be newly predicted. And CTD profiles and Winkler bottle samples should be continuously observed at station C to check maintenance of three-layer deep-water structure and long-term variation of DO profile. The diffusion coefficient (K) and upwelling velocity (w) used in the 1-D advection-diffusion model were not validated from observations in deep-water formation area. They also need to be obtained from an analysis of isotope data (ex) carbon-14) and the microstructure profiler in near future. Recent analysis of the microstructure profiler [Matsuno et al., 2015] measurements in the Yamato Basin suggests that K is 10^{-5}~$10^{-3.5}$ m^2/s. Lastly, ES survey in winter should be conducted to observe the processes for deep-water formations as reported in the winter, 2001 [Kim et al., 2002b; Lobanov et al., 2002; Senjyu et al., 2002; Tsunogai et al., 2003].

Bibliography

Bindoff, N. L. and T. J. Mcdougall (1994), Diagnosing climate change and ocean ventilation using hydrographic data, *J. Phys. Oceanogr.,* 24, 1137-1152, doi: http://dx.doi.org/10.1175/1520-0485(1994)024<1137:DCCAOV>2.0.CO;2

Boyer, T. P., H. E. Garcia, D. R. Johnson, R. A. Locarnini, A. V. Mishonov, M. T. Pitcher, O. K. Baranova, and I. V. Smolyar (2006), World Ocean Database 2005, NOAA Atlas NESDIS, vol. 60, edited by S. Levitus, 192 pp., NOAA, Silver Spring, Md.

Bryden, H. L., H. R. Longworth, and S. A. Cunningham (2005), Slowing of the Atlantic meridional overturning circulation at 25° N, *Nature*, 438, 655-657, doi: 10.1038/nature04385

Cavalieri, D. J., J. Crawford, M. Drinkwater, W. J. Emery, D. T. Eppler, L. D. Farmer, M. Goodberlet, R. Jentz, A. Milman, C. Morris, R. Onstott, A. Schweiger, R. Shuchman, K. Steffen, C. T. Swift, C. Wackerman, and R. L. Weaver (1992), *NASA Sea Ice Validation Program for the DMSP SSM/I: Final Report,* NASA Technical Memorandum 104559, National Aeronautics and Space Administration, Washington, D. C. 126 pages

Cavalieri, D. J., C. L. Parkinson, P. Gloersen, and H. J. Zwally (2015), Sea Ice Concentrations from Nimbus-7 SMMR and DMSP SSM/I-SSMIS Passive Microwave Data, Version 1.1. NASA National Snow and Ice Data Center Distributed Active Archive Center, Boulder, Colorado USA, doi: http://dx.doi.org/10.5067/8GQ8LZQVL0VL.

Chang, K.-I., N. Hogg, M.-S. Suk, S.-K. Byun, Y.-G. Kim, and K. Kim (2002), Mean flow and variability in the southwestern East Sea, *Deep-Sea Res., I.,* 49, 2261-2279, doi:10.1016/S0967-0637(02)00120-6

Chang, K.-I., W. J. Teague, S. J. Lyu, H. T. Perkins, D.-K. Lee, D. R. Watts, Y.-B. Kim, D. A. Watts, Y.-B. Kim, D. A. Mitchell, C. M. Lee, and K. Kim (2004), Circulation and currents in the southwestern

East/Japan Sea: Overview and review, *Prog. Oceanogr.,* 61, 105-156, doi: 10.1016/j.pocean.2004.06.005

Chang, K.-I., C.-I. Zhang, C. Park, D.-J. Kang, S.-J. Ju, S.-H. Lee, and M. Wimbush (2016), Oceanography of the East Sea (Japan Sea), 460 pp, Springer, Switzerland

Chen, C. T. A., A. S. Bychkov, S. L. Wang, G. Y. Pavlova, and W. H. Liu (1999), An anoxic sea of Japan by the year 2200?, *M. Chemistry*, 67, 249-265, doi: 10.1029/2001GL013367

Cho, Y.-K, and K. Kim (1994), Two modes of salinity-minimum layer water in the Ulleung Basin, *La Mer,* 32, 271-278

Cho, Y.-K, and K. Kim (1996), Seasonal variation of the East Korea Warm Current and its relation with the cold water, *La Mer,* 34, 172-182

Cho, Y.-K, and K. Kim (2000), Branching mechanism of the Tsushima current in the Korea strait, *J. Phys. Oceanogr.*, 30, 2788-2797, doi: http://dx.doi.org/10.1175/1520-0485(2000)030<2788:BMOTTC>2.0.CO;2

Choi, K.-S. and I.-J. Moon (2012), Influence of the Western Pacific teleconnection pattern on Western North Pacific tropical cyclone activity, *Dyn. Atmos. and Oceans,* 57, 1-16, doi: 10.1016/j.pocean.2004.06.003

Emery, W. J. and R. E. Thomson (1997), Effective degrees of freedom, in Data Analysis Methods in Physical Oceanography, 2nd edition, pp. 257-263, Elsevier Science, Amsterdam

Fukudome, K.-I., J.-H. Yoon, A. Ostrovskii, T. Takikawa, and I.-S. Han (2010), Seasonal volume transport variation in the tsushima warm current through the tsushima straits from 10 years of ADCP observations, *J. Oceanogr.,* 66, 539-551, doi: 10.1007/s10872-010-0045-5

Gamo, T., Y. Nozaki, H. Sakai, T. Nakai, and H. Tsubota (1986), Spatial and temporal variations of water characteristics in the Japan Sea bottom layer, *J. Mar. Res.*, 44, 781-793, doi: http://dx.doi.org/10.1357/002224086788401620

Gamo, T., N. Momoshima, and S. Tolmachyov (2001), Recent upward shift of the deep convection system in the Japan Sea, as inferred from the geochemical tracers tritium, oxygen, and nutrients, *Geophys. Res. Lett.*, 28, 4143–4146, doi: 10.1029/2001GL013367

Gamo, T. (2011), Dissolved oxygen in the bottom water of the Sea of Japan as a sensitive alarm for global climate change, *Tr. Anal. Che.*, 30, 1308–1319, doi: 10.1016/j.trac.2011.06.005

Gamo, T., N. Nakayama, N. Takahata, Y. Sano, J. Zhang, E. Yamazaki, S. Taniyasu, and N. Yamashita (2014), The Sea of Japan and its unique chemistry revealed by time-series observations over the last 30 years, *Monogr. Environ. Earth Planets*, 2, 1–22, doi:10.5047/meep.2014.00201.0001

Gille, S. T. (2008), Decadal-scale temperature trends in the Southern Hemisphere Ocean, *J. Clim.,* 21, 4749–4765, doi: 10.1175/2008JCLI2131.1

Global Modelling and Assimilation Office (GMAO) (2015), MERRA-2 tavgM_2d_ocn_Nx: 2d, monthly mean, time-averaged, single-level, assimilation, ocean surface diagnostics V5. 12. 4. Goddard Earth Sciences Data and Information Services Center (GES DISC), Greenbelt, MD, USA, doi:http://dx.doi.org/10.5067/ 4IASLIDL8EEC

Gordon, A. L., C. F. Guilivi, C. M. Lee, H. H. Furey, A. Bower, and L. Talley (2002), Japan/East Sea intrathermocline eddies, *J. Phys. Oceanogr.,* 32, 1960–1974, doi:10.1175/1520–0485(2002)032<1960:JESIE>2.0.CO;2.

Han, I. S., and Y.–Q. Kang (2003), Supply of heat by Tsushima warm current in the East Sea (Japan Sea), *J. Oceanogr.,* 59, 317–323, doi:10.1023/A:1025563810201

Hase, H., J.–H. Yoon, and W. Koterayama (1999), The current structure of the Tsushima Warm Current along the Japanese coast, *J. Oceanogr.,* 55, 217–235, doi: 10.1023/A:1007894030095

Hill, K. L., S. R. Rintoul, R. Coleman, and K. R. Ridgway (2008), Wind forced low frequency variability of the East Australia Current,

Geophys. Res. Lett., 35, L08602, doi:10.1029/2007GL032912

Hirose, N., C.-H. Kim, and J.-H. Yoon (1996), Heat budget in the Japan Sea, *J. Oceanogr.,* 52, 553-574, doi: 10.1007/BF02238321

Hofmann, M., and S. Rahmstorf (2009), On the stability of the Atlantic meridional overturning circulation, *PNAS*, 106 (49), 20584-20589, doi: 10.1073/pnas.0909146106

Hogan J. P., and H. E. Hurlburt (2000), Impact of upper ocean-topographical coupling and isopycnal outcropping in Japan/East Sea models with 1/8° to 1/64° resolution, *J. Phys. Oceanogr.*, 30, 2535-2561, doi: 10.1175/1520-0485(2000)030<2535:IOUOTC>2.0. CO;2

Hong, C. H., K. D. Cho, and S. K. Yang (1984), On the abnormal cooling phenomenon in the coastal areas of East Sea of Korea in summer 1981, *J. Oceanol. Soc. Korea*, 19, 1-17

IPCC (2014), Climate Change 2014: Synthesis Report. Contribution of Working Groups I, II and III to the Fifth Assessment Report of the Intergovernmental Panel on Climate Change [Core Writing Team, R.K. Pachauri and L.A. Meyer (eds.)]. IPCC, Geneva, Switzerland, 151 pp

Ishi, Y., and K. Hanawa (2005), Large-scale variabilities of wintertime wind stress curl field in the North Pacific and their relation to atmospheric teleconnection patterns, *Geophys. Res. Lett.,* 32, L10607, doi:10.1029/2004GL022330

Isobe, A., and Y. Isoda (1997), Circulation in the Japan basin, the northern part of the Japan Sea, *J. Oceanogr.,* 53, 373-381

Ito, M., A. Morimoto, T. Watanabe, O. Katoh, and T. Takikawa (2014), Tsushima Warm Current paths in the southwestern part of the Japan Sea, *Prog. Oceanogr.,* 121, 83-93, doi: 10.1016/j.pocean.2013.10.007

Jenkins, W.J. (2008), The biogeochemical consequences of changing ventilation in the Japan/East Sea, *Mar. Chem.*, 108, 137-147, doi: 10.1016/j.marchem.2007.11.003

Jo, H.-S., S.-W. Yeh, and C.-H. Kim (2013), A possible mechanism for the North Pacific regime shift in winter of 1998/1999, *Geophys. Res. Lett.,* 40, 4380-4385, doi:101.1002/grl.50798

Kang, D.-J., K.-E. Lee, and K.-R. Kim (2003a), Recent developments in chemical oceanography of the East (Japan) Sea with an emphasis on CREAMS findings: A review, *Geosci. J.,* 7, 179-197, doi: 10.1007/BF02910222

Kang, D.-J., S. Park,Y.-G. Kim, K. Kim, and K.-R. Kim (2003b), A moving-boundary box model (MBBM) for oceans in change: An application to the East/Japan Sea, *Geophys. Res. Lett.*, 30, 32-1-32-4, doi: 10.1029/2002GL016486

Kang, D.-J., K. Kim, and K.-R. Kim (2004a), The past, present and future of the East/Japan Sea in change: a simple moving-boundary box model approach, *Prog. Oceanogr.*, 61, 175-191, doi: 10.1016/j.pocean.2004.06.006

Kang, D.-J., J.-Y. Kim, T. Lee, and K.-R. Kim (2004b), Will the East/Japan Sea become an anoxic sea in the next century?, *M. Chemistry*, 91, 77-84, doi: 10.1016/j.marchem.2004.03.020

Katoh, O. (1994), Structure of the Tsushima Current in the southwestern Japan Sea, *J. Oceanogr.,* 49, 17-30, doi: 10.1007/BF02239520

Kawamura H., and P. Wu (1998), Formation mechanism of Japan Sea Proper Water in the flux center off Vladivostok, *J. Geophys. Res.,* 103, 611-621, doi: 10.1029/98JC01948

Kim, C.H., and J.-H. Yoon (1996), Modeling of the wind-driven circulation in the Japan Sea using a reduced gravity model, *J. Oceanogr.,* 52, 359-373, doi: 10.1007/BF02235930

Kim, K., K.-I. Chang, D.-J. Kang, Y. H. Kim, and J.-H. Lee (2008), Review of recent findings on the water masses and circulation in the East Sea (Sea of Japan*), J. Oceanogr.,* 64, 721-735, doi: 10.1007/s10872-008-0061-x

Kim, K. and J. Y. Chung (1984), On the salinity-minimun and dissolved oxygen-maximum layer in the East Sea (Sea of Japan), in Ocean Hydrodynamics of the Japan and East China Seas, 55-65pp., edited by T. Ichiye, Elsevier Science Publishers, Amsterdam

Kim, K., K.-R. Kim, Y.-G. Kim, Y.-K. Cho, J.-Y. Chung, B.-H. Choi, S.-

K. Byun, G.-H. Hong, T. Masaki, J.-H. Yoon, Y. Volkov, and M. Danchenkov (1996), New findings from CREAMS observations: Water masses and Eddies in the East Sea, *J. Kor. Soc. Oceanogr.*, 31, 155-163

Kim, K., K.-R. Kim, Y.-G. Kim, Y.-K. Cho, D.-J. Kang, M. Takematsu, and Y. Volkov (2004), Water masses and decadal variability in the East Sea (Sea of Japan), *Prog. Oceanogr.,* 61, 157-174, doi: 10.1016/j.pocean.2004.06.003

Kim, K., K.-R. Kim, D.-H. Min, Y. Volkov, J.-H. Yoon, and M. Takematsu (2001), Warming and Structural changes in the East (Japan) Sea: A clue to future changes in global oceans?, *Geophys. Res. Lett.*, 28, 3293-3296, doi: 10.1029/2001GL013078

Kim, K. and R. Legeckis (1986), Branching of the Tsushima Current in 1981-1983, *Prog. Oceanog,* 17, 265-276, doi: 10.1016/0079-6611(86)90049-2

Kim, K.-R., and K. Kim (1996), What is happening in the East Sea (Japan Sea)?: Recent chemical observations during CREAMS 93-96, *J. Kor. Soc. Oceanogr.*, 31, 164-172

Kim, K.-R., K. Kim, D.-J. Kang, Y. N. Volkov, J.-H. Yoon, and M. Takematsu (2002a), The changes in the East/Japan Sea found by CREAMS, *Oceanogr. Jap.*,11, 419-429, doi: http://doi.org/10.5928/kaiyou.11.419

Kim, K.-R., G. Kim, K. Kim, V. Lobanov, V. Ponomarev, and A. Salyuk (2002b), A sudden bottom-water formation during the severe winter 2000-2001: The case of the East/Japan Sea, *Geophys. Res. Lett.*, 29, 75-1-75-4, doi: 10.1029/2001GL014498

Kim, Y.-G., K. Kim, Y.-K. Cho, and H. Ossi (2000), CTD data processing for CREAMS expeditions: Thermal-lag correction of Sea-Bird CTD, *J. Kor. Soc. Oceanogr.*, 35, 192-199

Kumamoto, Y.-I., M. Yoneda, Y. Shibata, H. Kume, A. Tanaka, T. Uehiro, M. Morita, and K. Shitashima (1998), Direct observation of the rapid turnover of the Japan Sea bottom water by means of AMS radiocarbon

measurement, *Geophys. Res. Lett.*, 25, 651-654, doi: 10.1029/98GL00359

Large W. G. and S. Pond (1981), Open ocean momentum flux measurements in moderate to strong winds, *J. Phys. Oceanogr.,* 11, 324-336, doi: http://dx.doi.org/10.1175/1520-0485(1981)011<0324:OOMFMI> 2.0.CO;2

Lee, S.-H., D.-S. Byun, B.-J. Choi, and E. Lee (2009), Estimation of the surface currents using mean dynamic topography and satellite altimeter data in the East Sea, *J. Korean Soc. Oceanogr.,* 14(4), 195-204

Lee, D.-K., Y. H. Seung, Y.-B. Kim, Y. H. Kim, H.-R. Shin, C.-W. Shin, and K.-I. Chang (2016), Chapter 4: Circulation, in Oceanography of the East Sea (Japan Sea), 460 pp., edited by K.-I. Chang, C. I. Zhang, C. Park, D.-J. Kang. S.-J. Ju, M. Wimbush, Springer, Switzerland.

Lee, S.-K. (1999) Self-excited variability of the East Korea Warm Current: A quasi-geostrophic model study, *J. Korean Soc. Oceanogr.,* 34(1), 1-21

Levitus, S., J. Antonov, and T. P. Boyer (2005), Warming of the world ocean, 1955-2003, *Geophys. Res. Lett.,* 32, L02604, doi: 10.1029/2004GL021592

Levitus, S., J. Antonov, T. P. Boyer, and C. Stephens (2000), Warming of the world ocean, *Science,* 287, 2225-2228, doi: 10.1126/science.287.5461.2225

Levitus, S., J. Antonov, T. P. Boyer, O.K. Baranova, H.E. Garcia, R.A. Locarnini, A.V. Mishonov, J.R. Reagan, D.Seidov, E.S. Yarosh, and M.M. Zweng (2012), World ocean heat content and thermosteric sea level change (0-2000 m), 1955-2010, *Geophys. Res. Lett.*, 39, L23610, doi: 10.1029/2012GL051106, 2012

Lim, S., C. J. Jang, I. S. Oh, and J. Park (2012), Climatology of the mixed layer depth in the East/Japan Sea, *J. Mar. Sys.*, 96-97, 1-14, doi: 10.1016/j.jmarsys.2012.01.003

Lobanov, V., A. Salyuk, V. Ponomarev, L. Talley, K. Kim, K.-R. Kim, P. Tishchenko, A. Nedaskovskiy, G. Kim, and S. Sagalaev (2002), Renewal of bottom water in the Japan/East Sea, Proc. 17th Int. Symp. Okhotsk Sea & Sea Ice, Mombetsu, Japan, 2002

Lozier, M. S., S. Leadbetter, R. G. Williams, V. Roussenov, M. S. C. Reed, and N. J. Moore (2008), The spatial pattern and mechanisms of heat-content change in the North Atlantic, *Science,* 319, 800-803, doi: 10.1126/science.1146436

Manabe, S., and R. J. Stouffer (1993), Century-scale effects of increased atmospheric CO_2 on the ocean-atmosphere system, *Nature*, 364, 215-217, doi: 10.1038/364215a0

Marshall, J., and F. Schott, Open-ocean convection: Observations, theory, and models, *Rev. Geophys.*, 37, 1- 64, 1999, doi: 10.1029/98RG02739

Matsuno, T., T. Endoh, T. Hibiya, T. Senjyu, and M. Watanabe (2015), Formation of the well-mixed homogeneous layer in the bottom water of the Japan Sea, *J. Oceano.,* 71, 441-447, doi: 10.1007/s10872-015-0303-7

Mensah, V., M. L. Menn, and Y. Morel (2009), Thermal Mass correction for the evaluation of salinity, *J. Atmos. Oceanic Technol.*, 26, 665-672, doi: http://dx.doi.org/10.1175/2008JTECHO612.1

Minobe, S., A. Sako, and M. Nakamura (2004), Interannual to interdecadal variability in the Japan Sea Based on a new gridded upper water temperature dataset, *J. Phys. Oceanogr.,* 34, 2382-2397, doi: 10.1175/JPO2627.1

Mitchell D. A., D. R. Watts, M. Wimbush, W. J. Teague, K. L. Tracey, J. W. Book, K.-I. Chang, M.-S. Suk, and J.-H. Yoon (2005) Upper circulation patterns in the Ulleung Basin, *Deep-Sea Res. II,* 52, 1617-1638. doi:10.1016/j.dsr2.2003.09.005

Min, D.-H., and M. J. Warner (2005), Basin-wide circulation and ventilation study in the East Sea (Sea of Japan) using chlorofluorocarbon tracers, *Deep Sea Res., Part Ⅱ*, 52, 1580-1616, doi: 10.1016/j.dsr2.2003.11.003

Minami, H., Y. Kano, and K. Ogawa (1999), Long-term variations of potential temperature and dissolved oxygen of the Japan Sea Proper Water, *J. Oceanogr.*, 55, 197−205, doi: 10.1023/A:1007889929187

Morison, J., R. Andersen, N. Larson, E. D' Asaro, and T. Boyd (1994), The correction for Thermal-lag effects in Sea-Bird CTD data, *J. Atmos. Oceanic Technol.*, 11, 1151−1164, doi: http://dx.doi.org/10.1175/1520−0426(1994)011 <1151:TCFTLE>2.0.CO;2

Na, H., K.−Y. Kim, K.−I. Chang, J. J. Park, K. Kim, and S. Minobe (2012), Decadal variability of the upper ocean heat content in the East/Japan Sea and its possible relationship to northwestern Pacific variability, *J. Geophys. Res.,* 117, C02017, doi: 10.1029/2011JC007369

Nam. S., Y. H. Kim, K.−A. Park, K. Kim (2005), Spatio-temporal variability in sea surface wind stress near and off the east coast of Korea, *Acta Oceano. sin.,* 24, 107−114

Nam. S., S.−T. Yoon, J.−H. Park, Y. Kim, and K.−I. Chang (2016), Distinct characteristics of the intermediate water observed off the east coast of Korea during two contrasting years, *J. Geophys. Res.,* 121, doi: 10.1002/2015JC011593

Onishi, M., and K. Ohtani (1997), Volume transport of the Tsushima Warm Current, west of Tsugaru Strait bifurcation area, *J. Oceanogr., 53*, 27−34, doi: 10.1007/BF02700746

Ozgokmen, T. M., E. P. Chassignet, and A. M. Paiva (1997) Impact of wind forcing, bottom topography, and inertia of midlatitude jet separation in a quasigeostrophic model, *J. Phys. Oceanogr.,* 27, 2460−2476, doi: http://dx.doi.org/10.1175/1520−0485(1997)027<2460:IOWFBT>2.0.CO;2

Pak, G., Y.−H. Park, F. Vivier, Y.−O. Kwon, and K.−I. Chang (2014), Regime-Dependent Nonstationary Relationship between the East Asian Winter Monsoon and North Pacific Oscillation, *J. Clim.,* 27, 8185−8204, doi: 10.1175/JCLI−D−13−00500.1

Palmer, M. D. and K. Haines (2009), Estimating oceanic heat content change using isotherms, *J. Clim.,* 22, 4953-4969, doi: 10.1175/2009JCLI2823.1

Palmer, M. D., K. Haines, S. F. B. Tett, and T. J. Ansell (2007), Isolating the signal of ocean global warming, *Geophys. Res. Lett.,* 34 , L23610, doi: 10.1029/2007GL031712

Park, K.-A., K.-I. Chang, H. Na, and U-J. Jung (2016), Chapter 2: Forcings, in Oceanography of the East Sea (Japan Sea), 460 pp., edited by K.-I. Chang, C.I. Zhang, C. Park, D.-J. Kang. S.-J. Ju, M. Wimbush, Springer, Switzerland.

Park, K.-A., J. Y. Chung, and K. Kim (2004), Sea surface temperature fronts in the East (Japan) Sea and temporal variations, *Geophys. Res. Lett.,* 31, L07304, doi:10.1029/2004GL019424

Park, K.-A., J.-E. Park, B.-J. Choi, D.-S. Byun, and E.-I. Lee (2013), An oceanic current map of the East Sea for science textbooks based on scientific knowledge acquired from oceanic measurements, *The Sea, J. Kor. Soc. Oceanogr.,* 18, 234-265, doi: 10.7850/jkso.2013.18.4.234

Park, S., P. C. Chu, and J.-H. Lee (2011) Interannual-to-interdecadal variability of the Yellow Sea Cold Water Mass in 1967-2008: Characteristics and seasonal forcings, *J. Mar. Syst.,* 87, 177-193, doi:10.1016/j.jmarsys.2011.03.012

Park, Y.-G. (2007) The effects of Tsushima Warm Current on the interdecadal variability of the East/Japan Sea thermohaline circulation, *Geophys. Res. Lett.,* 34, L06609, doi:10.1029/2006GL029210

Postlethwaite, C. F., E. J. Rohling, W. J. Jenkins, and C. F. Walker (2005), A tracer study of ventilation in the Japan/East Sea, *Deep Sea Res., Part Ⅱ*, 52, 1684-1704, doi: 10.1016/j.dsr2.2004.07.032

Rahmstorf, S., J. E. Box, G. Feulner, M. E. Mann, A. Robinson, S. Rutherford, and E. J. Schaffernicht (2015), Exceptional twentieth-century slowdown in Atlantic Ocean overturning circulation, *Nature Climate Change*, 5, 475-480, doi:10.1038/nclimate2554

Reynolds, R. W., T. M. Smith, C. Liu, D. B. Chelton, K. S. Casey, and M. G. Schlax (2007), Daily high-resolution-blended analyses for sea surface temperature, *J. Clim., 20*, 5473-5496, doi: 10.1175/2007JCLI1824.1

Roemmich D., J. Gilson, R. Davis, P. Sutton, S. Wijffels, and S. Riser (2007), Decadal spinup of the South Pacific subtropical gyre, *J. Phys. Oceanogr.,* 37, 162-173, doi: 10.1175/JPO3004.1

Sea-Bird Electronics (2014), SBE 9plus CTD user's manual, Seasave V7 version 7.22.5, Washington, 1-73

Send, U., M. Lankhorst, and T. Kanzow (2011), Observation of decadal changes in the Atlantic meridional overturning circulation using 10 years of continuous transport data, *Geophys. Res. Lett.*, 38, L24606, doi: 10.1029/2011GL049801

Seung, Y.-H., and J.-H.,Yoon (1995), Some features of winter convection in the Japan Sea, *J. Oceanogr.*, 51, 61-73, doi: 10.1007/BF02235936

Senjyu, T., T. Aramaki, S. Otosaka, O. Togawa, M. Danchenkov, E. Karasev, and Y. Volkov (2002), Renewal of the bottom water after the winter 2000-2001 may spin-up the thermohaline circulation in the Japan Sea, *Geophys. Res. Lett.*, 29 (7), 1149, doi: 10.1029/2001GL014093

Smith, P. C. (1973), The dynamics of bottom boundary currents in the ocean, Ph.D thesis, Dep. of Meteorol., Massa. Inst. Tech., Cambridge, USA

Smith, P. C. (1975), A streamtube model for bottom boundary currents in the ocean, *Deep Sea Res.Oceanogr. Abstr.,* 22, 853-873, doi:10.1016/0011-7471(75)90088-1

Song, W., J. Lan, Q. Liu, D. Sui, L. Zeng, and D. Wang (2014), Decadal variability of heat content in the South China Sea inferred from observation data and an ocean data assimilation product, *Ocean Sci.,* 10, 135-139, doi: 10.5194/os-10-135-2014

Speer, K., and E. Tziperman (1992), Rates of water mass formation in the North Atlantic Ocean, , *J. Phys. Oceanogr.*, 22, 93-104, doi: http://dx.doi.org/10.1175/1520-

0485(1992)022<0093:ROWMFI>2.0.CO;2

Stocker T. F., and A. Schmittner (1997), Influence of CO_2 emission rates on the stability of the thermohaline circulation, *Nature*, 388, 862-865

Stocker T. F., and D. G. Wright (1991), Rapid transitions of the ocean's deep circulation induced by changes in surface water fluxes, *Nature*, 351, 729-732

Stocker, T. F., R. Knutti, and G.-K. Plattner (2001), The Future of the Thermohaline Circulation - a Perspective, in The Oceans and Rapid Climate Change: Past, Present, and Future (eds D. Seidov, B. J. Haupt and M. Maslin), American Geophysical Union, Washington, D. C.. doi: 10.1029/GM126p0277

Takikawa, T., and J.-H. Yoon (2005), Volume transport through the Tsushima straits estimated from sea level difference, *J. Oceanogr.,* 61, 699-708, doi: 10.1007/s10872-005-0077-4

Talley, L. D., V. Lobanov, V. Ponomarev, A. Salyuk, P. Tishchenko, and I. Zhabin (2003), Deep convection and brine rejection in the Japan Sea, *Geophys. Res. Lett.*, 30, 1159, doi: 10.1029/2002GL016451

Talley, L. D., D.-H. Min, V. B. Lobanov, V. A. Luchin, V. I. Ponomarev, A. N. Salyuk, A. Y Shcherbina, P. Y. Tishchenko, and I. Zhabin (2006), Japan/East Sea water masses and their relation to the sea's circulation, Oceanography, 19, 32-49, doi: http://dx.doi.org/10.5670/oceanog.2006.42

Talley, L. D., P. Tishchenko, V. Luchin, A. Nedashkovskiy, S. Sagalaev, D.-J. Kang, M. Warner, D.-H. Min (2004), Atlas of Japan (East) Sea hydrographic properties in summer, 1999, *Prog. Oceanogr.*, 61, 277-348, doi: 10.1016/j.pocean.2004.06.011

Tanaka, K. (2014), Formation of bottom water and its variability in the northwestern part of the Sea of Japan, *J. Geophy. Res.*, 119, 2081-2094, doi: 10.1002/2013JC009456

Trusenkova, O., A. Nikitin, and V. Lobanov (2009), Circulation features in the Japan/East Sea related to statistically obtained wind patterns in the warm season, *J. Mar. Sys.,* 78, 214-225, doi: 10.1016/j.jmarsys.

2009.02.019

Tsunogai, S., K. Kawada, S. Watanabe, and T. Aramaki (2003), CFC indicating renewal of the Japan Sea Deep Water in winter 2000–2001, *J. Oceanogr.*, 59, 685–693, doi: 10.1023/B:JOCE.0000009597.33460.d7

Uda, M.(1934) The results of simultaneous oceanographical investigations in the Japan Sea and its adjacent waters in May and June, 1932, *Japan Imp. Fish. Exp. Sta.,* 5, 57–190 (in Japanese)

Visbeck, M., E. P. Chassignet, R. Curry, T. Delworth, B. Dickson, and G. Krahmann (2003), Chapter 6: The Ocean's Response to North Atlantic Oscillation Variability, 113–145 pp., edited by J.W. Hurrell, Y. Kushnir, G. Ottersen, M. Visbeck, Amer. Geophy. Union, Washington, D.C.

Watanabe, Y.W., M. Wakita, N. Maeda, T. Ono, and T. Gamo (2003), Synchronous bidecadal periodic changes of oxygen, phosphate, and temperature between the Japan Sea deep water and the North Pacific intermediate water, *Geophys. Res. Lett.,* 30(24), 2273, doi: 10.1029/2003GL018338

Wu, B. Y., and J. Wang (2002), Winter Arctic Oscillation, Siberian High and East Asian winter monsoon, *Geophys. Res. Lett.,* 29(9), 1897, doi:10.1029/2002GL015373

Yamamoto, A., A. Abe–Ouchi, M. Shigemitsu, A. Oka, K. Takahashi, R. Ohgaito, and Y. Yamanaka (2015), Global deep ocean oxygenation by enhanced ventilation in the southern ocean under long-term global warming, *Global Biogeochem. Cycles*, 29, 1801–1815, doi:10.1002/2015GB005181

Yeh, S.–W., Y.–G. Park, H. Min, C.–H. Kim, and J.–H. Lee (2010), Analysis of characteristics in the sea surface temperature variability in the East/Japan Sea. *Prog. Oceanogr.,* 85, 213–223, doi:10.1016/j.pocean.2010.03.001

Yoon, J.–H., K. Abe, T. Ogata, and Y. Wakamatsu (2005), The effects of wind-stress curl on the Japan/East Sea circulation, *Deep–Sea Res. II,*

52, 1827-1844, doi:10.1016/j.dsr2.2004.03.004

Yoon, J.-H., and Y.-J. Kim (2009), Review on the seasonal variation of the surface circulation in the Japan/East Sea, *J. Mar. Syst.,* 78, 226-236, doi:10.1016/j.jmarsys.2009.03.003

Yun, J.-Y., K.-I. Chang, K.-Y. Kim, Y.-K. Cho, K.-A. Park, and L. Magaard (2016), ENSO teleconnection to the isopycnal depth fluctuations of the East/Japan Sea Intermediate Water in the Ulleung Basin during 1968-2002, *J. Phys. Oceanogr.,* 46, 2675 - 2694, doi: http://dx.doi.org/10.1175/JPO-D-15-0225.1

Abstract (in Korean)

전세계 대양은 1950년대 이후로 엄청난 온난화를 경험하고 있다. 지구 열 균형 변화에 중요한 역할을 하는 해양의 열용량은 전 대양에 걸쳐 상당히 증가하였다. 해수 순환과 대기 강제력에 의한 자오면 순환의 안정도나 민감도는 미래 해양 변화의 불확실성을 결정하는 중요한 요소에 해당하는데 이 자오면 순환 역시 온난화로 인해 지속적으로 약화 되고 있다는 주장이 꾸준히 제기되어 왔다.

동해는 북서태평양에 위치한 작은 연근해이지만 대양과 역학적 유사성을 가져 작은 대양으로 불리고 있다. 그러므로 동해를 구성하는 해수의 물리적 특성 변화에 관한 고찰을 통해, 온난화와 기후 변화에 따른 동해의 반응을 이해 할 수 있을 뿐 아니라 대양의 현재 혹은 미래 환경 변화에 대한 시사점을 유추할 수 있다. 따라서 본 연구에서는, 지구 온난화가 지속되는 상황 속에서 동해의 상층 열용량과 심층 수괴 변화를 분석하여 해수의 물리적 특성 장기 변화를 고찰하였다.

최근 30년 동안 동해 상층 500 m 의 비계절적 열용량의 변화는 동해 동부와 서부 사이에 분명한 차이를 보였다. 이 열용량 변화의 분명한 공간적 차이를 1976년부터 2007년까지의 격자화된 자료와 1976년부터 2011년까지 서안경계 해류 해역을 포함하는 동해 남서부 해역에서 관측한 자료를 분석하여 조사하였다. 1995년 이전까지는 동해 동부와 서부의 열용량은 같은 위상으로 약 10년 주기의 변화를 보이나 1995년 이후에는 두 열용량의 상관 관계가 낮아지고 수 년 주기의 변화를 보였다. 동해 온난 해류(대마난류)의 주요 분지에 의한 히빙 효과, 특히 서부는 동한난류 동부는 대마난류의 동쪽 분지에 의한 열영량 변화가 열용량 변화의 주된 원인으로 나타났다. 또한 동해 서부의 히빙 효과는 동해 북부의 해상풍 회전장과 연관이 있는 것으로 밝혀졌다. 겨울철 서태평양 원격상관 패턴, 시베리가 고기압과 연관하여 일본 분지에서 양의 부호를 가지는 해상풍 회전장이 약해져 아극

소용돌이가 약해지면 동한난류가 더 북쪽에서 이안하게 되고 이는 동해 서부의 열용량을 증가시키게 된다. 동해 동부의 히빙 효과는 시베리가 고기압 세기와 연관이 되어 있는 것으로 여겨지나 보다 정확한 기작을 연구하기 위해서는 컴퓨터 모델링과 같은 추가적인 연구가 필요하다. 이 열용량 연구는 좁고 강한 경계류가 우세한 해역에서 열용량 변화를 이해하기 위해 공간적으로 매우 조밀한 고분해능의 자료가 중요함도 증명하였다.

또한 본 연구에서는 동해 상층 열용량 변화와 함께 최근 동해에서 나타나는 심층 수괴(동해중앙수, 동해심층수, 동해바닥수) 구조 및 부피 변화를 통해 동해 심층 순환의 활발한 변동을 제시하였다. 표층 해수의 온난화와 관련된 동해 심층해수 생성의 1990년대 변화(바닥수 형성이 중앙수 형성으로 변화)를 심해 염분최소층(중앙수와 심층수의 경계)과 심해저균질층 상부 경계 수심(심층수와 바닥수의 경계)이 깊어지는 변화로부터 파악한 바 있는데, 본 연구에서는 심해 염분최소층과 심해저균질층의 상부 경계 수심이 깊어지는 속도가 2000년대 이후 현저히 느려지는 것을 발견하였고, 이는 바닥수의 형성이 다시 강화되는 것과 연관됨을 제시하였다. 1차원 이류 확산 모델을 통해 2000년대 중반 동해중앙수 형성 약화와 동해심층수로의 용존 산소 공급 강화를 확인하였는데, 바닥수 형성의 강화 증거로 꼽을 수 있다. 이 심층 순환 변화는 동해 북부에서 발생하는 두 종류의 대류 즉, 외양성 대류와 사면 대류의 최근 변화와도 무관하지 않은데, 동해 북부 해역의 혼합층 두께, 표면 부력 유속, 그리고 해빙 변화는 1990년대에 비해 최근 외양성 대류를 통한 중앙수 형성이 약화된 반면, 경사 대류를 통한 바닥수 형성은 강화되는 가능성을 시사한다. 본 연구의 심층 수괴 분석에 의한 새 예측에 따르면 동해 심층의 3층 구조는 최소 2040년까지 유지되며, 이는 대양의 자오면 순환 재강화 가능성도 시사한다.

결론적으로 동해 열용량과 동해 심층 순환은 최근 수십 년간에 급격한 변화 모습을 보인다. 그리고 지난 수십 년간 관측된 동해 상층 및 심층 해수의 물리적 특성 장기 변화는 지구 온난화에 의한 해수 수온

증가의 영향보다는 주로 동해 내부 및 외부에서 발생하는 해양과 대기 이류 및 대류 과정들에 의한 효과로 설명된다. 요컨대, 동해의 상층 열용량과 심층 순환 시스템 변화는 '작은 대양으로서의 동해' 특성을 잘 뒷받침한다.

주요어 : 지구 온난화, 해수 열용량, 심층 수괴, 동해, 상층 순환, 심층 순환 시스템
학번 : 2011-20374

Appendix

Table A1. Abbreviations used in the dissertation

Abbreviation	Name
AABW	Antarctic Bottom Water
ACC	Antarctic Circumpolar Current
AMOC	Atlantic Meridional Overturning Circulation
BW	Bottom Water
CL	Confidence Limit
CREAMS	Circulation Research of the East Asian Marginal Seas
CTD	Conductivity-Temperature-Depth
CW	Central Water
DJF	December, January, and February
DO	Dissolved Oxygen
DOM	Dissolved Oxygen Minimum
DSM	Deep Salinity Minimum
DW	Deep Water
EAST	The region of the fastest warming rate in the southeastern ES
EAST-I	East Asian Seas Time-series-I
EJS	The whole area covered by the NA12 data
EKB	East Korea Bay
EKWC	East Korea Warm Current
ES	East Sea
ESIW	East Sea Intermediate Water
EVT	Volume Transports through the Eastern channel of the Korea Strait
HCA	Heat Content Anomaly
JB	Japan Basin
JSPW	Japan Sea Proper Water
KODC	Korea Oceanographic Data Center

MBBM	Moving Boundary Box Model
MLD	Mixed Layer Depth
MOC	Meridional Overturning Circulation
NA12	monthly mean temperature data used by Na et al. [2012]
NAO	North Atlantic Oscillation
NB	Nearshore Branch
NKCC	North Korea Cold Current
NIFS	National Institute of Fisheries Science
OB	Offshore Branch
OHC	Ocean Heat Content
ONB	Offshore and Nearshore Branch
OUR	Oxygen Utilization Rates
r	correlation coefficients
RMS	Root Mean Square
SBE	Sea-Bird Electronics
SH	Siberian High
SSH	Sea Surface Height
SSS	Sea Surface Salinity
SST	Sea Surface Temperature
TWC	Tsushima Warm Current
TWW	Tsushima Warm Water
UB	The region covered by the KODC data
UBHL	Upper limit of a Benthic Homogeneous Layer
VT	Volume Transports through the entire Korea Strait
WEST	The region of the slow cooling rate in the southwestern ES
WOD	World Ocean Database
WP	Western Pacific teleconnection pattern
WSC	Wind Stress Curl
WSCA	Wind Stress Curl Anomaly
WVT	Volume Transports through the Western channel of the

	Korea Strait
YB	Yamato Basin

Table A2. Percent variance of each decomposed part of total eight components of HCA to HCA, cross correlation coefficients between each decomposed part and HCA, and the linear trend of each decomposed part (Trend) in the EJS defined in the text with 90% confidence level of the trend. $\bar{\mathbf{T}}\mathbf{H}_\mathbf{i}'$ denotes the i-th heaving component and $\bar{\mathbf{H}}\mathbf{T}_\mathbf{i}'$ the i-th warming component.

EJS	Water Mass	Temperature range (℃)	Part	Variance (%)	r	Trend ($\times 10^6$ J/m^2/ month)
	TWW	$10 < T$	$\bar{T}H'_1$	57.4	0.95	0.59 ± 0.91
			$\bar{H}T'_1$	3.1	0.73	0.27 ± 0.26
	Thermocline layer	$5 < T < 10$	$\bar{T}H'_2$	5.8	−0.29	-0.40 ± 0.30
			$\bar{H}T'_2$	0.5	0.94	0.09 ± 0.09
	ESIW	$1 < T < 5$	$\bar{T}H'_3$	24.9	0.26	0.86 ± 0.79
			$\bar{H}T'_3$	2.7	−0.28	-0.30 ± 0.28
	JSPW	$1 > T$	$\bar{T}H'_4$	3.0	−0.57	-0.32 ± 0.29
			$\bar{H}T'_4$	2.6	0.45	0.34 ± 0.26

Table A3. The long-term trends of deep structures reported in Kang et al. [2003b] and calculated in this study. The position of station C, W, and E is 41.3°N, 134°E, 41°N, 132.3°E, and 42°N, 136°E, respectively. The JB denotes trends of the averaged deep structures in the JB (north of 39°N, 131–139°E). A positive value means a deepening tendency of depth. The significant trend at 95% confidence level is highlighted in bold. Other listed trends are significant at 90% confidence level.

Trend (1952–1996) [m/year]	0.13–0.15 ℃					UBHL (DO)
Kang et al. [2003b]		18.53				26.87
Trend (1994–2016) [m/year]	**0.6 ℃**	**0.13–0.15 ℃**	**DSM**	**DOM**	**UBHL (θ)**	**UBHL (DO)**
JB	8.14	20.89	7.55	−34.04		
Sta. C	9.62	20.52		−15.66		
Sta. W		15.47		−35.88	−5.47	
Sta. E	4.90	16.24				

Table A4. Upper and Lower limit of CW and DW for applying the 1-D advection-diffusion model at each cruise's Station C.

Cruise date	Upper limit of CW [m]	Lower limit of CW [m]	Upper limit of DW [m]	Lower limit of DW [m]
Aug., 1993				
Jul., 1994	700	1,450	1,600	2,450
Mar., 1995	700	1,350	1,550	2,550
Jul., 1995	780	1,350	1,550	2,350
Feb., 1996	650	1,550	1,700	2,450
Aug., 1996	800	1,400	1,800	2,550
Mar., 1997	850	1,600	1,800	2,450
Feb., 1999	550	1,300	1,550	2,350
Jun., 1999	950	1,500	1,750	2,500
Mar., 2000	500	1,350	1,700	2,500
Apr., 2001				
Apr., 2002				
Oct., 2005	600	1,250	1,700	2,450
May, 2007	750	1,650	1,800	2,500
Jul., 2009	850	1,600	1,850	2,540
Oct., 2012	750	1,700	2,000	2,450
Apr., 2014	800	1,400	1,650	2,550
Apr., 2015	750	1,450	1,700	2,600

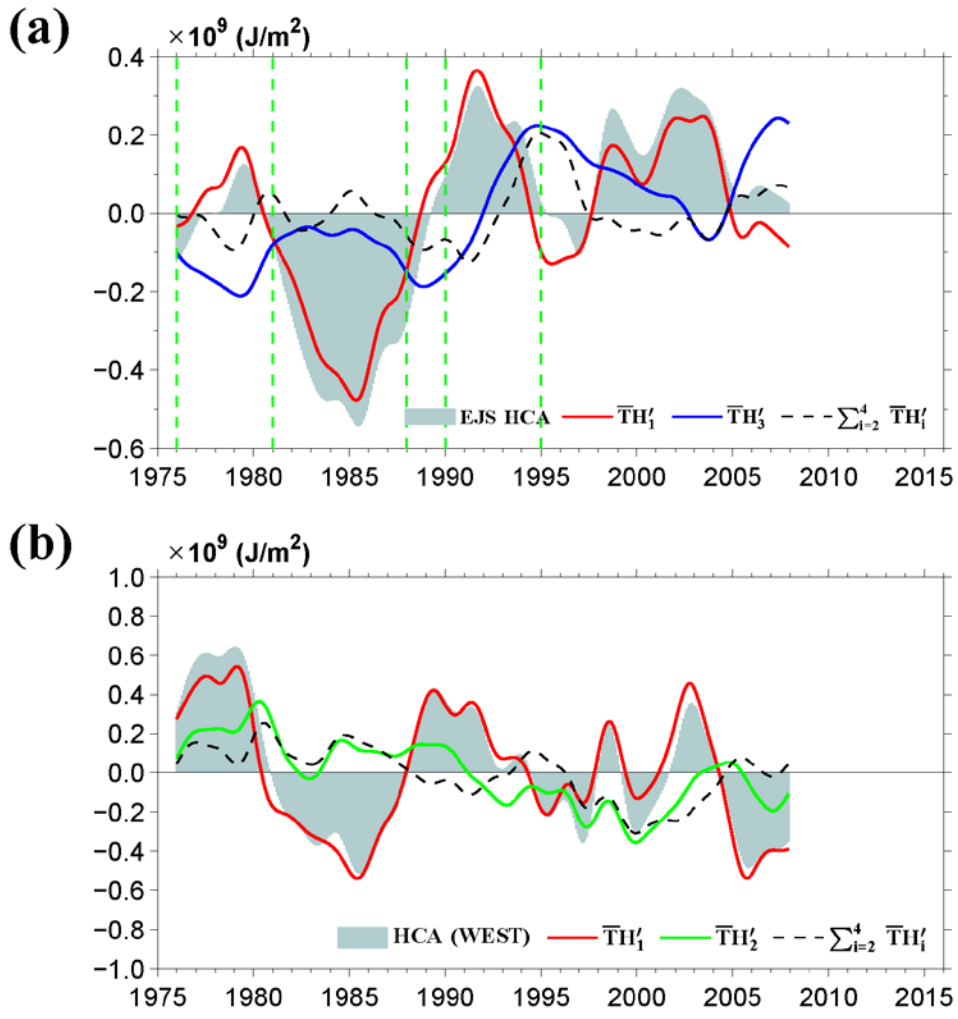

Figure A1. (a) Time series of HCA (shading), $\overline{\mathbf{TH}}'_{\mathbf{1}}$ (red), $\overline{\mathbf{TH}}'_{\mathbf{3}}$ (blue), and $\sum_{\mathbf{i=2}}^{\mathbf{4}} \overline{\mathbf{TH}}'_{\mathbf{i}}$ (black dashed) in the EJS. Vertical green dashed lines indicate years for dividing the time series of HCA in the EAST and WEST into in- and out-phase periods. (b) Time series of HCA (shading), $\overline{\mathbf{TH}}'_{\mathbf{1}}$ (red), $\overline{\mathbf{TH}}'_{\mathbf{2}}$ (green), and $\sum_{\mathbf{i=2}}^{\mathbf{4}} \overline{\mathbf{TH}}'_{\mathbf{i}}$ (black dashed) in the WEST.

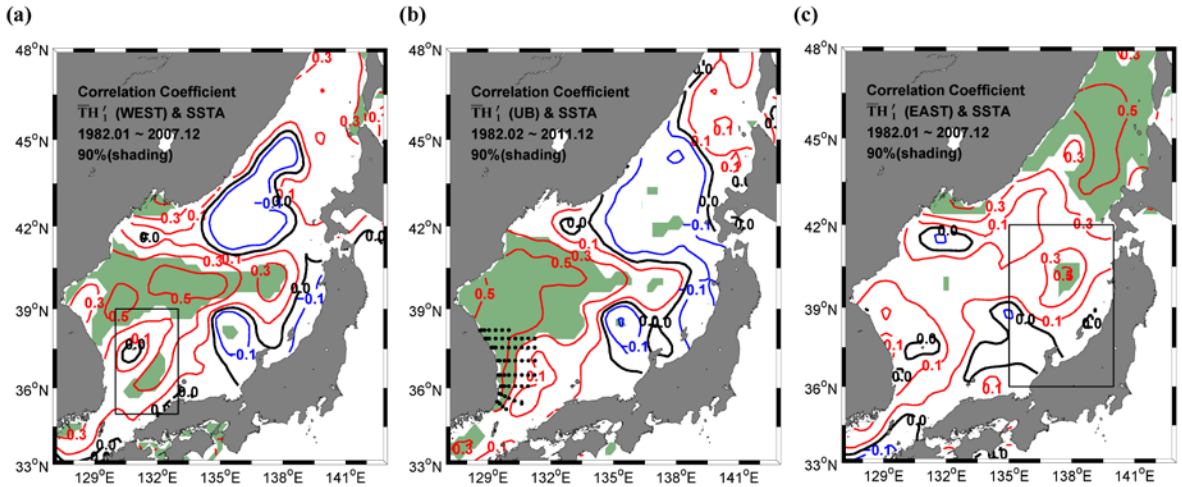

Figure A2. Spatial correlation map (a) between de-trended non-seasonal SST variation and $\overline{TH}'_1$ variation in the WEST (1982–2007), (b) between de-trended non-seasonal SST variation and $\overline{TH}'_1$ in the UB (1982–2011), and (c) between de-trended non-seasonal SST variation and $\overline{TH}'_1$ in the EAST (1982–2007). The non-seasonal SST is calculated by subtracting the monthly mean climatology. The shaded areas have a significant correlation coefficient at the 90% confidence level. Areas having a significant correlation coefficient at the 95% confidence level is also shown in (c) with yellow green color.

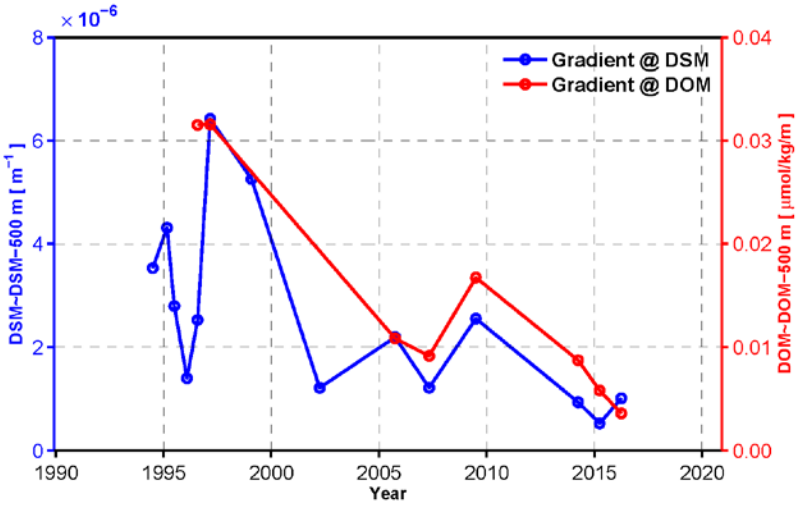

Figure A3. A blue dot line indicates salinity (S) gradients between DSM and DSM minus 500 m ($|S_{z=DSM} - S_{z=DSM-500}|/500$ [m^{-1}]) during 1993–2016. A red dot line shows dissolved oxygen (DO) gradients between DOM and DOM minus 500 m ($|DO_{z=DSM} - DO_{z=DSM-500}|/500$ [µmol/kg/m]) during 1993–2016.

Publications and Presentations

※ Published papers

1. Yoon, S.-T., K.-I. Chang, S. Nam, T. Rho, D.-J. Kang, T. Lee, K.-A. Park, V. Lobanov, D. Kaplunenko, P. Tishchenko, and K.-R. Kim, Re-initiation of bottom water formation in the East Sea (Japan Sea): Another clue to future changes in global ocean? (Peer reviewing in *Scientific Reports* from June 22, 2017)

2. Yoon, S.-T., K.-I. Chang, H. Na, and S. Minobe (2016), An east-west contrast of upper ocean heat content variation south of the subpolar front in the East/Japan Sea, *J. Geophys. Res. Oceans*, 121, 6418-6443.

3. Nam, S., S.-T. Yoon, J.-H. Park, Y. Kim, and K.-I Chang (2016), Disitinct characteristics of the intermediate water observed off the east coast of Korea during two contrasting years, *J. Geophys. Res. Oceans*, 121, 5050-5068.

4. Son, Y.-T., K.-I. Chang, S.-T. Yoon, T. Rho, J. H. Kwak, C. K. Kang, and K.-R. Kim (2014), A newly observed physical cause of the onset of the subsurface spring phytoplankton bloom in the southwestern East Sea/Sea of Japan, *Biogeosciences*, 11, 1319-1329.

5. Rho, T., Y.-B. Kim, J. I. Park, Y.-W. Lee, D. H. Im, D.-J. Kang, T. Lee, S.-T. Yoon, T.-H. Kim, J.-H. Kwak, H. J. Park, M. K.

Jeong, K.-I. Chang, C.-K. Kang, H.-L. Suh, M. Park, H. Lee, and K.-R. Kim (2010), Plankton Community Response to Physico-Chemical Forcing in the Ulleung Basin, East Sea during Summer 2008, *Ocean Polar Res.*, 32 (3), 269-289.

※ Conference Presentations

1. Oral, Yoon, S.-T., S. Nam, and K.-I. Chang, "The east-west contrast of upper ocean heat content variation south of the subpolar front in the East/Japan Sea", 2017 Korean Society of Oceanography Spring Meeting, Apr. 19-20, 2017, Busan, Korea

2. Oral, Nam, S., S.-T. Yoon, M. Han, and Y.-K. Cho, "Intradecadal changes of meridional overturning circulations observed and modeled in the East Sea (Japan Sea)", 2017 10th WESTPAC international Science Conference, Apr. 17-20, 2017, Qingdao, China

3. Poster, Yoon, S.-T., M. Han, and S. Nam, "Interannual variations of Kuroshio transport and upper ocean heat content in the southeast East Sea (Japan Sea)", 2017 Pacific Asian Marginal Seas Meeting, Apr. 11-13, 2017, Jejudo, Korea

4. Oral, Kim, K.-R., D.-J. Kang, S. Park, D. Hahm, T. Rho, T. Lee, S.-T. Yoon, S. Nam, and K.-I. Chang, "Dissolved oxygen: A powerful tracer for changes in physical dynamics, A case for the East Sea (Japan Sea)", 2017 The third Xiamen Symposium on Marine Environmental Sciences (XMAS-Ⅲ), Jan. 9-11, 2017, Xiamen, China

5. Poster, Yoon, S.-T., K.-I. Chang, K.-R. Kim, and V. B. Lobanov, "Long-term variation of ventilation system in the East Sea (Japan Sea) revealed by heat content change and water mass analysis", 2016 Ocean Science Meeting, Feb. 21-26, 2016, New Orleans, USA

6. Poster, Nam, S, S.-T. Yoon, J.-H. Park, Y. H. Kim, and K.-I. Chang, "Distinct characteristics of Intermediate Water observed off the east coast of Korea during two contrasting years", 2016 Ocean Science Meeting, Feb. 21-26, 2016, New Orleans, USA

7. Oral, Yoon, S.-T. and K.-I. Chang, "Regional variation of the upper ocean heat content and its causative mechanisms in a marginal sea of the Western Pacific Ocean", 2015 Open Science Symposium, Oct. 26-28, 2015, Busan, Korea

8. Poster, Nam, S., S.-T. Yoon, J.-H. Park, Y. H. Kim, and K.-I. Chang, "Distinct characteristics of East Sea Intermediate Water in response to varying western boundary current", 2015 Open Science Symposium, Oct. 26-28, 2015, Busan, Korea

9. Poster, Yoon, S.-T. and K.-I. Chang, "The role of regional variation of the upper ocean heat content and its causative mechanisms in the East/Japan Sea", 2015 Pacific Asian Marginal Seas Meeting, Apr. 21-23, 2015, Okinawa, Japan

10. Poster, Yoon, S.-T. and K.-I. Chang, "Heat content variations due to strengthening and weakening of cold and warm currents in the southwestern East/Japan Sea", 2014 Ocean Science Meeting,

Feb. 23-28, 2014, Hawaii, USA

11. Oral, Yoon, S.-T. and K.-I. Chang, "Heat content variations in the southwestern East/Japan Sea", 2013 PICES annual meeting, Oct. 11-20, 2013, Nanaimo, Canada

12. Poster, Yoon, S.-T. and K.-I. Chang, "Decadal variability and cooling trend of intermediate layer heat content in the southwestern East/Japan Sea", International Workshop "Regional Climate Models-Ⅱ", Sep. 10-12, 2013, Seoul, Korea

13. Oral, Yoon, S.-T. and K.-I. Chang, "Heat content variations in the southwestern East/Japan Sea", 2013 Korean Society of Oceanography Spring Meeting, May. 23-24, 2013, Jeju, Korea